Vortex Waves and Evolution in Sharp Vorticity Gradient Vortices

Wesley D. Terwey and Michael T. Montgomery

Research Supported by the National Science Foundation
Grants #ATM-0101781 and ATM-0132006

And the Office of Naval Research
Grant #ONR-N00014-93-1-0456

Colorado State University

DEPARTMENT OF ATMOSPHERIC SCIENCE

PAPER NO. 734

VORTEX WAVES AND EVOLUTION IN SHARP VORTICITY GRADIENT VORTICES

Wesley D. Terwey and Michael T. Montgomery

Research supported through the National Science Foundation under Grants ATM-0101781 and ATM-0132006 and the Office of Naval Research under Grant ONR-N00014-93-1-0456.

Principal Investigator: Michael T. Montgomery

Department of Atmospheric Science

Colorado State University

Fort Collins, Colorado 80523

April 2003

Atmospheric Science Paper No. 734

ABSTRACT

Intense geophysical vortices are observed to be strongly axisymmetric and frequently possess steep gradients of vorticity around their cores. Such vortices are often surrounded by asymmetric disturbances that act to deform the mean vortex. The evolution of such intense vortices in response to these small-amplitude forcings is an important and interesting study and the topic of this work.

Previous studies investigated the interactions between vorticity perturbations on two, concentric, sharp vorticity gradients and detailed a classic exponential instability. We perform here a general and complete linearized analysis of a similar, but unrestricted, three region vortex initial value problem (IVP) in a two-dimensional, non-divergent model, including initial disturbances both on and in the vicinity of the pair of steep vortex gradients. Using this more general model, we complete the exponential instability analysis, noting the existence of a wavenumber-2 instability in cases previously not studied.

After constructing the solution to the linear IVP, we show that the addition of sheared disturbances does not change the long-time stability properties of the main vortex. The mean flow changes due to the momentum fluxes of these sheared disturbances, however, are altered considerably by the perturbation flow associated with the deformed vortex core. Mean flow changes are particularly large in magnitude for sheared disturbances located near critical radii in the mean flow. Perturbations near these radii resonantly force and deform the main vortex, leading to the breakdown of linear theory and the significance of nonlinear mixing processes around these radii. The nonlinear effects on the mean vortex in these resonant cases can lead to resonant damping of the deformed vortex which is not possible in the strictly linear IVP. Finally, we demonstrate the importance of nonlinearities

in evolution of sharp gradient vortices and point out the usefulness and limitations of linear theory.

ACKNOWLEDGEMENTS

This research was supported in part by the National Science Foundation under Grants ATM-0101781 and ATM-0132006, the Office of Naval Research under Grant ONR-N00014-93-1-0456, and Colorado State University.

We would like to thank Professor V.A. Vladimirov for making us aware of his previous experimental work and stability analysis that motivated Chapter 3 of this work. Thanks also go out to Thomas Cram, Eric Hendricks, Jim Kossin, John Persing, Paul Reasor, Andrea Saunders, Wayne Schubert, and Laurie Trenary for their constructive suggestions. We would also like to thank Jillian L'Ecuyer, Kathy Mulica, and Sam Grandlienard for their help in the administrative and computer areas. Thanks finally go to Wen Chau Lee of NCAR, who kindly provided the DOW tornado data used in Chapter 1.

CONTENTS

Chapter 1

INTRODUCTION

Some of the strongest winds in the world are associated with intense atmospheric vortices. Tornadoes frequently contain winds in excess of 50 m/s and will occasionally top out above 100 m/s, often demolishing any structures in their paths. Hurricanes are not known to frequently exhibit such extreme wind maxima, but have a larger areal coverage of 50 m/s or greater winds, as well as flooding rains and sea surges. Unlike its tropospheric cousins, the polar stratospheric vortex does not directly impact humans, but does frequently have 50 m/s and greater circumferential winds, and is vitally important to the chemistry of the stratosphere.

Because of the importance of these vortical phenomena, researchers have studied each of these vortices in depth, in many varied ways. Despite their temporal and spatial differences, though, these vortices share some similarities that allow us to draw some conclusions about all three at once. One such similarity can be inferred from Figures 1.1, 1.2, and 1.3. These figures focus on the vorticity, a measure of the microscopic rotation of a fluid particle (technically, twice the local rotation rate of the particle), in the main vortex.

On May 3, 1999, a series of supercells formed in Oklahoma and Kansas. Some very strong tornadoes formed in association with these supercells, including one that passed over the town of Mulhall, Oklahoma. A single Doppler on Wheels (DOW) radar caught the evolution of this tornado during a portion of its peak intensity (Wurman, 2002). This unique dataset is currently unmatched in its resolution of the inner core structure and evolution of a large and violent tornado, along with its attendant multiple vortex structures. Using the GBVTD technique (Lee et al., 1999), the azimuthal mean structure of the tornado around its

center has been estimated with a high degree of confidence (Lee, personal communication). Figure 1.1 shows the estimated azimuthal mean tangential velocity and vertical vorticity at 0316 UTC on May 4, 1999 in the Mulhall tornado derived from the DOW data and the GBVTD technique as a representative snapshot. While the large values of vorticity (on the order of 0.1 s^{-1}) in the core region of the tornado ($r \leq 500$ m) dominate the plot, the intense radial gradient of the vorticity just outside this core is almost as impressive.

Moving up the size scale, we next examine some data from a strong hurricane. Figure 1.2 is a plot of tangential wind and vorticity derived from flight-level data of a flight into Hurricane Gilbert (1988) (Kossin and Schubert, 2001; NOAA Hurricane Research Division archive). The dashed line represents the tangential velocity, while the solid line denotes the relative vorticity derived from this velocity. The dominant feature in this figure is the narrow annular region of elevated vorticity near the vortex center surrounded by a relatively low vorticity environment that fluctuates around an approximately constant value. Although this profile is derived from a single radial flight leg, given the strong axisymmetry the storm portrayed at this time, it provides a rough estimate of the azimuthal mean structure of the vortex. Similar to the tornado, the radial gradients of vorticity in this profile are quite strong.

Moving up in size even further, we look finally at the polar stratospheric vortex. Although the vortex in the Southern Hemisphere is typically more intense because of a lack of major mountain ranges and other synoptic scale forcing in the Southern Hemisphere's mid-latitudes, the intensity of the Northern Hemisphere's vortex can be significant at times. Using the Berlin Stratospheric Research Group's data series for the Northern Hemisphere (Labitzke et al., 2002), we computed the zonal mean zonal winds and absolute geostrophic vorticity during some particularly strong vortex events. Figure 1.3 shows one particular realization of the polar vortex, corresponding to an event on December 19, 1991. As with the tornado and hurricane profiles, we notice that the stratospheric vortex has a particularly sharp gradient in vorticity, here between 60 and 70 degrees latitude.

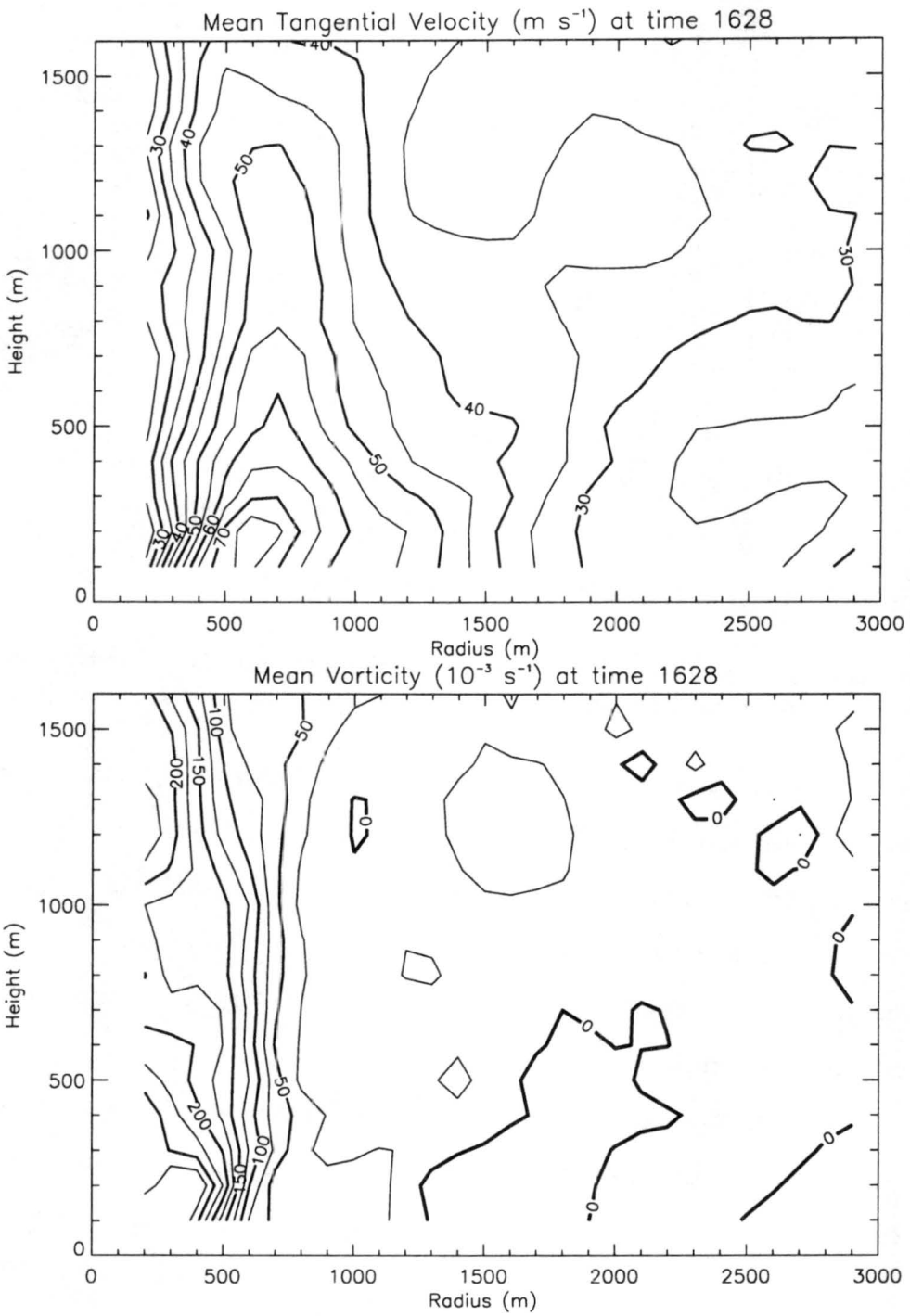

Figure 1.1: Azimuthal mean tangential velocity (top) and vertical vorticity (bottom) at 0316 UTC on May 4, 1999 for the Mulhall tornado. The data comes from a single Doppler on Wheels (Wurman, 2002), analyzed using the GBVTD technique. (Lee et al., 1999) [Data provided by W. Lee, personal communication.]

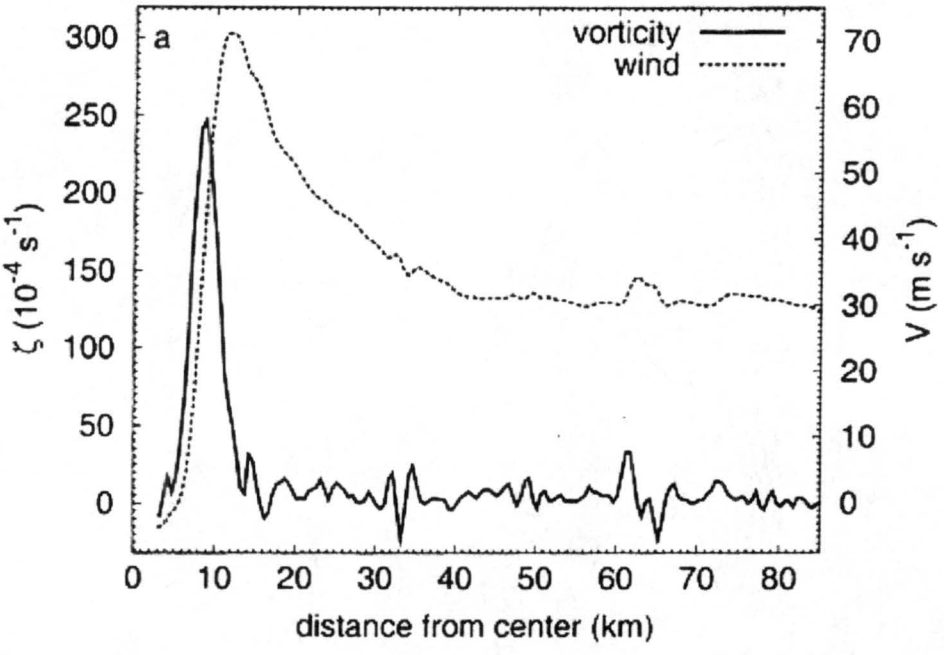

Figure 1.2: From Kossin and Schubert (2001). Radial flight-level data from Hurricane Gilbert (1988) showing a sample radial profile of vorticity (solid) and tangential velocity (dashed).

From these figures, we notice that well-developed geophysical vortices can have sharp gradients of mean vorticity in the radial direction (radial in tornadoes and hurricanes, equatorward in the polar vortex) as well as relatively constant values of vorticity outside these strong gradient regions. This should not be too surprising since, as suggested in Dritschel (1998), "vortices tend to develop and maintain sharp gradients" when diffusion processes are nonexistent.

These steep gradients of vorticity are dynamically important since these types of vortices tend to have a strong resilience to deformations. Because of this, steep gradient vortices tend to have a strong "elasticity" in response to being perturbed (e.g. McIntyre, 1993). Therefore, it is interesting to examine what is needed to significantly deform such vortices as well as examining the effects that this elasticity may have on features close to the vortex. Also, because of these steep gradients, the perturbations to the azimuthal mean that develop as a vortex is deformed can be quantitatively substantial. These perturbations of the mean vortex in the vicinity of the steep gradients are often called "discrete vortex

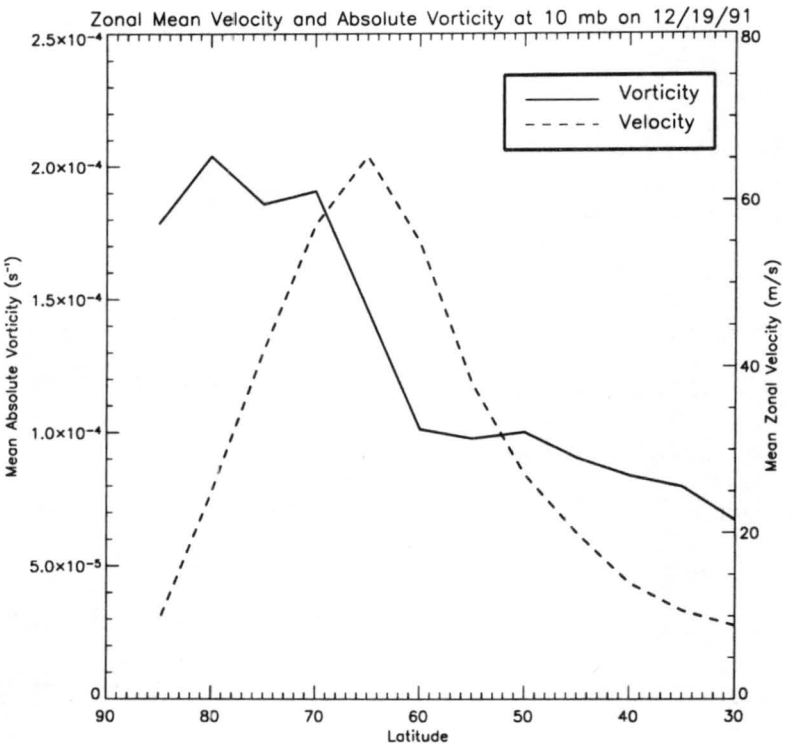

Figure 1.3: Zonal mean zonal winds and absolute geostrophic vorticity at 10 mb on December 19, 1991 in the Northern Hemisphere. The data is derived from the Berlin Stratospheric Data Series (Labitzke et al., 2002).

Rossby waves," alluding to the similarities they have to synoptic-scale Rossby waves. For example, discrete vortex Rossby waves propagate because their perturbation radial winds cross the sharp gradient of mean vorticity. Because total vorticity must be conserved, the perturbation moves. This is analogous to planetary Rossby waves which propagate due to perturbation's meridional winds advecting the planetary vorticity gradient in a regime of absolute vorticity conservation. A more detailed interpretation of this idea is handled in Chapter 3 of this work.

Vortices with these steep gradients have been studied in some detail in the past. A simple, and frequently used, approach in the investigation of such vortices involves the limiting case where the mean vorticity profile is assumed to be piecewise constant, i.e. discontinuously jumping at particular radii as an approximation to the steep gradients (e.g. Michalke and Timme, 1967; Flierl, 1988 [hereafter F88]; Dritschel, 1989; Schubert et al., 1999 [hereafter S99]). This is an extreme limiting case, but permits us to find closed-form

solutions in our analytical study while removing only a small number of vortex phenomena, such as discrete vortex Rossby wave damping (Schecter et al., 2000) and air parcel exchanges between the core and environment. For the analytical portion of this work, we will not focus on the most basic limiting case: the Rankine vortex, which has a uniform vorticity out to a certain radius, and no vorticity outside this vortex core, but will instead use its extended relative, the "three-region" vortex, to be explained in more detail in Chapter 2. In a later section, though, we will utilize a "smoothed-out" version of the Rankine vortex for use in a numerical model simulation to gain a more complete, yet simplified, understanding of the nonlinear evolution of gently-forced sharp gradient vortices.

Until now, we have been focusing on the azimuthal mean structure of the vortex, but observations has shown that geophysical vortices are generally not strictly axisymmetric. There are often small amplitude, asymmetric deviations, or perturbations, superimposed on this mean flow in the vicinity of the vortex. As an illustrative example of this, consider Figure 1.4. This figure is a simple schematic showing a discrete vortex Rossby wave excited by exterior vorticity disturbances in the vicinity of an intense Rankine vortex (cf. Smith and Montgomery, 1995, section 5). For small amplitudes, the initial vorticity perturbations (dashed red and blue contours) are mainly advected by the mean winds outside the initial main vortex (dashed black contour). The portions of these perturbations closer to the vortex core get advected around the core faster than those further from the core. After some time, this differential rotation stretches and elongates the patches of perturbation vorticity (solid red and blue contours), thus motivating the terminology "sheared disturbances." The main vortex gets deformed (solid black contour) by the induced radial winds of these sheared perturbations. The deviations of the Rankine vortex from axisymmetry are the discrete vortex Rossby waves. Their rotation rate around the mean vortex is determined not only by simple Rossby wave theory (Lamb, 1932), but also by the winds associated with the sheared disturbances.

Examples of vorticity perturbations in geophysical vortices include topographically forced Rossby waves in the polar stratospheric vortex, local downdrafts from the convection

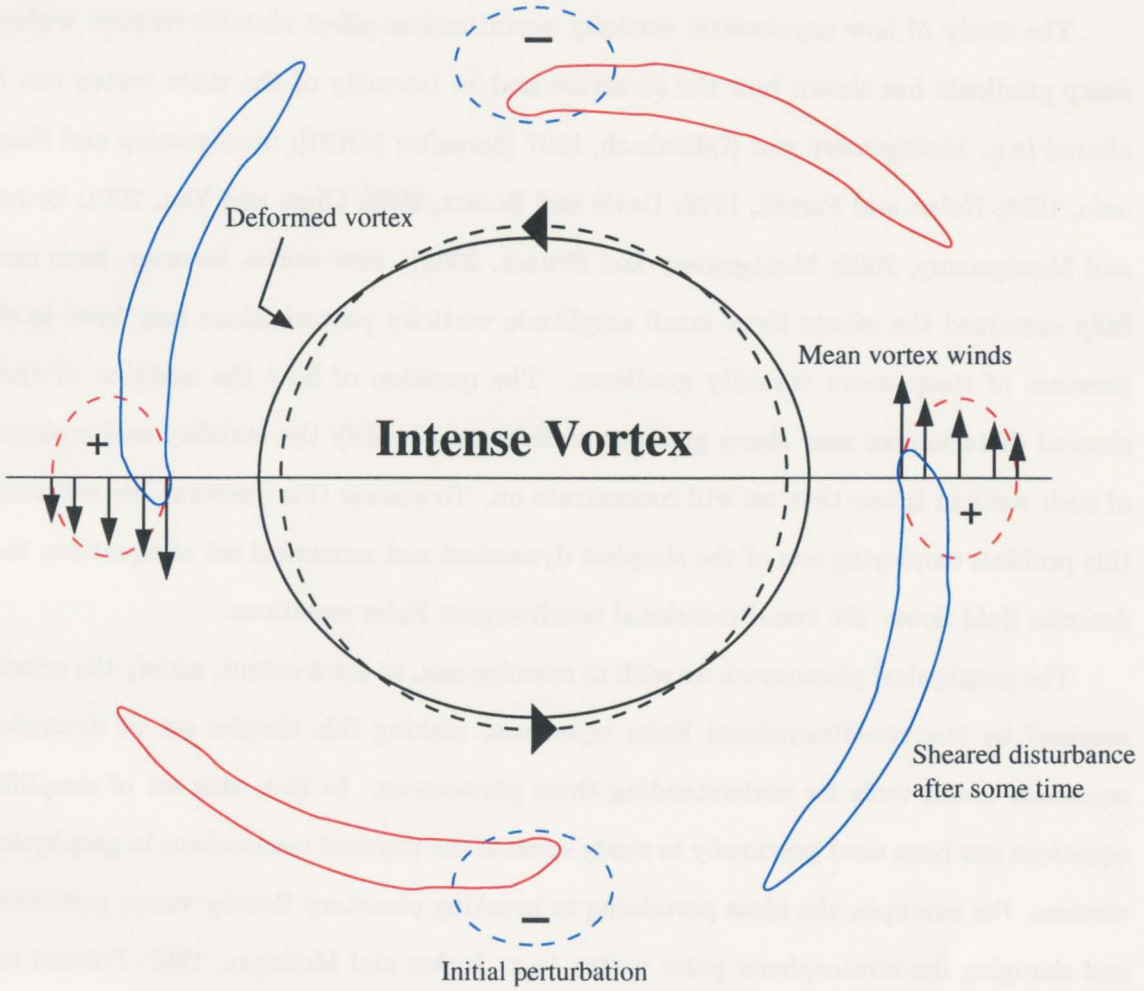

Figure 1.4: A simple schematic showing a discrete vortex Rossby wave excited by exterior vorticity disturbances in the vicinity of an intense Rankine vortex. For small amplitudes, the initial vorticity perturbations (dashed red and blue contours) are mainly advected by the mean winds outside the initial main vortex (dashed black contour). The portions of these perturbations closer to the vortex core get advected around the core faster than those further from the core. After some time, this differential rotation stretches and elongates the patches of perturbation vorticity (solid red and blue contours), thus motivating the terminology "sheared disturbances." The main vortex gets deformed (solid black contour) by the induced radial winds of these sheared perturbations. The deviations of the Rankine vortex from axisymmetry are the discrete vortex Rossby waves. Their rotation rate around the mean vortex is determined not only by simple Rossby wave theory, but also by the winds associated with the sheared disturbances.

nearby in a tornado, spiral bands in a hurricane, or a vorticity anomalies resulting from bursts of convection in a hurricane.

The study of how asymmetric vorticity perturbations affect circular vortices without sharp gradients has shown how the structure and/or intensity of the main vortex can be altered (e.g. Montgomery and Kallenbach, 1997 [hereafter MK97]; Montgomery and Enagonio, 1998; Nolan and Farrell, 1999; Davis and Bosart, 2000; Chen and Yau, 2001; Brunet and Montgomery, 2002; Montgomery and Brunet, 2002). Few works, however, have carefully examined the effects these small amplitude vorticity perturbations may have in the presence of steep mean vorticity gradients. The question of how the addition of these sheared disturbances near sharp gradient vortices may modify the stability and evolution of such vortices is one that we will concentrate on. To answer this question, we will study this problem employing one of the simplest dynamical and numerical set of equations that describe fluid flows: the two-dimensional nondivergent Euler equations.

The geophysical phenomena we wish to examine can, to some extent, satisfy the criteria assumed by the two-dimensional Euler equations, making this simpler set of dynamical equations useful tools for understanding these phenomena. In fact, this set of simplified equations has been used previously to study some of the physical mechanisms in geophysical vortices. For example, the ideas pertaining to breaking planetary Rossby waves perturbing and changing the stratospheric polar vortex (e.g. Juckes and McIntyre, 1987; Polvani and Plumb, 1992), the many influences that vortex Rossby waves might have on hurricane vortices (e.g. MK97, S99), and a theory for multiple vortex phenomena in tornadoes and hurricanes (e.g. Staley and Gall, 1979; Montgomery et al., 2002) have all been examined in this simplified dynamical framework. We continue and extend some of these studies in this work, discovering physical interactions that may prove useful in explaining phenomena in more complex and realistic frameworks.

Having now set up our approach to this problem, the questions we seek to answer here are, as follows:

- In what ways do these small perturbations affect the vortex and each other?

- Are such changes significant?
- To what extent do the simple ideas pursued here persist, especially as we consider more complex models and dynamical frameworks?

We shed insight on all these questions in this work by examining two different steep gradient vortices analytically in the inviscid two-dimensional non-divergent framework.

A summary of this analysis follows. In Chapter 2, we will set up the analytical framework of the three-region model, posing the linear initial value problem (IVP) to be studied, and begin to reexamine the stability analysis of this popular vortex model. Then, in Chapter 3, we complete the exponential instability analysis for the three-region model, noting the existence of and describing the mechanisms behind a wavenumber-2 instability. From there, we derive the complete solution to the linear IVP in Chapter 4, examining the asymptotic (long time) nature of those solutions and inquiring whether these small perturbations affect the stability of the vortex.

Chapter 5 continues the analytical study by examining the wave-mean flow interactions due to eddy vorticity fluxes diagnosed from the linear solution to the IVP (frequently referred to as quasi-linear dynamics) for the three-region model. To aid in solidifying ideas, we focus on the dynamics of a Rankine vortex surrounded by a monochromatic sheared disturbance, using a numerical model to quantify the effects these perturbations have. Here, we find that the quasi-linear dynamics show significant amplifications of mean flow accelerations in the vicinity of the sheared disturbances and also point to the importance of critical radii. We then note some limitations on the use of purely quasi-linear over fully nonlinear theory, especially in resonance (critical radius) cases, tying this in specifically with the ideas of resonant damping that have been recently developed. Conclusions from this work are provided in Chapter 6.

Chapter 2

LINEAR ANALYSIS

2.1 Model Setup

The two-dimensional Euler equations (see equations (2.1)) for fluid flow are a useful starting point for examining flows that are strongly vortical. Formally speaking, if a flow has Ekman, Rossby and temporal Rossby numbers that are small compared to unity, the Taylor-Proudman theorem can be invoked and the flow tends to be vertically rigid. Such flows tend to move in vertical columns, implying that they are governed by the dynamics in the two non-vertical dimensions. Although some of the phenomenon we wish to study have local Rossby numbers much greater than unity, this model framework still serves as a useful starting place for basic understanding of vortex dynamics.

Despite their simplicity, however, a substantial amount of physics can still be found in these equations, even though they filter out certain physical phenomena like gravity waves, cloud microphysical processes, or frictional and diffusive effects. This simple analytical framework will provide a basic understanding of potentially important processes that affect strongly vortical flows.

Two-dimensional Euler equations in cylindrical coordinates

$$
\begin{aligned}
&\textbf{Radial Momentum} && \frac{\partial u}{\partial t} + u\frac{\partial u}{\partial r} + \frac{v}{r}\frac{\partial u}{\partial \lambda} - \frac{v^2}{r} = -\frac{1}{\rho}\frac{\partial p}{\partial r} \\
&\textbf{Azimuthal Momentum} && \frac{\partial v}{\partial t} + u\frac{\partial v}{\partial r} + \frac{v}{r}\frac{\partial v}{\partial \lambda} + \frac{uv}{r} = -\frac{1}{\rho r}\frac{\partial p}{\partial \lambda} \\
&\textbf{Mass Conservation} && \frac{\partial \rho}{\partial t} + \frac{1}{r}\frac{\partial (r\rho u)}{\partial r} + \frac{1}{r}\frac{\partial (\rho v)}{\partial \lambda} = 0
\end{aligned}
\tag{2.1}
$$

We start by assuming that the fluid is homogeneous and incompressible (i.e. ρ is constant in time and space). This constraint is equivalent to the application of the Boussinesq approximation in our two-dimensional system. It also implies that the flow is nondivergent, i.e.

$$\frac{1}{r}\frac{\partial(ru)}{\partial r} + \frac{1}{r}\frac{\partial v}{\partial \lambda} = 0. \tag{2.2}$$

With any set of equations, it is advantageous to reduce the number of prognostic equations in favor of diagnostic equations. In the two-dimensional Euler equations, this can be easily accomplished by forming the vorticity equation from the two momentum equations in (2.1). Cross-differentiating, we find that the vorticity (denoted as ζ) satisfies

$$\frac{\partial \zeta}{\partial t} + u\frac{\partial \zeta}{\partial r} + \frac{v}{r}\frac{\partial \zeta}{\partial \lambda} = 0, \tag{2.3}$$

where

$$\zeta = \frac{\partial(rv)}{r\partial r} - \frac{\partial u}{r\partial \lambda}.$$

Vorticity is, thus, materially conserved. This material conservation property, in addition to the removal of the pressure terms from our prognostic equation, is why vorticity is one of the most important variables in the Euler equations. However, u and v are still involved in this formulation. To make this equation self-contained, we note that since the flow is non-divergent (i.e. (2.2)), we can define a streamfunction ψ such that $-(\partial\psi/r\partial\lambda) = u$ and $(\partial\psi/\partial r) = v$. It is easy to show that vorticity and streamfunction are also related:

$$\zeta = \frac{\partial(rv)}{r\partial r} - \frac{\partial u}{r\partial \lambda} = \frac{\partial}{r\partial r}\left(r\frac{\partial \psi}{\partial r}\right) + \frac{1}{r^2}\frac{\partial^2 \psi}{\partial \lambda^2} = \nabla^2\psi.$$

This allows us to focus on solving one prognostic equation and diagnose the rest of the fluid properties from the solutions to that equation:

$$\left(\frac{\partial}{\partial t} - \frac{\partial \psi}{r\partial \lambda}\frac{\partial}{\partial r} + \frac{\partial \psi}{r\partial r}\frac{\partial}{\partial \lambda}\right)\nabla^2\psi = 0. \tag{2.4}$$

Next, since we would like to examine circular vortices, we assume that we have a basic state circular flow with perturbations superimposed on it. Henceforth, we will be working

with the perturbation equations in a cylindrical coordinate system, assuming some mean circular flow. Therefore, barred quantities, i.e. $\bar{v}$, will be assumed to be azimuthal averages, i.e.

$$\bar{v}(r,t) = \frac{1}{2\pi}\int_0^{2\pi} v(\lambda,r,t)d\lambda \tag{2.5}$$

and primed quantities, i.e. $v'(\lambda,r,t)$, are perturbations, or differences of the total from this azimuthal average. For Chapters 2, 3, and 4, we will assume that all mean quantities are constant in t. Chapter 5 will address temporal changes in the mean vortex.

Since the flow is assumed to be nondivergent, it follows that $\bar{u} = 0$. The mean vorticity ($\bar{\zeta}$) is then $\bar{\zeta} = \partial(r\bar{v})/r\partial r$.

As mentioned in the introduction, we wish study the interactions between perturbations on sharp mean vorticity gradients, perturbations outside these mean gradients, and the mean vorticity gradients themselves. Many previous works have focused on the interactions between the perturbations on sharp gradients but have not included any other perturbations outside these gradients. Other works have studied the effects perturbations may have on a mean vortex, but in absence of sharp mean gradients. It is from the stance of providing a more complete solution to this analytically simple problem that we continue.

We set up our basic state vortex with the three-region piecewise constant vorticity model studied by Michalke and Timme (1967), Vladimirov and Tarasov (1980) [hereafter VT80], Lugovtsov (1982), F88, Dritschel (1989), and S99. This is the simplest model that allows for interaction between multiple sharp vorticity gradients and is inspired by vortices similar to the hurricane vortex in Figure 1.2. Since this basic state model has been studied frequently before, we will be able to compare and contrast our results with those previous studies. However, here we will employ a more general version of this model than had been previously studied, allowing the vorticity to take on any constant value in each of the three regions. Denoting the environmental vorticity as C, the radial vorticity distribution is given by:

$$\bar{\zeta}(r) = \frac{\partial(r\bar{v})}{r\partial r} = \begin{cases} \xi_1 + \xi_2 + C & 0 < r < r_1, \\ \xi_2 + C & r_1 < r < r_2, \\ C & r_2 < r < \infty. \end{cases}$$

where ξ_1, ξ_2, r_1, r_2 are constants. Respectively, ξ_1 and ξ_2 are the vorticity jumps at the inner and outer interfaces. The tangential wind ($\bar{v}$) and the angular velocity ($\bar{\Omega}$) profiles consistent with this vorticity profile are:

$$\bar{v}(r) = \frac{1}{2r} \begin{cases} \xi_1 r^2 + \xi_2 r^2 + C r^2 & 0 \le r \le r_1, \\ \xi_1 r_1^2 + \xi_2 r^2 + C r^2 & r_1 \le r \le r_2, \\ \xi_1 r_1^2 + \xi_2 r_2^2 + C r^2 & r_2 \le r \le \infty. \end{cases}$$

$$\bar{\Omega}(r) = \frac{1}{2} \begin{cases} \xi_1 + \xi_2 + C & 0 \le r \le r_1, \\ \xi_1 \left(\frac{r_1}{r}\right)^2 + \xi_2 + C & r_1 \le r \le r_2, \\ \xi_1 \left(\frac{r_1}{r}\right)^2 + \xi_2 \left(\frac{r_2}{r}\right)^2 + C & r_2 \le r \le \infty. \end{cases} \tag{2.6}$$

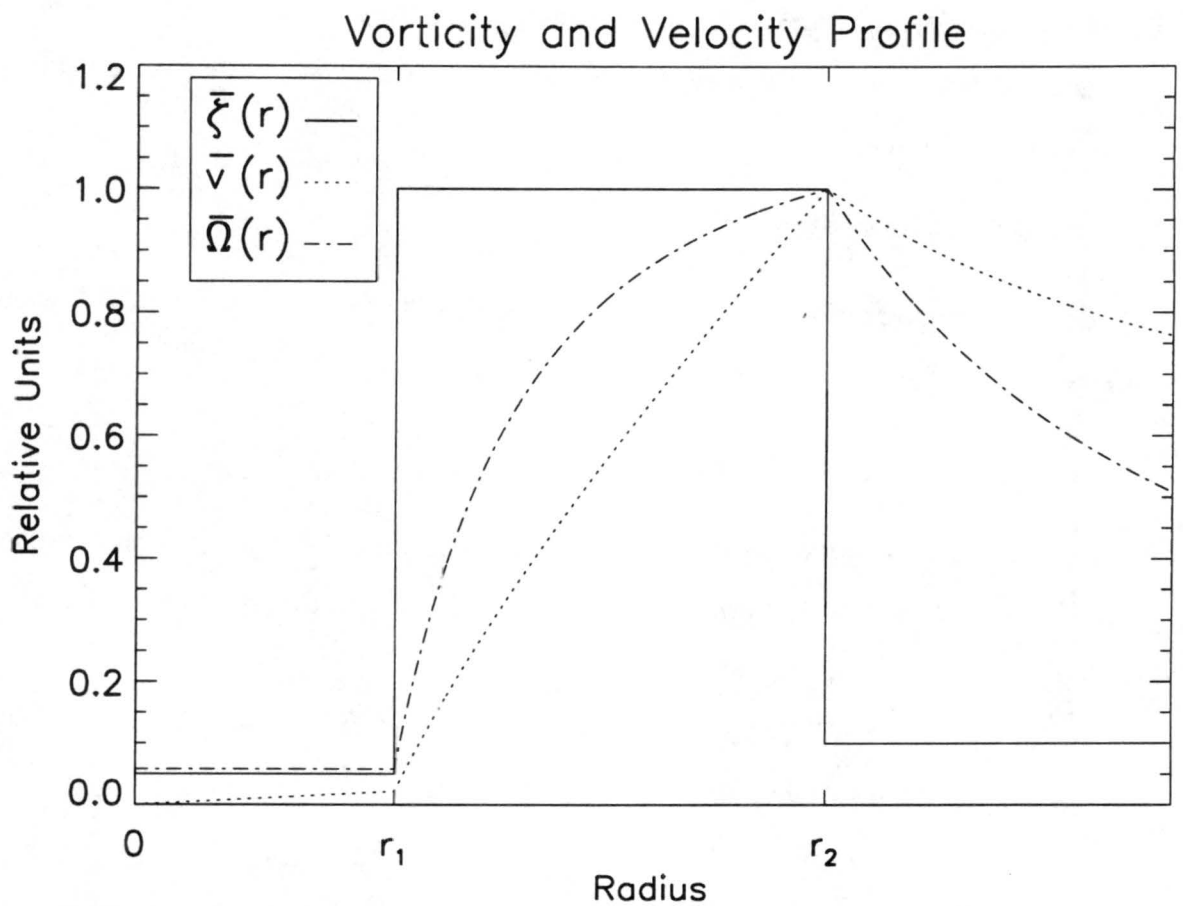

Figure 2.1: The generalized three-region basic-state model's velocity ($\bar{v}$), vorticity ($\bar{\zeta}$), and angular velocity ($\bar{\Omega}$) for a case where $\xi_2 = 9C$ and $\xi_1 = -9.5C$. All values are relative to the maximum of each field.

For an illustration of a sample of this model, see Figure 2.1. When discussing this model, we refer to the region $0 \le r \le r_1$ as the "inner region", the region $r_1 \le r \le r_2$ as

the "annulus", and the region $r_2 \leq r < \infty$ as the "environment". Also, the terms "inner interface" and "outer interface" refer to r_1 and r_2, respectively, where the vorticity jumps are found.

Note that if $C \neq 0$, then $\bar{v} \to \infty$ as $r \to \infty$. We are most interested, however, in the dynamics in the finite region near the center of circulation, effectively making this point at infinity dynamically inert.

It is known that solutions of the Euler equations are invariant with respect to a globally uniform vorticity, i.e. C. Therefore, the fundamental nature of our solutions will not change if we were to reduce the vorticity in the domain by C, making our solutions valid even in the similar compact cases. However, for the sake of generality, we will continue using a potentially non-zero C.

2.2 Analytical First Steps

Before beginning the stability analysis, it is useful and convenient to define additional parameters. Let δ and ϵ be ratios which classify the basic state vortex:

$$\delta = \frac{r_1}{r_2} < 1, \qquad \epsilon = -\frac{\xi_2}{\xi_1}.$$

Here, δ is the spacial ratio that defines the width of the annulus. ϵ is a vorticity scaling factor that influences the strength of discrete perturbations due to radial winds. The sign convention for ϵ will be explained in Chapter 3.

It can be shown that the perturbation streamfunction (ψ') and perturbation vorticity (ζ') are related in the following way:

$$\zeta' = \frac{\partial(rv')}{r\partial r} - \frac{\partial u'}{r\partial \lambda} = \frac{\partial}{r\partial r}\left(r\frac{\partial \psi'}{\partial r}\right) + \frac{1}{r^2}\frac{\partial^2 \psi'}{\partial \lambda^2} = \nabla^2 \psi'.$$

Using this and transforming our equations into streamfunction evolution equations and splitting the total streamfunction into mean and perturbation components, we can create a perturbation vorticity equation by combining the perturbation momentum equations.

Next, we assume that perturbations of the streamfunction are small compared to the magnitude of the mean streamfunction. This assumption allows us to linearize the perturbation vorticity equation to get the linearized, barotropic, nondivergent, two-dimensional vorticity equation in cylindrical coordinates (λ, r):

$$\left(\frac{\partial}{\partial t} + \bar{\Omega}(r)\frac{\partial}{\partial \lambda}\right)\nabla^2\psi' - \frac{\partial \psi'}{r\partial\lambda}\frac{\partial \bar{\zeta}}{\partial r} = 0. \tag{2.7}$$

Assuming our three-region model as the basic-state vortex, we note that $d\bar{\zeta}/dr = 0$ at every point except $r = r_1, r_2$. Thus, (2.7) becomes

$$\left(\frac{\partial}{\partial t} + \bar{\Omega}\frac{\partial}{\partial \lambda}\right)\zeta' = 0, \qquad r \neq r_1, r_2. \tag{2.8}$$

As we stated before, we strive to make this analysis as general and complete as possible. Therefore, we will allow for a group of perturbation vorticity solutions that not only include the traditional discrete vorticity waves on the interfaces, but also include a general smooth vorticity perturbation. Here, we follow the analysis of Smith and Montgomery (1995, Sec. 5) and split the perturbation vorticity into three linear parts to account for the discrete jumps at each interface and the remaining smooth perturbation. Therefore, we will assume that $\zeta' = \zeta'_s + \zeta'_1 + \zeta'_2$ where ζ'_s is smooth for all r, ζ'_1 accounts for the discontinuity at r_1 and vanishes elsewhere, and ζ'_2 accounts for the discontinuity at r_2 and vanishes elsewhere. Similarly, we will split the perturbation streamfunction into three related pieces: $\psi' = \psi'_s + \psi'_1 + \psi'_2$, where $\zeta'_i = \nabla^2\psi'_i$ for $i = 1, 2, s$.

A few comments are warranted about this split of the perturbation. First, ζ'_1 and ζ'_2 will be called the "discrete modes". They represent the deformation of the interfaces of the constant vorticity regions from their initially circular configurations. These are produced by radial advection of the basic state vortex as given by the last term on the left-hand side of (2.7). We call this part of the equation "perturbation generation." Second, since the smooth portion exists in a region with no mean vorticity gradient, the smooth portion will be sheared apart exclusively by the differential rotation of the mean circular flow (cf. Figure 1.4 and (2.8)). Thus, perturbation radial winds in these linearized dynamics can only produce

discrete mode perturbations, not smooth perturbations. This makes the evolution of the smooth perturbation rather simple in the linear dynamics. It will be shown, however, that this well-understood shearing mechanism (called the Orr mechanism (Orr, 1907; Lindzen, 1990)), through wave-mean flow interaction, can still influence the dynamics of the system as a whole. We will consider this further in Chapter 5.

Continuing with the linear analysis, we note that (2.7) splits naturally into

$$\begin{cases} \left(\dfrac{\partial}{\partial t} + \bar{\Omega}\dfrac{\partial}{\partial \lambda}\right)\zeta_s' = 0, & \text{for all } r; \\ \left(\dfrac{\partial}{\partial t} + \bar{\Omega}\dfrac{\partial}{\partial \lambda}\right)\zeta_1' = 0, & \text{for all } r \neq r_1; \\ \left(\dfrac{\partial}{\partial t} + \bar{\Omega}\dfrac{\partial}{\partial \lambda}\right)\zeta_2' = 0, & \text{for all } r \neq r_2; \end{cases} \tag{2.9}$$

We next apply a discrete Fourier transform to all perturbation quantities (represented below as f') in the azimuth,

$$f'(\lambda, r, t) = \mathrm{Re}\left[\sum_{\substack{n=-\infty \\ n\neq 0}}^{\infty} \hat{f}_n(r,t)e^{in\lambda}\right], \tag{2.10}$$

to transform the equations into azimuthal wavenumber space. We use a discrete transform since the nature of cylindrical coordinates require n to be integral, and we ignore the $n = 0$ contribution since that term represents the azimuthal mean. Also, for notational convenience, we will drop the n subscript and assume that all hatted quantities depend on n. One more restriction we will impose is the limiting of our scope to one wavenumber at a time, since it simplifies the analysis and since the linear dynamics do not allow waves to interact with each other to produce waves outside of wavenumber-n. Thus, we will assume that n is some fixed non-zero integer.

The Fourier space equivalents to the equations for ζ_1' and ζ_2' in (2.9) are, then,

$$\begin{cases} \left(\dfrac{\partial}{\partial t} + in\bar{\Omega}\right)\hat{\zeta}_1 = 0, & r \neq r_1 \\ \left(\dfrac{\partial}{\partial t} + in\bar{\Omega}\right)\hat{\zeta}_2 = 0, & r \neq r_2. \end{cases} \tag{2.11}$$

Since $|\hat{\zeta}_1|$ and $|\hat{\zeta}_2|$ represent the radial structure of the discrete modes, and since the discrete modes vanish at every point outside of their respective radii, we follow SM95 and assume

$$\begin{cases} \hat{\zeta}_1 = \gamma_1(t)\delta^*(r - r_1) \\ \hat{\zeta}_2 = \gamma_2(t)\delta^*(r - r_2), \end{cases}$$

where $\delta^*(r)$ is the usual Dirac delta function. These solutions are constructed to satisfy the jump conditions needed for the discrete modes ζ_1' and ζ_2'.

γ_1 and γ_2, physically, represent the time dependent magnitude and phase of the discrete waves on the inner and outer interfaces, respectively. To see this, assume that $\gamma_1(t) = |A(t)|e^{iBt}$. $A(t)$ represents the amplitude, or strength, of the inner interface's discrete wave, while the phase shift of the wave is given by e^{iBt}. Since these are the only time dependent portions of the discrete modes, we will focus our attention on solving for these γ functions.

Recalling that in this model, $\zeta_1' = \nabla^2\psi_1'$ and $\zeta_2' = \nabla^2\psi_2'$, it can be shown, using (2.2) and (2.10), that $\hat{\psi}_1 = \gamma_1(t)\hat{\Psi}_1(r)$ and $\hat{\psi}_2 = \gamma_2(t)\hat{\Psi}_2(r)$ where the functions $\hat{\Psi}_1(r)$ and $\hat{\Psi}_2(r)$ satisfy

$$\begin{cases} \left[\dfrac{d}{r\,dr}\left(r\dfrac{d}{dr}\right) - \dfrac{n^2}{r^2}\right]\hat{\Psi}_1 = \delta^*(r - r_1), \\ \left[\dfrac{d}{r\,dr}\left(r\dfrac{d}{dr}\right) - \dfrac{n^2}{r^2}\right]\hat{\Psi}_2 = \delta^*(r - r_2). \end{cases}$$

These differential equations represent the radial structure for the discrete waves' streamfunction. To mathematically complete this solution, the kinematic boundary condition at each interface requires that the perturbation radial velocity be continuous across it. Therefore, $\hat{\Psi}_1$ and $\hat{\Psi}_2$ must be continuous at the interface radii. We also assume that the delta function has a unit strength. With these conditions in place, we can complete the solution for the radial streamfunction equations to obtain

$$\hat{\Psi}_1(r) = -\frac{r_1}{2n}\begin{cases} \left(\dfrac{r}{r_1}\right)^n & 0 \le r \le r_1, \\ \left(\dfrac{r_1}{r}\right)^n & r_1 \le r \le \infty, \end{cases} \tag{2.12}$$

$$\hat{\Psi}_2(r) = -\frac{r_2}{2n}\begin{cases} \left(\dfrac{r}{r_2}\right)^n & 0 \le r \le r_2, \\ \left(\dfrac{r_2}{r}\right)^n & r_2 \le r \le \infty. \end{cases} \tag{2.13}$$

Lastly, we must find the solution to the first equation in (2.9) in Fourier space. This equation tells us, first, that

$$\zeta_s' = \zeta_{s0}'(\lambda, r)e^{-in\bar{\Omega}(r)t}, \tag{2.14}$$

where ζ_{s0}' is the initial ($t = 0$) smooth vorticity perturbation, which we assume to be given in the problem. Since our prognostic equation (2.4) is in terms of streamfunction, however, we need to solve for $\psi_s(\lambda, r, t)$. We reduce the Laplacian operator in Fourier space to get the following differential equation for $\hat{\psi}_s(r, t)$:

$$\left[\frac{\partial}{\partial r}\left(r\frac{\partial}{\partial r}\right) - \frac{n^2}{r}\right]\hat{\psi}_s(r,t) = r\hat{\zeta}_{s0}(r)e^{-in\bar{\Omega}(r)t}. \tag{2.15}$$

We also assume that our streamfunction vanishes at the origin ($\hat{\psi}_s(0,t) = 0$) and out to infinity ($\hat{\psi}_s(\infty,t) = 0$).

This differential equation can be solved using Green function theory (Carr and Williams, 1989; Zwillinger, 1998, pg. 288-296). The solution to this will be given by

$$\hat{\psi}_s(r,t) = \int_0^\infty \rho\hat{\zeta}_{s0}(\rho)e^{-in\bar{\Omega}(\rho)t}G(r,\rho)d\rho \tag{2.16}$$

where $G(r, \rho)$ is the Green function that is to be determined.

According to theory, if we have non-trivial solutions $Y_1(r)$ and $Y_2(r)$ such that

$$\left[\frac{d}{dr}\left(r\frac{d}{dr}\right) - \frac{n^2}{r}\right]Y_1(r) = 0 \quad \text{and} \quad Y_1(0) = 0,$$

$$\left[\frac{d}{dr}\left(r\frac{d}{dr}\right) - \frac{n^2}{r}\right]Y_2(r) = 0 \quad \text{and} \quad Y_2(\infty) = 0, \tag{2.17}$$

then the Green function is given by

$$G(r,\rho) = \begin{cases} \dfrac{Y_1(r)Y_2(\rho)}{\rho W(\rho)} & 0 \le r \le \rho, \\ \dfrac{Y_2(r)Y_1(\rho)}{\rho W(\rho)} & \rho \le r < \infty, \end{cases}$$

where $W(\rho) = Y_1(\rho)(dY_2(\rho)/dr) - Y_2(\rho)(dY_1(\rho)/dr)$ is the Wronskian of Y_1 and Y_2 at $r = \rho$.

If we assume that $Y_1(r)$ and $Y_2(r)$ have the form r^k, then we can see, using (2.17) that $Y_1 = r^n$ and $Y_2 = r^{-n}$, assuming that $n > 0$.

Therefore, we are able to show that

$$\hat{\psi}_s(r,t) = \int_0^\infty G(r,\rho)\hat{\zeta}_{s0}(\rho)e^{-int\bar{\Omega}(\rho)}\rho d\rho, \tag{2.18}$$

where

$$G(r,\rho) = -\frac{1}{2n}\begin{cases} \left(\frac{r}{\rho}\right)^n & 0 \le r \le \rho, \\ \left(\frac{\rho}{r}\right)^n & \rho \le r < \infty. \end{cases}$$

Having now solved for each of the streamfunction pieces, we can now write the total perturbation Fourier streamfunction as:

$$\hat{\psi}(r,t) = \hat{\psi}_s(r,t) + \gamma_1(t)\hat{\Psi}_1(r) + \gamma_2(t)\hat{\Psi}_2(r). \tag{2.19}$$

This gives us the Fourier components of the perturbation winds:

$$\hat{u} = -\frac{in}{r}\hat{\psi} = -\frac{in}{r}\hat{\psi}_s - \gamma_1\frac{in}{r}\hat{\Psi}_1 - \gamma_2\frac{in}{r}\hat{\Psi}_2, \tag{2.20}$$

$$\hat{v} = \frac{\partial\hat{\psi}}{\partial r} = \frac{\partial\hat{\psi}_s}{\partial r} + \gamma_1\frac{d\hat{\Psi}_1}{dr} + \gamma_2\frac{d\hat{\Psi}_2}{dr}. \tag{2.21}$$

We now examine the evolution of the waves in time. So, we begin with the linearized azimuthal momentum equation in this model,

$$\frac{\partial v'}{\partial t} + \bar{v}\frac{\partial v'}{r\partial\lambda} + u'\bar{\zeta} = -\frac{\partial p'}{r\partial\lambda},$$

which can be expressed in Fourier space as

$$\frac{\partial\hat{v}}{\partial t} + in\bar{\Omega}\hat{v} + \bar{\zeta}\hat{u} = \frac{in}{r}\hat{p}. \tag{2.22}$$

Assuming the perturbation pressure is continuous across r_1 and r_2 and evaluating this on each side of r_1 and r_2, then taking the difference, we obtain

$$\begin{cases} \frac{\partial}{\partial t}\left(\hat{v}(r_1^+) - \hat{v}(r_1^-)\right) + in\left[\bar{\Omega}(r_1^+)\hat{v}(r_1^+) - \bar{\Omega}(r_1^-)\hat{v}(r_1^-)\right] + \left[\bar{\zeta}(r_1^+)\hat{u}(r_1^+) - \bar{\zeta}(r_1^-)\hat{u}(r_1^-)\right] = 0 \\ \frac{\partial}{\partial t}\left(\hat{v}(r_2^+) - \hat{v}(r_2^-)\right) + in\left[\bar{\Omega}(r_2^+)\hat{v}(r_2^+) - \bar{\Omega}(r_2^-)\hat{v}(r_2^-)\right] + \left[\bar{\zeta}(r_2^+)\hat{u}(r_2^+) - \bar{\zeta}(r_2^-)\hat{u}(r_2^-)\right] = 0. \end{cases}$$

where r_i^+ and r_i^- are radii infinitesimally larger and smaller than r_i, respectively.

Now, recalling that $\bar{\Omega}$ and $\hat{u}$ are continuous over both jumps, we simplify this to

$$\begin{cases} \left[\dfrac{\partial}{\partial t} + in\bar{\Omega}(r_1)\right][\hat{v}(r_1^+) - \hat{v}(r_1^-)] - \xi_1\hat{u}(r_1) = 0 \\ \left[\dfrac{\partial}{\partial t} + in\bar{\Omega}(r_2)\right][\hat{v}(r_2^+) - \hat{v}(r_2^-)] - \xi_2\hat{u}(r_2) = 0. \end{cases}$$

Recalling the definitions of $\hat{u}$ and $\hat{v}$ in terms of the total streamfunction, i.e. (2.20) and (2.21), respectively, we obtain

$$\begin{cases} \left[\dfrac{\partial}{\partial t} + in\bar{\Omega}(r_1)\right]\left[\dfrac{\partial\hat{\psi}}{\partial r}(r_1^+) - \dfrac{\partial\hat{\psi}}{\partial r}(r_1^-)\right] + \dfrac{in\xi_1}{r_1}\hat{\psi}(r_1) = 0 \\ \left[\dfrac{\partial}{\partial t} + in\bar{\Omega}(r_2)\right]\left[\dfrac{\partial\hat{\psi}}{\partial r}(r_2^+) - \dfrac{\partial\hat{\psi}}{\partial r}(r_2^-)\right] + \dfrac{in\xi_2}{r_2}\hat{\psi}(r_2) = 0. \end{cases} \tag{2.23}$$

However,

$$\frac{\partial\hat{\psi}}{\partial r}(r_1^+) - \frac{\partial\hat{\psi}}{\partial r}(r_1^-) = \gamma_1\left[\frac{d\hat{\Psi}_1}{dr}(r_1^+) - \frac{d\hat{\Psi}_1}{dr}(r_1^-)\right] = \gamma_1,$$

using the fact that $\hat{\psi}_s$ and $\hat{\Psi}_2$ have continuous radial derivatives at r_1 and using (2.13) for $\hat{\Psi}_1$.

Similarly,

$$\frac{\partial\hat{\psi}}{\partial r}(r_2^+) - \frac{\partial\hat{\psi}}{\partial r}(r_2^-) = \gamma_2\left[\frac{d\hat{\Psi}_2}{dr}(r_2^+) - \frac{d\hat{\Psi}_2}{dr}(r_2^-)\right] = \gamma_2.$$

Therefore, (2.23) becomes, after evaluating $\hat{\psi}$ at r_1 and r_2 (using (2.13) and (2.19)),

$$\begin{cases} \left[\dfrac{d}{dt} + in\bar{\Omega}(r_1)\right]\gamma_1 + \dfrac{in\xi_1}{r_1}\left[\hat{\psi}_s(r_1,t) + \gamma_1\left(-\dfrac{r_1}{2n}\right) + \gamma_2\left(-\dfrac{r_2}{2n}\delta^n\right)\right] = 0 \\ \left[\dfrac{d}{dt} + in\bar{\Omega}(r_2)\right]\gamma_2 + \dfrac{in\xi_2}{r_2}\left[\hat{\psi}_s(r_2,t) + \gamma_1\left(-\dfrac{r_1}{2n}\delta^n\right) + \gamma_2\left(-\dfrac{r_2}{2n}\right)\right] = 0. \end{cases}$$

Rearranging and regrouping terms, we get

$$\begin{cases} \dfrac{d}{dt}\gamma_1 + i\left[n\bar{\Omega}(r_1) - \dfrac{\xi_1}{2}\right]\gamma_1 + i\left[-\dfrac{\xi_1}{2}\delta^{n-1}\right]\gamma_2 = -i\left[\dfrac{n\xi_1}{r_1}\hat{\psi}_s(r_1,t)\right] \\ \dfrac{d}{dt}\gamma_2 + i\left[-\dfrac{\xi_2}{2}\delta^{n+1}\right]\gamma_1 + i\left[n\bar{\Omega}(r_2) - \dfrac{\xi_2}{2}\right]\gamma_2 = -i\left[\dfrac{n\xi_2}{r_2}\hat{\psi}_s(r_2,t)\right]. \end{cases} \tag{2.24}$$

Further defining

$$\begin{aligned} \nu_1 &= n\bar{\Omega}(r_1) - \frac{\xi_1}{2} & \nu_2 &= n\bar{\Omega}(r_2) - \frac{\xi_2}{2} \\ \mu_1 &= -\left(\frac{\xi_1}{2}\right)\delta^{n-1} & \mu_2 &= -\left(\frac{\xi_2}{2}\right)\delta^{n+1} \\ \alpha_1(t) &= -\left(\frac{n\xi_1}{r_1}\right)\hat{\psi}_s(r_1,t) & \alpha_2(t) &= -\left(\frac{n\xi_2}{r_2}\right)\hat{\psi}_s(r_2,t), \end{aligned} \tag{2.25}$$

we can rewrite (2.24) as:

$$\begin{cases} \left[\dfrac{d}{dt} + i\nu_1\right]\gamma_1 + i\mu_1\gamma_2 = i\alpha_1(t) \\ \left[\dfrac{d}{dt} + i\nu_2\right]\gamma_2 + i\mu_2\gamma_1 = i\alpha_2(t). \end{cases} \tag{2.26}$$

Equation (2.26) is the starting point for the rest of the analysis. This pair of coupled equations for the time-varying amplitudes of the discrete modes (γ_1, γ_2) encapsulates the linear physics of the system: the azimuthal rotation of each mode (first term on the left-hand side), the perturbation generation from the induced flow from the other interface's wave (last term on the left-hand side), and the perturbation generation from the sheared smooth perturbation (the right-hand side). We can now solve this coupled set of ordinary differential equations for γ_1. Since γ_1 and γ_2 are intimately connected (via (2.26)), we can focus entirely on solving for the inner interface's wave and deduce the properties of the outer wave from this solution.

Eliminating γ_2 from (2.26), we obtain

$$\left[\frac{d}{dt} + i\nu_2\right]\left[\frac{d}{dt} + i\nu_1\right]\gamma_1 + \mu_1\mu_2\gamma_1 = \left[\frac{d}{dt} + i\nu_2\right] i\alpha_1(t) + \mu_1\alpha_2(t)$$

which simplifies to

$$\left[\frac{d^2}{dt^2} + i(\nu_1 + \nu_2)\frac{d}{dt} - \nu_1\nu_2 + \mu_1\mu_2\right]\gamma_1 = \left[\frac{d}{dt} + i\nu_2\right] i\alpha_1(t) + \mu_1\alpha_2(t). \tag{2.27}$$

This is an inhomogeneous ordinary differential equation for γ_1. To find the homogeneous solutions, we assume that $\gamma_1 = C_1 e^{i\nu t}$. Using this solution in (2.27), we get the following equation for ν:

$$-\nu^2 - (\nu_1 + \nu_2)\nu + (\mu_1\mu_2 - \nu_1\nu_2) = 0.$$

ν represents the intrinsic frequencies of only the inner wave (since the solution is only for γ_1, or the amplitude function of the inner discrete wave). If ν is not purely real, then the pair of solutions will have the same azimuthal frequency, but one will grow exponentially in time while the other will decay exponentially. Otherwise, there will be two real solutions for

ν (excluding when the determinant of the above quadratic formula vanishes) which describe the rotation rates of the two waveforms that comprise the inner discrete wave.

Solving for ν, we obtain

$$\begin{aligned} \nu &= -\tfrac{1}{2}\left[(\nu_1+\nu_2) \pm \sqrt{(\nu_1+\nu_2)^2 + 4(\mu_1\mu_2 - \nu_1\nu_2)}\right] \\ &= -\tfrac{1}{2}\left[(\nu_1+\nu_2) \pm \sqrt{(\nu_1-\nu_2)^2 + \xi_1\xi_2\delta^{2n}}\right]. \end{aligned} \tag{2.28}$$

This is exactly the dispersion relation derived in S99 (their equation (2.10)), verifying our work up to this point.

In the next chapter, (2.28) will be examined more completely, leading into a discussion of the discrete mode exponential instabilities. From there, the analysis will be continued, focusing on the inhomogeneous solutions to (2.27) and, using asymptotic mathematics, attempting to find the leading behavior of any general disturbance to the vortex at long times. Lastly, the interactions of the waves on the mean flow will be studied to determine the spin-up/spin-down effect of the perturbations on the mean vortex.

Chapter 3

EXPONENTIAL INSTABILITIES

3.1 The Existence of Wavenumber-2 Exponential Instabilities

The classical discrete mode exponential instability for the three-region model has been analyzed in the past (Michalke and Timme, 1967; VT80; S99), but not to our knowledge in this sort of generalization. Here we complete this analysis and attempt to glean further information about the peculiar nature of this three-region model.

We begin with the necessary condition for discrete mode exponential instabilities: Rayleigh's condition. Rayleigh's condition for shear instabilities in the analogous continuous model requires the vorticity gradient to change sign somewhere in the domain (Michalke and Timme, 1967; Gent and McWilliams, 1986). The similar condition is satisfied in this discrete model when the jumps ξ_1 and ξ_2 are of different sign. We will therefore assume that ξ_1 and ξ_2 are of opposite sign for the remainder of this chapter. Note that this implies that $\epsilon > 0$.

Starting with the homogeneous solutions, let us assume that the smooth part of the perturbation vanishes. This method separates out the discrete modes from any sheared disturbance component that might also be present. Looking for exponential-type instabilities, we will assume that ν has a non-zero imaginary part, or that the discriminant of (2.28), hereafter called ν_D^2, is negative:

$$\nu_D^2 = (\nu_1 - \nu_2)^2 + \xi_1 \xi_2 \delta^{2n} < 0. \tag{3.1}$$

Looking first at some specific cases, we examine $n = 1$. Here, it can be shown, using (2.25) and (2.6), that $\nu_1 = \frac{1}{2}(\xi_2 + C)$ and $\nu_2 = \frac{1}{2}(\xi_1 \delta^2 + C)$. Thus, for the instability to

occur,

$$\frac{1}{4}(\xi_2 - \xi_1\delta^2)^2 + \xi_1\xi_2\delta^2 < 0$$

which can be simplified to

$$(\xi_2 + \xi_1\delta^2)^2 < 0. \tag{3.2}$$

This proves, by contradiction, that wavenumber-1 is exponentially stable in the generalized model. This is encouraging, since it replicates results from Reznik and Dewar (1994) in their appendix for a continuously distributed mean vortex profile. However, notice that if $(\xi_2 + \xi_1\delta^2) = 0$, then $\nu_D = 0$ for $n = 1$. This locus of "neutral" points will be discussed in a later analysis in Chapter 4, Section 3.

Turning our attention to $n = 2$, from (2.6), we obtain $\nu_1 = \frac{1}{2}\xi_1 + \xi_2 + C$ and $\nu_2 = \xi_1\delta^2 + \frac{1}{2}\xi_2 + C$. Trying to find instabilities, (3.1) gives us the instability criterion:

$$\left[\left(\frac{1}{2} - \delta^2\right)\xi_1 + \frac{1}{2}\xi_2\right]^2 + \xi_1\xi_2\delta^4 < 0,$$

or, equivalently,

$$(\xi_1 + \xi_2)^2 - 4\xi_1(\xi_1 + \xi_2)\delta^2 + 4\xi_1(\xi_1 + \xi_2)\delta^4 < 0. \tag{3.3}$$

Since the first term in the left-hand sum is non-negative, a necessary condition for the inequality to be satisfied is

$$4\xi_1(\xi_1 + \xi_2)\delta^4 < 4\xi_1(\xi_1 + \xi_2)\delta^2$$

or,

$$\xi_1(\xi_1 + \xi_2)\delta^2 < \xi_1(\xi_1 + \xi_2).$$

However, $0 < \delta < 1$, by definition. This implies that $\xi_1(\xi_1 + \xi_2) > 0$. Thus, for an instability to be possible in this model, $|\xi_2| < |\xi_1|$. If the opposite is true, we have stability. This is a necessary, but not sufficient, condition for instability of azimuthal wavenumber-2 disturbances in the three-region model. Note also that this condition does not require ξ_1 (or ξ_2) to have a specific sign. This implies that the criterion would be the same for depressed annuli (compared to the environment) as it is for elevated annuli.

For the class of vortices considered in S99 ($C = 0$, $\xi_1 < 0$, $\xi_2 > 0$; i.e. compact vortices with elevated vorticity in the annulus), the necessary condition requires negative vorticity in the inner region. In S99, though, the vorticity in the inner region was assumed positive in accordance with numerous flight level observations of the eye region of hurricanes. Thus, S99's class of vortices lies outside the necessary condition for wavenumber-2 exponential instability. It is precisely this condition that makes wavenumber-2 curiously absent from previous discrete waveguide analyses. Many previous works examined compact vortices with non-negative vorticity everywhere, thus excluding them *a priori* from supporting this instability. In this generalized model, however, the necessary condition, as well as the assumption of positive vorticity in the inner region, can both be fulfilled.

The necessary condition, as well as Rayleigh's condition, then implies that $0 < \epsilon < 1$. We reduce (3.3) to

$$4(1-\epsilon)\delta^4 - 4(1-\epsilon)\delta^2 + (1-\epsilon)^2 < 0. \tag{3.4}$$

Equation (3.4) is a quadratic equation in δ^2 with a positive coefficient on the squared (i.e. quartic) term. Thus, the inequality is satisfied for

$$\frac{1-\sqrt{\epsilon}}{2} < \delta^2 < \frac{1+\sqrt{\epsilon}}{2}. \tag{3.5}$$

This implies that if $|\xi_2| < |\xi_1|$ (necessary condition) and if our annular region has dimensions that fall into the proper ranges determined by the vorticity profile (3.5), a wavenumber-2 instability will occur. This relation between the ratio of the radii (δ) and the ratio of the vorticity jumps (ϵ) is the sufficient condition for this instability.

A similar result was first attained in VT80, assuming that the vorticity in the inner region is zero. Equation (3.5) generalizes their result by allowing non-zero vorticity in the inner region.

Despite working with the quasi-geostrophic approximation and compact vortices, F88 arrived at similar results in the barotropic limit which is mathematically isomorphic to the two-dimensional non-divergent model. Using $\Delta = \epsilon/(\epsilon-1)$ and $b = \delta^{-1}$, equations (3.4) and (3.5) are equivalent to F88's equation (3.7) and the result in F88's Sec. 3.1.i), respectively.

3.2 Exponential Growth Rates

Generalizing the result of Section 3.1 to arbitrary wavenumber-n, (2.28) may be rewritten, using (2.25), as:

$$\begin{aligned}\nu &= \frac{1}{4}\left[-\xi_1(1-n-n\delta^2+2n\epsilon+\epsilon)+2Cn\right] \\ &\quad \pm\frac{1}{4}\sqrt{(-\xi_1[1-n+n\delta^2-\epsilon])^2+4\xi_1^2\epsilon\delta^{2n}},\end{aligned}$$

or equivalently,

$$\nu = \frac{Cn}{2}+\frac{-\xi_1}{4}\left[(1-n-n\delta^2+2n\epsilon-\epsilon)\mp\sqrt{(1-n+n\delta^2+\epsilon)^2-4\epsilon\delta^{2n}}\right]. \quad (3.6)$$

This is the general criterion for instability. Instability occurs when the discriminant of (3.6) is less than zero:

$$(1-n+n\delta^2+\epsilon)^2-4\epsilon\delta^{2n}<0 \quad (3.7)$$

This condition is dependent on three parameters: n, δ, and ϵ. Because solutions in this two-dimensional model are known to be invariant with respect to uniform rotation, C only appears in the real (rotational) part of the complex frequency ν. Note further that for $n=2$, (3.7) reduces to (3.4). A criterion for the instability of wavenumber-n was previously derived by VT80 in the special case where $\epsilon=1$, i.e. the inner core vorticity is the same as the environment's:

$$F(n)=[n(1-x)-2]^2-4x^n<0,$$

where $x=(r_1/r_2)^2=\delta^2$. $F(n)$ is exactly the same as (3.7) in this special case.

Returning to the general case and examining the growth rate, we are only concerned about the positive imaginary part of (3.6):

$$\nu_i=\frac{|\xi_1|}{4}\sqrt{(1-n+n\delta^2+\epsilon)^2-4\epsilon\delta^{2n}}. \quad (3.8)$$

We now make ν_i dimensionless by dividing through by $|\xi_1|$. This is different than S99's formulation, where an average vorticity was used for scaling the growth rate. In

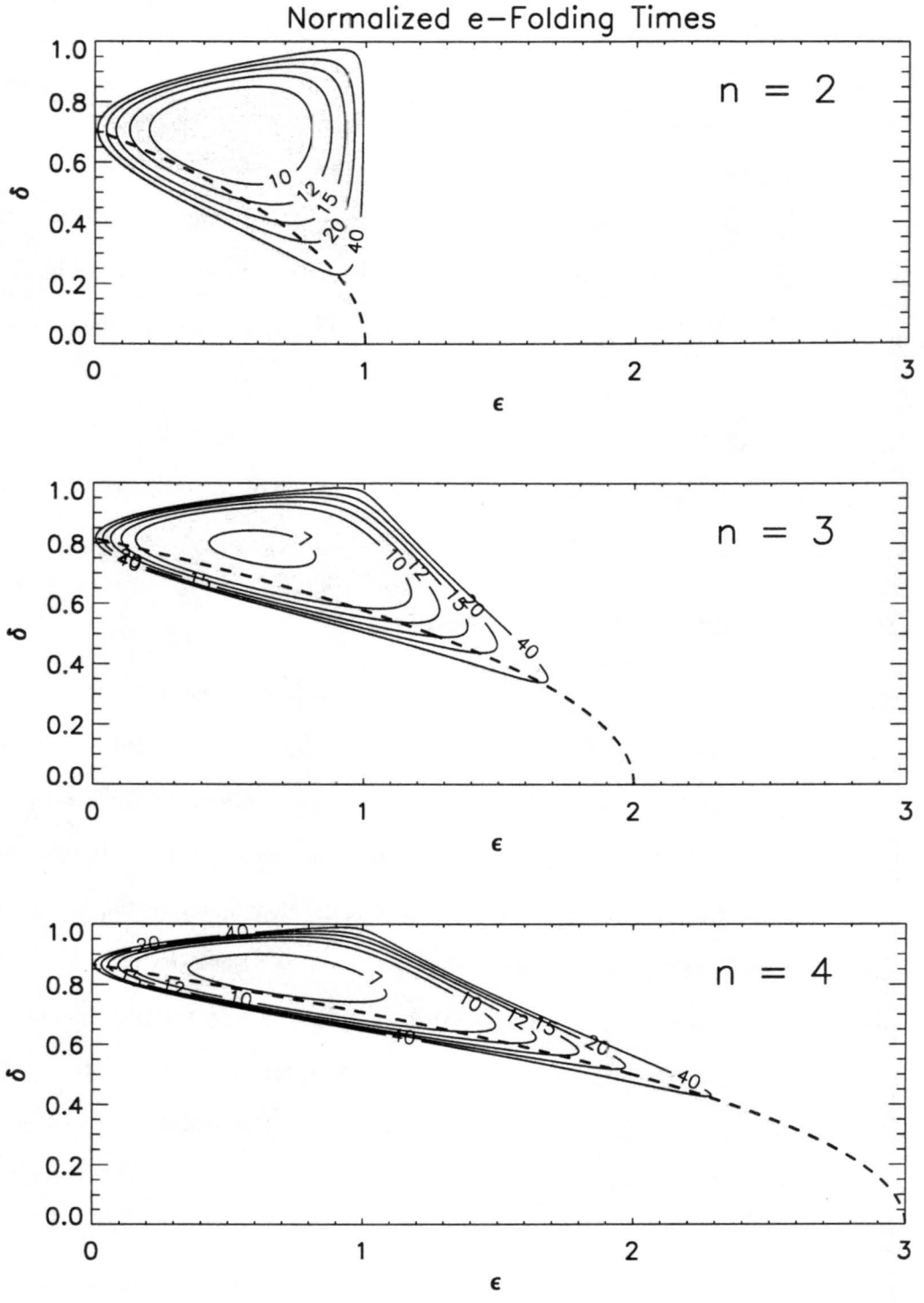

Figure 3.1: Normalized e-folding times for $n = 2, 3, 4$. Note that $n = 3, 4$ have an instability when $\epsilon > 1$, corresponding to most previous instability analyses. To get dimensional e-folding times, divide by $|\xi_1|$. The dashed line is the locus of points where $\nu_1 = \nu_2$, or where the waves are naturally phase-locked.

this case, the average vorticity adds complexity by making the scaled growth rate equation algebraically dependent on C.

Converting these normalized growth rates into normalized e-folding times, Figure 3.1 shows these e-folding times for wavenumbers-2, 3, and 4 in δ-ϵ space. Note that wavenumbers-3 and 4 have a tail that extends to $\epsilon > 1$, which corresponds to the instability discussed by S99. For wavenumber-2, however, there is no tail in the region $\epsilon > 1$. This is a restatement of the fact that the instability for wavenumber-2 is strictly confined to vortices with $\epsilon < 1$. As an example, take $\xi_1 = -10^{-2}$ s^{-1}, a realistic vorticity jump in a mature hurricane (Black and Marks, 1991; Kossin and Schubert, 2001, Figure 1). Thus, 10 units of normalized e-folding time correspond to a true e-folding time of 10^3 seconds, or about 16.7 minutes, which corresponds favorably to similar calculations in S99.

3.3 Discrete Vortex Rossby Wave Interpretation

The description of barotropic instabilities via phase-locked, counter-propagating vortex Rossby waves has proven useful in this model (S99) and other analogous models (Hoskins et al. 1985). As has been shown, vorticity gradients act as the waveguides for the instability; thus, we follow the lead of others and classify these waves as vortex Rossby waves. This concept proves useful for explaining how the $n = 2$ instability is supported by the waveguide. To do this, we require the non-interacting frequencies of these waves, i.e. the natural frequencies of these waves. Mathematically, these are obtained by forcing μ_1 and μ_2 from (2.25) to approach zero, since these terms are the multiplicative constants on the opposite waves in each wave's temporal differential equation (the pair of equations in (2.26)). Formally, this requires either $\delta \to 0$ (Rankine vortex) or $n \to \infty$. Thus, these frequencies are ν_1 and ν_2.

The phase-locked, non-interacting wave solution is obtained by equating ν_1 and ν_2 in (2.25). If $\nu_1 = \nu_2$, then for any n,

$$\frac{\xi_2}{\xi_1} = n\delta^2 - (n-1)$$

or equivalently,

$$\epsilon = (n-1) - n\delta^2. \tag{3.9}$$

The dashed curves plotted in Figure 3.1 correspond to the solution of (3.9) for varying n. Note that this locus of points lies entirely within the unstable region of interacting Rossby waves given by (3.7). We also note that (3.9) is equivalent to the result of F88 (his Sec. 3.1.iii), although in that context, the wavenumber was restricted to be greater than two.

We note that the definition $0 < \delta < 1$ implies, using (3.9), that $-1 < \epsilon < n-1$. This latter inequality implies the following consequences:

- For $n = 1$, the inequality states that for non-interacting waves to phase-lock, $\epsilon < 0$. This contradicts the requirement of non-negative ϵ implied by Rayleigh's condition. Thus, the wavenumber-1 Rossby waves cannot phase-lock in this model.

- For $n = 2$, non-interacting waves can phase-lock for $0 < \epsilon < 1$. This helps explain why $\epsilon = 1$ is a critical barrier for wavenumber-2.

- For $n > 2$, non-interacting waves can phase-lock for $0 < \epsilon < n-1$. This helps explain why the shaded regions in Figure 3.1 asymptote to $\epsilon = n-1$ as $\delta \to 0$.

Figure 3.2 shows the complete phase speeds of the interacting waves, which can be deduced from (3.6), in the frame of reference rotating with the environmental vorticity as a function of azimuthal wavenumber-n, for varying ϵ and δ. Where the curve bifurcates indicates the transition from instability to stability, as the two waves begin moving at different phase speeds and are not reinforcing each other's growth.

Also note the movement of the lesser n-bifurcation point as one changes values of ϵ. For $\epsilon < 1$, this n-bifurcation point is less than 2, while for $\epsilon > 1$, it is greater than 2, showing again that for wavenumber-2, $\epsilon = 1$ is a critical barrier.

Figure 3.3 shows regions where the instability occurs, as determined by (3.7) in n-ϵ space for varying values of δ. Note that all the regions' outlines in Figure 3.3 intersect at $(n, \epsilon) = (2, 1)$. Thus, for any δ, if $\epsilon < 1$, we enter into the unstable part of the curve at $n = 2$.

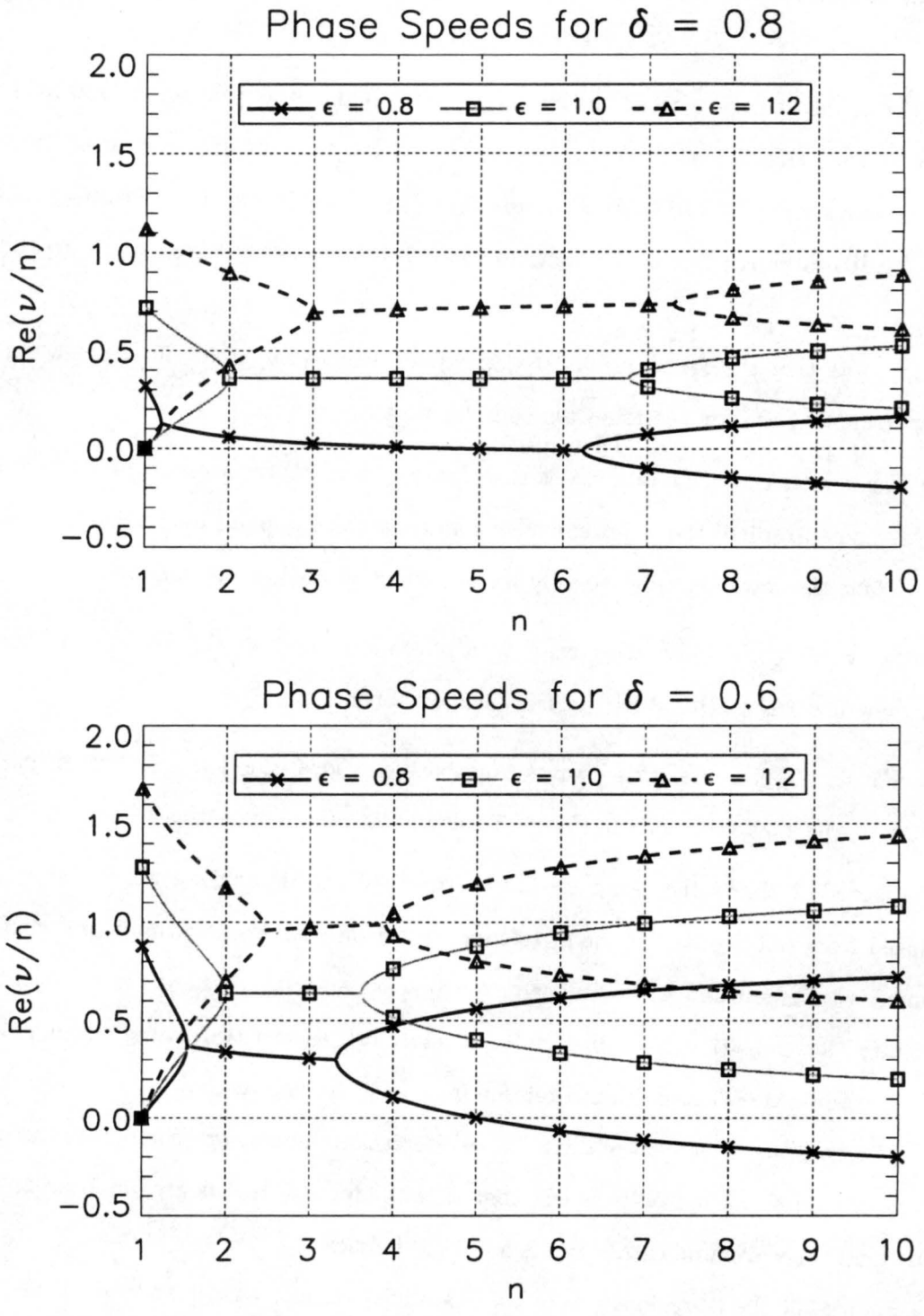

Figure 3.2: Phase speeds (i.e. $\mathrm{Re}(\nu/n)$) for varying values of ϵ and δ, in the frame of reference rotating with the environmental vorticity, e.g. assuming $C = 0$. Exponential instabilities occur where there is only one solution, indicating a pair of imaginary conjugate solutions.

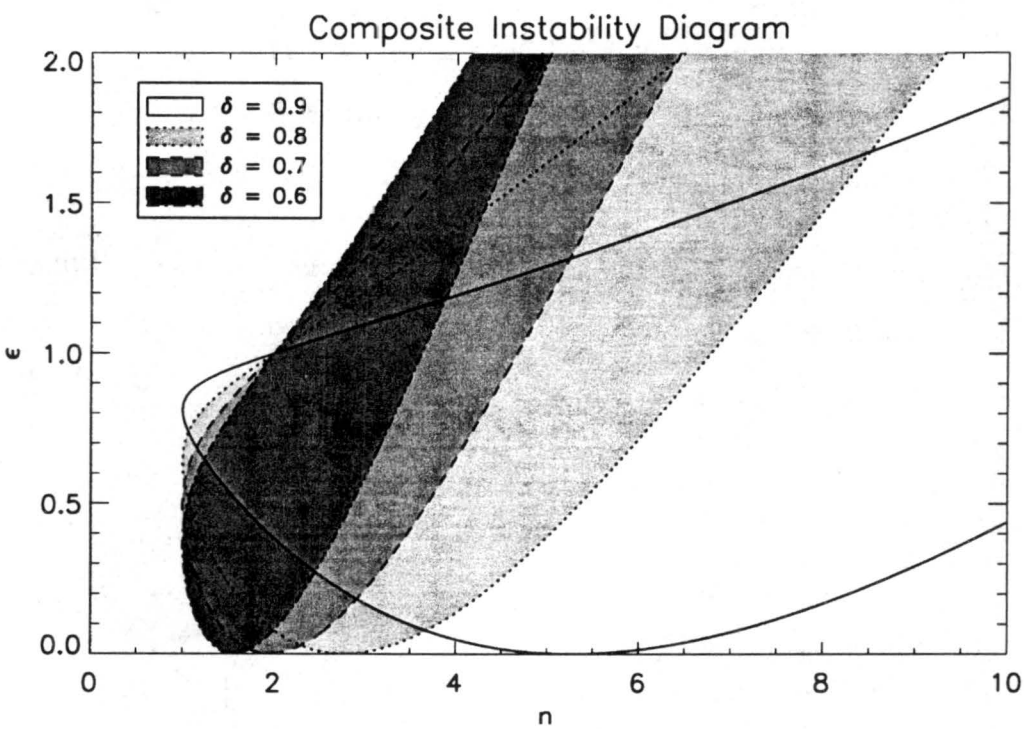

Figure 3.3: Regions in n-ϵ space where an exponential instability will occur, as determined by (3.7) for varying values of δ. Shading indicates instability. Note that for $n = 2$, all the plots are unstable for some ϵ-interval in [0,1].

3.4 Structure of Discrete Waves

Having now examined the conditions and growth rates of this instability, we focus attention on the perturbation streamfunction structure of this instability. Therefore, we will focus our attention on $\psi_1' + \psi_2'$, assuming for the moment that $\psi_s' = 0$ (which implies that $\hat{\psi}_s = 0$).

So,

$$\begin{aligned} \psi_1' + \psi_2' &= \mathrm{Re}\left[\left(\gamma_1(t)\hat{\Psi}_1(r) + \gamma_2(t)\hat{\Psi}_2(r)\right)e^{in\lambda}\right] \\ &= \mathrm{Re}\left[\gamma_1(t)\hat{\Psi}_1(r)e^{in\lambda} + \gamma_2(t)\hat{\Psi}_2(r)e^{in\lambda}\right] \end{aligned} \tag{3.10}$$

where $\hat{\Psi}_1$ and $\hat{\Psi}_2$ are defined in (2.12) and (2.13).

Now, using (2.26), we can find the relationship between γ_1 and γ_2. Using the first equation and using the assumed solution of $\gamma_1 = C_1 e^{i\nu t}$, where ν is determined from the vortex constants and wavenumber constraints through the dispersion relation (2.28), we see that

$$\gamma_2 = \frac{i\left[\frac{d}{dt} + i\nu_1\right]\gamma_1}{\mu_1} = -\frac{\nu + \nu_1}{\mu_1}\gamma_1. \tag{3.11}$$

So, we can rewrite (3.10) as

$$\begin{aligned} \psi_1' + \psi_2' &= \mathrm{Re}\left[\left(\hat{\Psi}_1(r) - \frac{\nu + \nu_1}{\mu_1}\hat{\Psi}_2(r)\right)\gamma_1(t)e^{in\lambda}\right] \\ &= \mathrm{Re}\left[\hat{\Psi}_1(r)\gamma_1(t)e^{in\lambda}\right] - \mathrm{Re}\left[\hat{\Psi}_2(r)\frac{\nu + \nu_1}{\mu_1}\gamma_1 e^{in\lambda}\right]. \end{aligned} \tag{3.12}$$

The first term represents the perturbation on the inner edge; the second term represents the outer edge's perturbation. Note that $\hat{\Psi}_1$ and $\hat{\Psi}_2$ do nothing to help determine the azimuthal structure of these waves since they are pure real. Recalling, though, that any complex number can be written in the form $e^{i\theta}$, we use this fact to simplify (3.12) to

$$\psi_1' + \psi_2' = \mathrm{Re}\left[\hat{\Psi}_1(r)\gamma_1(t)e^{in\lambda}\right] - \mathrm{Re}\left[\hat{\Psi}_2(r)\gamma_1(t)e^{in(\lambda+\theta')}\right], \tag{3.13}$$

where $e^{i\theta'} = (\nu + \nu_1)/(n\mu_1)$.

Since ν_1 and μ_1 are strictly real, the only way θ' will not equal 0 or π is if ν has some imaginary component. Thus, if ν has an imaginary component, i.e. there is an exponential instability, the outer wave is "phase-shifted" from the inner wave by an azimuthal angle θ'. This phase-shifting is important since it allows the waves to interact favorably, through the mean flow, to promote the other's growth and to promote the phase-locking required for further growth. Otherwise, if the streamfunction (and therefore vorticity) extrema are "stacked" in the radial direction, the generation of the perturbations will be inappropriately placed to facilitate the growth of the waves.

Figure 3.4 is a plot of $\psi' = \psi_1' + \psi_2'$ for $\delta = 0.5$ and $\epsilon = 0.875$, a configuration that is unstable in this model for wavenumber-2. We also assume that $\xi_1 < 0$ and $\xi_2 > 0$ to emulate a mature hurricane vortex. The annulus of elevated vorticity is shaded. To interpret this figure, recall that $\zeta' = \nabla^2\psi'$, and consequently, a negative ψ' lobe like the one that is marked corresponds to positive ζ'.

Let us first assume that the waves are non-interacting entities. The marked outer interface positive perturbation vorticity lobe induces a perturbation velocity field that advects higher vorticity (positive vorticity advection, or PVA) from the annulus on its southeastern side, and advects lower vorticity (negative vorticity advection, or NVA) from the environment on its northwestern side. This will tend to move the lobe clockwise, opposite the cyclonic flow on this interface (i.e. retrograde). On the inner interface, however, a similar analysis of induced flow will tend to propagate the disturbances cyclonically (i.e. prograde). In this way, the waves can potentially phase-lock, since the tangential flow is faster on the outer interface than the inner interface. (cf. (3.9)).

No longer assuming non-interaction of the waves, the perturbation flow induced by a wave on one interface can influence the wave on the other interface. This is the essence of (3.5), which gives the relation between the vorticity profile and the size of the annulus in which this wavenumber-2 instability can occur. This induced flow advects the basic state vorticity in such a way as to reinforce the waves on the other interface. In this indirect manner, the waves interact and aid each other's growth (e.g. Hoskins et al. 1985). In

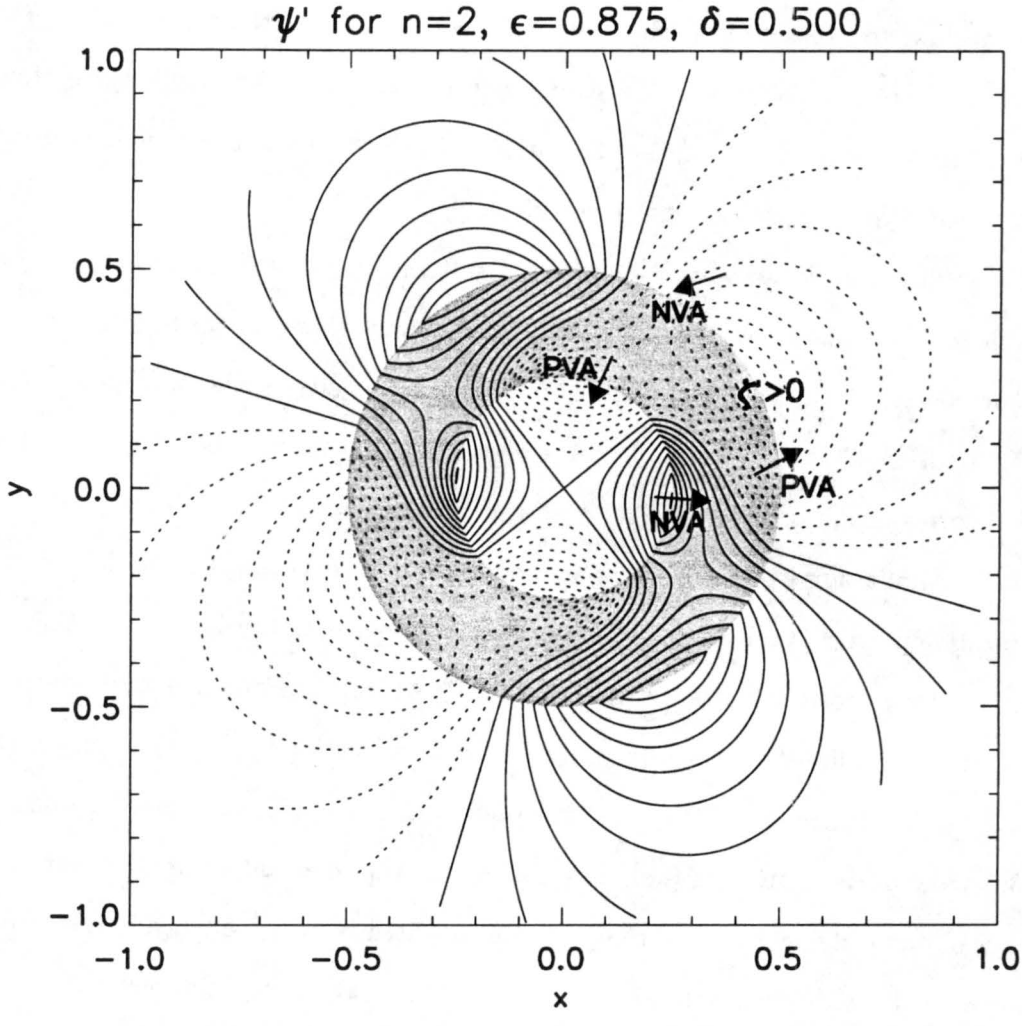

Figure 3.4: Sample plot of ψ'. Dashed contours indicate negative values of ψ'. The shaded region is the annular region. The annular region's vorticity here is assumed to be greater than the inner or outer regions' vorticity. Regions of positive and negative vorticity advections are denoted "PVA" and "NVA", respectively. Example perturbation winds are denoted by the arrows.

effect, this perturbation generation modifies each wave's phase speed, allowing the waves to remain phase-locked even when the non-interacting relation (3.9) is not satisfied. This interaction then creates an expanded envelope of instability around the solution plotted from (3.9) displayed in Figure 3.1. Mathematically, this envelope is the full instability criterion given by (3.7).

3.5 Discussion

Although a vortex similar to the generalized three-region model of Figure 2.1 is not necessarily realistic, our analysis nonetheless highlights some important points.

First, wavenumber-2 instabilities are not totally absent from the three-region model as commonly perceived. Most analyses of this model find no unstable wavenumber-2 modes (S99) mainly for the reason that the strictly non-negative compact vortex model automatically excludes those vortices that could support these modes. However, as noted before, wavenumber-2 instabilities had previously been found both in special cases (VT80) and in quasi-geostrophic formulations (F88) of this model. The theory here not only confirmed these works, but also extended them by considering a more general case of their model.

Second, while the assumption of non-zero vorticity in the outer region gives an unbounded tangential wind profile at large radii, this problem with extending this knowledge to real-world applications can be rectified in the context of discrete models if the generalized model is thought of as a limiting case of a discrete four-region model with zero environmental vorticity. Such a model has been formulated recently by Kossin et al. (2000, and refs. therein). When r_3 is large compared to r_1 and r_2, the interaction matrix in Kossin et al. approaches the interaction matrix of S99. This implies that the inclusion of this additional interface, if far enough from the other interfaces, will not fundamentally alter our analysis. A complete study of this four-region model and how it might apply to wavenumber-2 and higher instabilities with a depressed central core of vorticity might prove enlightening in the diagnosis of hurricane inner-core intensity change processes if used in conjunction with a continuous stability formulation.

Third, we would like to echo a quote from Balmforth et al. (2001): *"It is irritating that conclusions concerning important physical issues, such as the long-term relaxation of the streamfunction to axisymmetry, seem to turn on fussy mathematical restrictions concerning the smoothness or compactness of the vorticity profiles."* While, in this chapter, we are not studying the decay of perturbations and the return to axisymmetry but instead the growth of perturbations, their sentiments echo ours when we study this simple model. Indeed, that is one of the purposes of this work: to point out some more idiosyncrasies of this particular discrete vortex model. While we still gain important, yet basic, understanding of this instability from studying this simple model, we also point out the flaws inherent in it. For example, it is strange to think that an instability as common in continuous models and observed phenomenon would require $\epsilon < 1$ (or, in the case of compact vortices where the environmental vorticity is zero, that the core's vorticity must be negative) as a necessary criterion. Thus, while gaining basic understanding, we note that, realistically, much of this "fussy" mathematics serves only as a beginning guide for examining these instabilities.

Chapter 4

THE COMPLETE LINEAR SOLUTION AND ALGEBRAIC INSTABILITIES

4.1 Complete Solution Setup

In recent works (Smith and Rosenbluth, 1990 [hereafter SR90]; Nolan and Montgomery, 2000 [hereafter NM00]; Nolan, Montgomery, and Grasso, 2001 [hereafter NMG01]), an instability that grows algebraically, not exponentially, was found to potentially exist in a special class of vortices. They examined a class of basic state vortices that had smooth mean vorticity profiles, finding that some wavenumber-1 perturbations could grow and NMG01 argued that this furnished an explanation for the small-scale trochoidal motion of the center of hurricanes.

This wavenumber-1 algebraic instability (also to be called the trochoidal instability) requires that the mean vortex have its maximum angular velocity ($\bar{\Omega}$) occur at some radius away from the center (called the RMΩ) and have some initial perturbation inside that radius. The asymptotic streamfunction solutions for azimuthal wavenumber-1 of SR90, NM00, and NMG01 can be separated into three important components. First, there is the growing mode which grows as $t^{1/2}$ and whose structure is determined by the initial conditions of the mean vortex, the initial perturbations, the shape of the angular velocity maximum, and the difference between the local angular velocity and the maximum angular velocity. Second, there is the "pseudomode," which interacts with the outer boundary containing the fluid by rotating it at a time-invariant frequency, or in the case of no outer boundary, represents the time-invariant, linear translation of the vortex. The last part of the solution is a collection of sheared Rossby wave disturbances that live near the angular velocity maximum and

decay very slowly, as $t^{-1/2}$ for large t. The interaction between these three portions of the perturbation solution and the mean vortex produces the growth of the first part of the perturbation.

It is an intriguing and natural question, then, to see if the addition of the sheared smooth perturbation in our discontinuous basic-state can excite a similar response. Can we set up our mean vortex and initial perturbations to fit a profile that contains this instability, or does the discontinuous nature of our mean vorticity profile prohibit an analogous instability? Also, are there any other instabilities possible in this model besides the exponential instability discussed in Chapter 3? To answer these questions, we now focus on obtaining the complete solution to our problem. Thus, we will begin with our differential equation for γ_1, i.e. (2.27), and its attendant homogeneous solutions, i.e. (2.28). In this chapter, we will assume that we have some smooth vorticity perturbation within the vortex flow ($\hat{\psi}_s \neq 0$) to guarantee that we will be looking at the full inhomogeneous solution.

To begin, we recall that, in general, the two solutions to (2.28) are $\nu_A = -\frac{1}{2}[(\nu_1+\nu_2)+\nu_D]$, and $\nu_B = -\frac{1}{2}[(\nu_1+\nu_2)-\nu_D]$. These two solutions represent the excited frequencies at which the discrete vortex Rossby waves propagate azimuthally around the center of circulation. Looking more closely at these frequencies, there are two distinct cases: $\nu_D^2 \neq 0$ and $\nu_D^2 = 0$. We now examine each case.

4.2 Case 1: $\nu_D^2 \neq 0$

4.2.1 Analysis

The assumption $\nu_D^2 \neq 0$ implies that there are two independent solutions of the homogeneous equation, corresponding to the two intrinsic waves that may exist on the inner interface:

$$\gamma_{1A}(t) = C_A e^{i\nu_A t}$$

$$\gamma_{1B}(t) = C_B e^{i\nu_B t}.$$

To find the inhomogeneous solution, we use the method of Variation of Parameters (e.g. Zwillinger, 1997, pg. 378). This then furnishes the particular solution for γ_1:

$$\begin{aligned}\gamma_{1P}(t) &= -\gamma_{1A}\left[\int_0^t \frac{\gamma_{1B}\left[\left(\frac{d}{dt'}+i\nu_2\right)i\alpha_1+\mu_1\alpha_2\right]}{W(\gamma_{1A},\gamma_{1B})}dt'\right] \\ &\quad +\gamma_{1B}\left[\int_0^t \frac{\gamma_{1A}\left[\left(\frac{d}{dt'}+i\nu_2\right)i\alpha_1+\mu_1\alpha_2\right]}{W(\gamma_{1A},\gamma_{1B})}dt'\right], \end{aligned} \tag{4.1}$$

where

$$\left[\left(\frac{d}{dt'}+i\nu_2\right)i\alpha_1+\mu_1\alpha_2\right] = \int_0^\infty \mathcal{G}(\rho)\hat{\zeta}_{s0}(\rho)e^{-int'\bar{\Omega}(\rho)}\rho d\rho$$

is derived in Appendix A, $\mathcal{G}(\rho)$ is a composite Green function for the smooth perturbation forcing term, and the Wronskian is given by

$$\begin{aligned} W(\gamma_{1A},\gamma_{1B}) &= C_A e^{i\nu_A t'}\cdot\left[i\nu_B C_B e^{i\nu_B t'}\right] - C_B e^{i\nu_B t'}\cdot\left[i\nu_A C_A e^{i\nu_A t'}\right] \\ &= iC_A C_B \nu_D e^{i(\nu_A+\nu_B)t'}. \end{aligned} \tag{4.2}$$

For notational convenience, we let $F(\rho) = \mathcal{G}(\rho)\hat{\zeta}_{s0}(\rho)\rho$. Therefore,

$$\begin{aligned}\gamma_{1P}(t) &= -C_A e^{i\nu_A t}\left[\int_0^t \frac{C_B e^{i\nu_B t'}}{iC_A C_B\nu_D e^{i(\nu_A+\nu_B)t'}}\left(\int_0^\infty F(\rho)e^{-in\bar{\Omega}t'}d\rho\right)dt'\right] \\ &\quad +C_B e^{i\nu_B t}\left[\int_0^t \frac{C_A e^{i\nu_A t'}}{iC_A C_B\nu_D e^{i(\nu_A+\nu_B)t'}}\left(\int_0^\infty F(\rho)e^{-in\bar{\Omega}t'}d\rho\right)dt'\right] \\ &= \frac{1}{i\nu_D}\Big[-e^{i\nu_A t}\int_0^t e^{-i\nu_A t'}\left(\int_0^\infty F(\rho)e^{-in\bar{\Omega}t'}d\rho\right)dt' \\ &\quad +e^{i\nu_B t}\int_0^t e^{-i\nu_B t'}\left(\int_0^\infty F(\rho)e^{-in\bar{\Omega}t'}d\rho\right)dt'\Big] \\ &= \frac{1}{i\nu_D}\Big[-e^{i\nu_A t}\int_0^\infty F(\rho)\left(\int_0^t e^{-i(n\bar{\Omega}+\nu_A)t'}dt'\right)d\rho \\ &\quad +e^{i\nu_B t}\int_0^\infty F(\rho)\left(\int_0^t e^{-i(n\bar{\Omega}+\nu_B)t'}dt'\right)d\rho\Big] \end{aligned} \tag{4.3}$$

We next define $\mathcal{W}_A(\rho) = n\bar{\Omega}(\rho)+\nu_A$ and $\mathcal{W}_B(\rho) = n\bar{\Omega}(\rho)+\nu_B$; these are the intrinsic rotation rates of the two possible solutions for the inner wave.

Normally, the time integral

$$\int_0^t e^{-i\mathcal{W}_A(\rho)t'}dt'$$

is well-defined. But, in taking the ρ integral in Equation (4.3), the point where the intrinsic rotation rate vanishes (i.e. $\mathcal{W}_A(\rho) = 0$) can be a potential point of discontinuity. It has been verified that for some configurations of the three-region model, $\mathcal{W}_A(\rho)$ or $\mathcal{W}_B(\rho)$ can indeed vanish. However, not all vortex configurations allow for this, e.g. unstable configurations. Let us denote such radii r_A and r_B, respectively.

In fluid dynamics, these points are called critical levels (or critical radii, as would be the case in this cylindrically-based coordinate system). Frequently, these regions in a fluid act as barriers to the propagation of waves, implying an accumulation of wave energy there, provided the wave energy (or wave group velocity) is directed toward the level (e.g. Booker and Bretherton, 1967). However, we will next show that these radii are not critical in the linearized dynamics of our problem.

Let us examine each of these time integrals in the neighborhood of r_A and r_B. Without loss of generality, only the appropriate integral for the A-case will be worked out. The B-case follows similarly. Define

$$\mathcal{I}_A(\rho, t) = \int_0^t e^{-i\mathcal{W}_A(\rho)t'}\, dt'. \tag{4.4}$$

At $\rho = r_A$,

$$\mathcal{I}_A(r_A, t) = \int_0^t e^{-1\cdot 0\cdot t'}\, dt' = \int_0^t 1\, dt' = t. \tag{4.5}$$

Outside of $\rho = r_A$, the integral is well behaved and well defined with no singularities, and thus, can be solved normally. Therefore,

$$\mathcal{I}_A(\rho, t) = \frac{e^{-i\mathcal{W}_A(\rho)t} - 1}{-i\mathcal{W}_A(\rho)}. \tag{4.6}$$

As ρ approaches r_A from either side, $\mathcal{I}_A$ becomes indeterminate. Applying L'Hospital's rule gives

$$\begin{aligned}
\lim_{\rho\to r_A} \mathcal{I}_A(\rho, t) &= \lim_{\rho\to r_A} \frac{\frac{\partial}{\partial\rho}\Big[\exp[-in\bar{\Omega}(\rho)t]\exp[-i\nu_A t] - 1\Big]}{\frac{\partial}{\partial\rho}\Big[-in\bar{\Omega}(\rho) - i\nu_A\Big]} \\
&= \lim_{\rho\to r_A} \frac{\exp[-i\nu_A t]\cdot -in\frac{d\bar{\Omega}}{d\rho}\cdot t\cdot \exp[-in\bar{\Omega}(\rho)t]}{-in\frac{d\bar{\Omega}}{d\rho}} \\
&= \lim_{\rho\to r_A} t\cdot \exp[-i(n\bar{\Omega}(\rho) + \nu_A)t] \\
&= t.
\end{aligned} \tag{4.7}$$

This implies that the form of the integral given by (4.6) is continuous at $\rho = r_A$. Therefore, despite the possibly vanishing denominator, r_A and, by the same argument, r_B will give no problems in the ρ integral in (4.3) if we use (4.6) as our inner-time integral. Henceforth, we will remember that any vanishing $\mathcal{W}_A$ or $\mathcal{W}_B$ in the denominator of (4.6) has already been accounted for.

Having now addressed the potential problems in working with (4.3), we continue examining the particular solution. Equation (4.3) can be written in the form

$$\begin{aligned}
\gamma_{1P}(t) &= \frac{1}{\nu_D}\left(-e^{i\nu_A t}\int_0^\infty \frac{F(\rho)}{\mathcal{W}_A(\rho)}\left[e^{-i\mathcal{W}_A(\rho)t}-1\right]d\rho + e^{i\nu_B t}\int_0^\infty \frac{F(\rho)}{\mathcal{W}_B(\rho)}\left[e^{-i\mathcal{W}_B(\rho)t}-1\right]d\rho\right) \\
&= \int_0^\infty \frac{F(\rho)}{\nu_D}\left(\frac{1}{\mathcal{W}_A(\rho)}\left[e^{i\nu_A t}-e^{-in\bar{\Omega}(\rho)t}\right]+\frac{1}{\mathcal{W}_B(\rho)}\left[e^{-in\bar{\Omega}(\rho)t}-e^{i\nu_B t}\right]\right)d\rho \\
&= \frac{e^{i\nu_A t}}{\nu_D}\int_0^\infty \frac{F(\rho)}{\mathcal{W}_A(\rho)}d\rho - \frac{e^{i\nu_B t}}{\nu_D}\int_0^\infty \frac{F(\rho)}{\mathcal{W}_B(\rho)}d\rho - \int_0^\infty \frac{F(\rho)}{\mathcal{W}_A(\rho)\mathcal{W}_B(\rho)}e^{-in\bar{\Omega}(\rho)t}d\rho. \quad (4.8)
\end{aligned}$$

which admits a simple physical interpretation.

The first and second terms on the right hand side of (4.8) describe the two different Rossby edge waves induced by the forcing from the smooth perturbation on the inner interface. These terms are known functions of time, dependent on the complex number structure of the intrinsic frequencies ν_A and ν_B. The integrals in these two terms are independent of time and describe the projection of the smooth perturbation's initial condition onto the discrete mode. The third term's integral, however, has an integrand that depends on both radius and time. This term describes the direct, time dependent effect the sheared disturbance has on the inner interface.

To determine the temporal behavior of the third integral at long times, we now examine it more closely. First, we look for points where this integral may give us trouble. The most obvious points would be r_A and r_B where $\mathcal{W}_A(\rho)$ and $\mathcal{W}_B(\rho)$ vanish. However, we have already discussed these points above and eliminated their contribution from the total solution. Specifically, for the "problem" point $\rho = r_A$, both the first and third terms in (4.8) are infinite. The sum of the two terms, however, is well-behaved as demonstrated

previously. We will henceforth ignore r_A and r_B in regards to the linear evolution of the amplitude of the inner Rossby wave, i.e. γ_1.

Recalling the third term:

$$-\int_0^\infty \frac{F(\rho)}{\mathcal{W}_A(\rho)\mathcal{W}_B(\rho)} e^{-in\bar{\Omega}(\rho)t} d\rho, \tag{4.9}$$

we note that this integral can be integrated by parts whenever the function

$$\frac{F(\rho)}{\mathcal{W}_A(\rho)\mathcal{W}_B(\rho)\frac{d}{d\rho}\bar{\Omega}(\rho)} \tag{4.10}$$

exists, and whenever the integral

$$\int \frac{1}{int} \cdot \frac{d}{d\rho}\left[\frac{F(\rho)}{\mathcal{W}_A(\rho)\mathcal{W}_B(\rho)\frac{d\bar{\Omega}}{d\rho}}\right] e^{-in\bar{\Omega}(\rho)t} d\rho$$

exists. Therefore, this integral will be a problem wherever $d\bar{\Omega}/d\rho$ vanishes or doesn't exist. Recalling our basic state three-region model, it is easily verified, using (2.6), that

$$\frac{d}{d\rho}\bar{\Omega}(\rho) = -\begin{cases} 0 & 0 < \rho < r_1; \\ \dfrac{\xi_1 r_1^2}{\rho^3} & r_1 < \rho < r_2; \\ \dfrac{\xi_1 r_1^2}{\rho^3} + \dfrac{\xi_2 r_2^2}{\rho^3} & r_2 < \rho < \infty. \end{cases} \tag{4.11}$$

First, note that $d\bar{\Omega}/d\rho$ vanishes inside the inner core ($0 < \rho < r_1$), implying that we cannot integrate (4.9) by parts on the interval $(0, r_1)$. Another important observation to make is that $d\bar{\Omega}/d\rho$ will not exist whenever one of ξ_1, ξ_2, r_1, or r_2 vanishes, but these are degenerate cases and will be ignored. Strictly speaking, we must also remove the points r_1 and r_2 from the integral domain in order to complete the integration by parts of (4.9).

Since (4.10) is smooth and exists at all points except r_1 and r_2, we can integrate (4.9) by parts on the pair of open intervals (r_1, r_2) and (r_2, ∞). Lastly, since $d\bar{\Omega}/d\rho$ vanishes on the interval $[0, r_1)$, we know that $\bar{\Omega}$ is constant. This simplifies this portion of the ρ integral in (4.9).

On the basis of the foregoing discussion, we split the third term into the three pieces mentioned:

$$\begin{aligned} -\int_0^\infty \frac{F(\rho)}{\mathcal{W}_A(\rho)\mathcal{W}_B(\rho)} e^{-in\bar{\Omega}(\rho)t} d\rho &= -\frac{e^{-in\bar{\Omega}(0)t}}{\mathcal{W}_A(0)\mathcal{W}_B(0)} \int_0^{r_1^-} F(\rho) d\rho \\ &\quad - \int_{r_1^+}^{r_2^-} \frac{F(\rho)}{\mathcal{W}_A(\rho)\mathcal{W}_B(\rho)} e^{-in\bar{\Omega}(\rho)t} d\rho \\ &\quad - \int_{r_2^+}^{\infty} \frac{F(\rho)}{\mathcal{W}_A(\rho)\mathcal{W}_B(\rho)} e^{-in\bar{\Omega}(\rho)t} d\rho \end{aligned} \tag{4.12}$$

where r_A^- is the radius infinitesimally smaller than r_A and r_A^+ is the radius infinitesimally larger than r_A.

Now, take any open interval (R_1, R_2) where

$$\frac{F(\rho)}{\mathcal{W}_A(\rho)\mathcal{W}_B(\rho)\frac{d}{d\rho}\bar{\Omega}(\rho)}$$

is smooth and exists. This general notation allows us to look at any possible open interval where we can guarantee smoothness of the above function, for example, (r_1, r_2) or (r_1, r_A) if $r_1 < r_A < r_2$. We can, within the interval (R_1, R_2), integrate by parts the integral:

$$\int_{R_1}^{R_2} \frac{F(\rho)}{\mathcal{W}_A(\rho)\mathcal{W}_B(\rho)} e^{-in\bar{\Omega}(\rho)t} d\rho.$$

and find that it becomes

$$-\frac{1}{int\frac{d\bar{\Omega}}{d\rho}} \left(\frac{F(\rho)}{\mathcal{W}_A(\rho)\mathcal{W}_B(\rho)} \right) e^{-in\bar{\Omega}(\rho)t} \Bigg|_{\rho=R_1}^{R_2} + \int_{R_1}^{R_2} \frac{1}{int} \cdot \frac{d}{d\rho} \left[\frac{F(\rho)}{\mathcal{W}_A(\rho)\mathcal{W}_B(\rho)\frac{d\bar{\Omega}}{d\rho}} \right] e^{-in\bar{\Omega}(\rho)t} d\rho. \tag{4.13}$$

Note that first term in (4.13) has an amplitude part that varies as $1/t$. Upon factoring out a $1/(int)$ from the second integral, we can integrate it by parts again (provided the integrand is sufficiently smooth) to pull out further amplitude dependencies that vary as positive integral powers of $1/t$. The end result is that, as $t \to \infty$, (4.13) will decay as the most slowly decaying part: $(1/t)$. In this way, we write this term as $\mathcal{O}(1/t)$ which indicates the asymptotic solution has a leading portion that is on the order of $(1/t)$.

Thus, as $t \to \infty$, (4.8) reduces to

$$\gamma_{1P}(t) \;\to\; \frac{e^{i\nu_A t}}{\nu_D}\int_0^\infty \frac{F(\rho)}{\mathcal{W}_A(\rho)}d\rho - \frac{e^{i\nu_B t}}{\nu_D}\int_0^\infty \frac{F(\rho)}{\mathcal{W}_B(\rho)}d\rho - \frac{e^{-in\bar{\Omega}(0)t}}{\mathcal{W}_A(0)\mathcal{W}_B(0)}\int_0^{r_1^-} F(\rho)d\rho + \mathcal{O}(1/t). \tag{4.14}$$

This leads to the long-time asymptotic solution for γ_1, including the homogeneous solution:

$$\gamma_1(t) \;\to\; \overbrace{e^{i\nu_A t}\left(C_A + \frac{1}{\nu_D}\int_0^\infty \frac{F(\rho)}{\mathcal{W}_A(\rho)}d\rho\right)}^{\text{Term 1}} + \overbrace{e^{i\nu_B t}\left(C_B - \frac{1}{\nu_D}\int_0^\infty \frac{F(\rho)}{\mathcal{W}_B(\rho)}d\rho\right)}^{\text{Term 2}} \underbrace{- \frac{e^{-in\bar{\Omega}(0)t}}{\mathcal{W}_A(0)\mathcal{W}_B(0)}\int_0^{r_1^-} F(\rho)d\rho}_{\text{Term 3}} + \underbrace{\mathcal{O}(1/t)}_{\text{Term 4}}. \tag{4.15}$$

From here, the asymptotic solution for γ_2 can be diagnosed from (2.26):

$$\gamma_2(t) = \frac{1}{\mu_1}\left[i\frac{d\gamma_1(t)}{dt} - \nu_1\gamma_1(t) + \alpha_1(t)\right].$$

The form of $\gamma_2(t)$ at long times is similar to that of $\gamma_1(t)$ as given by (4.15).

4.2.2 Discussion and Interpretation

Equation (4.15) embodies the important physics in the case of two distinct Rossby wave frequencies ν_A and ν_B. Outside the transient forcing of the sheared disturbances, the only pieces that remain are three distinct Rossby wave modes that will only grow or decay if $\nu_D^2 < 0$, i.e. ν_A and ν_B are not purely real. In the asymptotic solution (4.15), we see the original discrete vortex Rossby waves in first two terms on the right-hand side, oscillating at their intrinsic rates ν_A and ν_B as well as a mode (Term 3) that oscillates at the rotation rate of the inner core, which is in solid body rotation.

Let us take a closer look at the asymptotic solution (4.15). Terms 1 and 2 are similar. Both include the initial discrete wave solution which oscillates at its particular frequency (the C_A and C_B pieces) and also the portions that the sheared disturbance excites at each wave frequency (the integral piece). Term 3 represents the additional component excited

if there is any smooth perturbation initially in the core. The collection of terms (denoted Term 4) describe the transient forcing by the sheared disturbance's streamfunction on the discrete waves. These four terms are the leading linear dynamics that influence the inner wave (γ_1). Similar calculations (not shown) yield an analogous asymptotic solution for the outer wave (γ_2).

In the exponentially unstable case ($\nu_D^2 < 0$), we see that Terms 1 and 2 in (4.15) are either exponentially growing or decaying in time, since, in this case, ν_A and ν_B are just complex conjugates of each other. Term 3 is purely oscillatory and represents the constant forcing by the unsheared smooth perturbation in the inner core. Therefore, the asymptotic analysis would point to the exponentially growing mode as the dominant piece in the temporal evolution of the inner wave. The addition of the sheared disturbances does not fundamentally change the exponential instability properties of the discrete modes.

Looking more closely at the solution (4.15), we now inquire whether we can find a similar behavior in this solution to the algebraic instability in SR90, NM00, and NMG01, discussed at the beginning of this chapter. Recalling the asymptotic algebraically-growing perturbation streamfunction solutions for azimuthal wavenumber-1 of SR90, NM00, and NMG01, we note that the solution itself can be separated into three important parts. First, there is the growing mode which grows as $t^{1/2}$ and whose structure is determined by the initial conditions of the mean vortex, the initial perturbations, the shape of the angular velocity maximum, and the difference between the local angular velocity and the maximum angular velocity. Second, there is the "pseudomode," which interacts with the outer boundary containing the fluid by rotating it at a time-invariant frequency, or in the case of no outer boundary, represents the time-invariant, linear translation of the vortex. The last, and most interesting, part of the solution is a collection of sheared Rossby wave disturbances that live near the angular velocity maximum and decay very slowly, as $t^{-1/2}$ for large t. The reason for this slow decay is that the amount of differential shearing near this angular velocity maximum is minimized, since $d\bar{\Omega}(r = \mathrm{RM}\Omega)/dr$ vanishes at the RMΩ and is small in its vicinity, where RMΩ is the radius of the angular velocity maximum.

It was determined in NM00 that only through these decaying waves' interactions with the mean state can the growing mode can amplify. Without these slowly decaying sheared waves, NM00 noted that the growing part of the solution could not grow and would, instead, remain constant in amplitude.

These sheared waves in our three-region model would decay too quickly, however, to support this amplification. This is where the theory of Brunet and Warn (1990) and Brown and Stewartson (1980) can be applied. In those works, the authors show that the stream-function of sheared disturbances in non-vanishing radial shear decays at $(1/t^2)$, not $(1/t^{1/2})$ as required for the trochoidal instability of SR90, NM00, and NMG01.

To gain an understanding of the physical differences between our model and the model used in SR90, NM00, and NMG01, assume that $\xi_1 < 0$ and $\xi_2 > 0$. This would imply that the RMΩ is at r_2. Recalling (4.11), we note that there is a discontinuity in the radial derivative of the angular velocity at r_2. This fact implies that any sheared waves that would be excited near r_2 would be sheared too quickly, as illustrated in Brunet and Warn (1990), to sufficiently aid in the growth of the discrete waves, excluding this algebraic growth mechanism for the class of three-region profiles considered here.

Physically, it is the "cuspy" nature of the angular velocity profile that precludes the instability of SR90 and NM00 from occurring here. Without a region of zero radial shearing around the RMΩ, a collection of decaying sheared disturbances are sheared apart too quickly. This implies, in particular, that the trochoidal instability will not be present. However, a neutral (non-growing) trochoidal oscillation is still present.

The natural extension of the above discussion implies that the trochoidal instability of SR90, NM00, and NMG01 will not exist for any similar discrete basic state profile of a finite number of constant vorticity annuli since the radial basic-state angular velocity profile in those cases will again be too "cuspy" to allow for the crucial slowly-sheared waves of the SR90 and NM00 solutions. Discrete basic state vorticity profiles will always have discontinuities in their radial angular velocity derivatives at the interface radii. These radii are also the only places where the RMΩ can exist, meaning that we could not construct a discrete

vorticity profile that could have a RMΩ at some point where the radial angular velocity derivative could be continuous and vanish. (This can be readily shown upon extending (2.6) to any finite number of constant vorticity regions.) Therefore, for an n-region discrete vorticity model of the type considered here, the conditions needed for the trochoidal instability discussed in SR90 and NM00 can never be satisfied.

4.3 Case 2: $\nu_D^2 = 0$ (Coalescence of Roots)

4.3.1 Analysis

Let us now assume that $\nu_D^2 = 0$. The solutions to the homogeneous characteristic equation (2.28) are then repeated roots: $\nu = -\frac{1}{2}(\nu_1 + \nu_2)$.

Since we have a repeated root to our characteristic equation, ordinary differential equation techniques tell us that the two independent solutions to the homogeneous equation (2.27) are

$$\gamma_{1A}(t) = C_A e^{i\nu t},$$

$$\gamma_{1B}(t) = C_B t e^{i\nu t}. \tag{4.16}$$

This can indeed be verified directly by substituting these solutions into the homogeneous form of (2.27).

To find the inhomogeneous solutions, we again use the method of Variation of Parameters. Using the notation from the previous section, the particular solution is then

$$\begin{aligned} \gamma_{1P}(t) &= -\gamma_{1A}\left[\int_0^t \frac{\gamma_{1B}\int_0^\infty F(\rho)e^{-int'\bar{\Omega}(\rho)}}{W(\gamma_{1A},\gamma_{1B})}dt'\right] \\ &\quad \gamma_{1B}\left[\int_0^t \frac{\gamma_{1A}\int_0^\infty F(\rho)e^{-int'\bar{\Omega}(\rho)}}{W(\gamma_{1A},\gamma_{1B})}dt'\right] \end{aligned} \tag{4.17}$$

where

$$\begin{aligned} W(\gamma_{1A},\gamma_{1B}) &= C_A e^{i\nu t'}\cdot\left[C_B e^{i\nu t'} + C_B i\nu t' e^{i\nu t'}\right] - C_B t e^{i\nu t'}\cdot\left[i\nu C_A e^{i\nu t'}\right] \\ &= C_A C_B e^{2i\nu t'}\cdot[1 + i\nu t' - i\nu t'] \\ &= C_A C_B e^{2i\nu t'}. \end{aligned} \tag{4.18}$$

Using (4.18), we find that

$$\begin{aligned}
\gamma_{1P}(t) &= -C_A e^{i\nu t}\int_0^t \frac{C_B t' e^{i\nu t'}}{C_A C_B e^{2i\nu t'}}\int_0^\infty F(\rho)e^{-int'\bar{\Omega}(\rho)}d\rho dt' \\
&\quad + C_B e^{i\nu t}\int_0^t \frac{C_A e^{i\nu t'}}{C_A C_B e^{2i\nu t'}}\int_0^\infty F(\rho)e^{-int'\bar{\Omega}(\rho)}d\rho dt' \\
&= -e^{i\nu t}\int_0^t t' e^{-i\nu t'}\int_0^\infty F(\rho)e^{-int'\bar{\Omega}(\rho)}d\rho dt' \\
&\quad + te^{i\nu t}\int_0^t e^{-i\nu t'}\int_0^\infty F(\rho)e^{-int'\bar{\Omega}(\rho)}d\rho dt'
\end{aligned}$$

Defining $\mathcal{W}(\rho) = \nu + n\bar{\Omega}(\rho)$ (similar to Case 1) and reversing the order of the integrations, we obtain

$$\begin{aligned}
\gamma_{1P}(t) &= -e^{i\nu t}\int_0^\infty F(\rho)\int_0^t t' e^{-i\mathcal{W}(\rho)t'}dt' d\rho \\
&\quad + te^{i\nu t}\int_0^\infty F(\rho)\int_0^t e^{-i\mathcal{W}(\rho)t'}dt' d\rho \\
&= -e^{i\nu t}\int_0^\infty F(\rho)\left[\frac{(i\mathcal{W}(\rho)t+1)e^{-i\mathcal{W}(\rho)t}-1}{(\mathcal{W}(\rho))^2}\right]d\rho \\
&\quad + te^{i\nu t}\int_0^\infty F(\rho)\left[\frac{e^{-i\mathcal{W}(\rho)t}-1}{\mathcal{W}(\rho)}\right]d\rho
\end{aligned} \tag{4.19}$$

Adding the integrals in (4.19) together and canceling terms, yields the following particular solution:

$$\gamma_{1P}(t) = \int_0^\infty \frac{F(\rho)}{\mathcal{W}(\rho)^2}\left[-e^{-in\bar{\Omega}(\rho)t} + e^{i\nu t} - it\mathcal{W}(\rho)e^{i\nu t}\right]d\rho. \tag{4.20}$$

The full solution, including the homogeneous solution, is then given by

$$\gamma_1(t) = C_A e^{i\nu t} + tC_B e^{i\nu t} + \int_0^\infty \frac{F(\rho)}{\mathcal{W}(\rho)^2}\left[-e^{-in\bar{\Omega}(\rho)t} + e^{i\nu t} - it\mathcal{W}(\rho)e^{i\nu t}\right]d\rho. \tag{4.21}$$

4.3.2 Discussion and Interpretation

Technically, (4.21) describes an algebraic instability. The perturbation streamfunction will grow as t as $t \to \infty$, as is evident in the last term in (4.21) as well as the last piece in the first term. The only limitation on this growth is the initial assumption that ν_D vanishes, which physically, corresponds to the mean vortex configuration lying on the border separating exponential stability and instability.

This particular point brings us back to (3.2), which is ν_D^2 for wavenumber-1. As was mentioned, if $\nu_D = 0$, (which is equivalent to saying that $\epsilon = \delta^2$) then wavenumber-1 will have this algebraic instability. This set of possible vortices, then, can be unstable, at least in an algebraic sense. These type of solutions also exist for any wavenumber-n; they are the edges of the instability regions in Figures 3.1 and 3.3.

It is the relatively small and precise nature of the conditions for this instability that makes it more of a curiosity than anything physically relevant. Just by changing the mean vortex minisculely, one can readily move from this algebraic instability to a full exponential instability or complete stability.

Notice also that our solution (4.21) shares none of the same structure of the SR90 and NM00 solutions. In fact, this solution is analogous to the coalescence of roots solution given in Farrell's solution to the Eady baroclinic instability problem (Farrell, 1984). Physically, this solution is the transition solution between exponential stability and instability. The waves are not able to affect each other enough to be able to phase-lock, but are able to interact with the mean vortex in such a way to allow themselves to still grow.

Chapter 5

EDDY FLUXES AND MEAN VORTEX CHANGES

5.1 Complete Quasi-Linear Mean Flow Solution

In the preceding chapters, we have studied the effects the mean flow has on determining the stability properties of vortex Rossby waves. It is, therefore, only natural to examine the role the waves have on changing the mean flow. This is important since mean flow changes relate to issues like vortex strengthening or weakening, even in cases of exponential stability ($\nu_D^2 > 0$).

Having analytically obtained the streamfunction and vorticity as functions of time, we can, as a first approximation, solve for the wave fluxes analytically to determine the wave-induced changes to the mean vortex. This approach, called quasi-linear dynamics, uses the linearized dynamical solutions for perturbation evolution as a diagnosis for the potential mean flow change those perturbations may have.

Recall that in the linearized, inviscid, two-dimensional Euler equations, the equation for the time-rate of change of the mean tangential flow is given by

$$\frac{\partial \bar{v}(r,t)}{\partial t} = -\overline{u'\zeta'}. \tag{5.1}$$

This is readily derived by taking the azimuthal mean of the azimuthal momentum equation (see (2.1)), taking into account the mean and perturbation contributions of the flow. Since ψ' and ζ' have been solved for analytically, we can thus determine $\partial\bar{v}/\partial t$.

To simplify the analysis, we consider a monochromatic disturbance and fix n as before. In our quasi-linear approximation, we assume that the total mean flow acceleration is the sum of the accelerations diagnosed for each wavenumber. Thus, for any perturbation of

wavenumber-n, the Fourier decompositions (as in (2.10)) of any perturbation streamfunction and vorticity are

$$\psi' = \mathrm{Re}\left[\hat{\psi}(r,t)e^{in\lambda}\right],$$

$$\zeta' = \mathrm{Re}\left[\hat{\zeta}(r,t)e^{in\lambda}\right].$$

Next, split the complex Fourier amplitudes $\hat{\psi}$ and $\hat{\zeta}$ into their component real and imaginary parts:

$$\hat{\psi} = \hat{\psi}_r + i\hat{\psi}_i,$$

$$\hat{\zeta} = \hat{\zeta}_r + i\hat{\zeta}_i.$$

Therefore,

$$\begin{aligned} u' &= -\frac{1}{r}\frac{\partial}{\partial\lambda}\left\{\mathrm{Re}\left[\hat{\psi}e^{in\lambda}\right]\right\} \\ &= -\frac{1}{r}\frac{\partial}{\partial\lambda}\left[\hat{\psi}_r\cos(n\lambda) - \hat{\psi}_i\sin(n\lambda)\right] \\ &= \frac{n}{r}\left[\hat{\psi}_r\sin(n\lambda) + \hat{\psi}_i\cos(n\lambda)\right]; \end{aligned} \tag{5.2}$$

and similarly

$$\zeta' = \hat{\zeta}_r\cos(n\lambda) - \hat{\zeta}_i\sin(n\lambda). \tag{5.3}$$

Thus,

$$u'\zeta' = \frac{n}{r}\left[\hat{\psi}_r\hat{\zeta}_r\sin(n\lambda)\cos(n\lambda) - \hat{\psi}_r\hat{\zeta}_i\sin^2(n\lambda) + \hat{\psi}_i\hat{\zeta}_r\cos^2(n\lambda) - \hat{\psi}_i\hat{\zeta}_i\cos(n\lambda)\sin(n\lambda)\right]$$

which gives, upon azimuthally averaging and recalling the orthogonality of the sine and cosine functions,

$$\overline{u'\zeta'} = \frac{n}{2r}\left[\hat{\psi}_i\hat{\zeta}_r - \hat{\psi}_r\hat{\zeta}_i\right]. \tag{5.4}$$

Equation (5.4) is the basis from which we continue working since it is the general solution for a given vorticity perturbation and streamfunction. Working with our three-region model, recall from Chapter 2, that the Fourier components of the streamfunction

and vorticity in terms of the basis functions $\hat{\Psi}_1$ and $\hat{\Psi}_2$ and Dirac delta functions (denoted by δ^*):

$$\begin{aligned}
\hat{\psi}(r,t) &= \overbrace{\gamma_1(t)\hat{\Psi}_1(r) + \gamma_2(t)\hat{\Psi}_2(r)}^{\hat{\psi}_d} + \hat{\psi}_s, \\
\hat{\zeta}(r,t) &= \underbrace{\gamma_1(t)\delta^*(r-r_1) + \gamma_2(t)\delta^*(r-r_2)}_{\hat{\zeta}_d} + \hat{\zeta}_s,
\end{aligned} \tag{5.5}$$

where $\hat{\psi}_d$ and $\hat{\zeta}_d$ are defined as the discrete Rossby wave perturbation streamfunction and vorticity Fourier components, respectively. $\hat{\psi}_s$ and $\hat{\zeta}_s$ are the smooth perturbation streamfunction and vorticity, respectively. As above, we separate the real and imaginary components of each of these Fourier components:

$$\begin{aligned}
\hat{\psi}_d &= \hat{\psi}_{dr} + i\hat{\psi}_{di} = \left(\gamma_{1r}\hat{\Psi}_1 + \gamma_{2r}\hat{\Psi}_2\right) + i\left(\gamma_{1i}\hat{\Psi}_1 + \gamma_{2i}\hat{\Psi}_2\right), \\
\hat{\psi}_s &= \hat{\psi}_{sr} + i\hat{\psi}_{si}, \\
\hat{\zeta}_d &= \hat{\zeta}_{dr} + i\hat{\zeta}_{di} = \left(\gamma_{1r}\delta^*(r-r_1) + \gamma_{2r}\delta^*(r-r_2)\right) + i\left(\gamma_{1i}\delta^*(r-r_1) + \gamma_{2i}\delta^*(r-r_2)\right), \\
\hat{\zeta}_s &= \hat{\zeta}_{sr} + i\hat{\zeta}_{si}.
\end{aligned} \tag{5.6}$$

where $\gamma_1 = \gamma_{1r} + i\gamma_{1i}$ and $\gamma_2 = \gamma_{2r} + i\gamma_{2i}$.

We now examine the time-rate of change of the mean tangential wind as the sum of four different eddy terms, using the general expression given in (5.4):

$$\begin{aligned}
\frac{\partial \bar{v}}{\partial t} = -\overline{u'\zeta'} &= -\overline{u'_d\zeta'_d} - \overline{u'_d\zeta'_s} - \overline{u'_s\zeta'_d} - \overline{u'_s\zeta'_s} \\
&= -\frac{n}{2r}\Big[\left(\hat{\psi}_{di}\hat{\zeta}_{dr} - \hat{\psi}_{dr}\hat{\zeta}_{di}\right) + \left(\hat{\psi}_{di}\hat{\zeta}_{sr} - \hat{\psi}_{dr}\hat{\zeta}_{si}\right) \\
&\quad + \left(\hat{\psi}_{si}\hat{\zeta}_{dr} - \hat{\psi}_{sr}\hat{\zeta}_{di}\right) + \left(\hat{\psi}_{si}\hat{\zeta}_{sr} - \hat{\psi}_{sr}\hat{\zeta}_{si}\right)\Big],
\end{aligned} \tag{5.7}$$

5.2 Mean Flow Change By the Discrete Vortex Rossby Waves

5.2.1 Analytical Theory

We now focus on the $\overline{u'_d\zeta'_d}$ term, i.e. the eddy flux due entirely to the Rossby edge (or discrete-mode) waves. Examining the purely discrete-mode tangential wind change, we see

that

$$\begin{aligned}
-\overline{u'_d\zeta'_d} &= -\frac{n}{2r}\left(\hat{\psi}_{di}\hat{\zeta}_{dr} - \hat{\psi}_{dr}\hat{\zeta}_{di}\right) \\
&= -\frac{n}{2r}\Big[\left(\gamma_{1i}\hat{\Psi}_1 + \gamma_{2i}\hat{\Psi}_2\right)\left(\gamma_{1r}\delta^*(r-r_1) + \gamma_{2r}\delta^*(r-r_2)\right) \\
&\quad - \left(\gamma_{1r}\hat{\Psi}_1 + \gamma_{2r}\hat{\Psi}_2\right)\left(\gamma_{1i}\delta^*(r-r_1) + \gamma_{2i}\delta^*(r-r_2)\right)\Big] \\
&= -\frac{n}{2r}\left(\hat{\Psi}_2\delta^*(r-r_1) - \hat{\Psi}_1\delta^*(r-r_2)\right)\left[\gamma_{1r}\gamma_{2i} - \gamma_{1i}\gamma_{2r}\right], \qquad (5.8)
\end{aligned}$$

where (5.6) has been used.

The right-hand side of this acceleration equation has two main pieces. The last (in square braces), $[\gamma_{1r}\gamma_{2i} - \gamma_{1i}\gamma_{2r}]$, encapsulates the temporal evolution of the acceleration by the discrete waves, while the first, $(\hat{\Psi}_2\delta^*(r-r_1) - \hat{\Psi}_1\delta^*(r-r_2))$, gives the radial structure of the azimuthal acceleration induced by the discrete Rossby waves. Since γ_1 and γ_2 are already intimately related by (2.26), the temporal piece can be further simplified using:

$$\gamma_2(t) = \frac{1}{\mu_1}\left[i\frac{d\gamma_1(t)}{dt} - \nu_1\gamma_1(t) + \alpha_1(t)\right]. \qquad (5.9)$$

Splitting γ_1, γ_2, and α_1 into their component real and imaginary components as above (r subscripts for real part, i subscripts for imaginary part), it is found that

$$\begin{aligned}
\gamma_{2r} + i\gamma_{2i} &= \frac{1}{\mu_1}\left[i\frac{d}{dt}\left(\gamma_{1r} + i\gamma_{1i}\right) - \nu_1\left(\gamma_{1r} + i\gamma_{1i}\right) + \left(\alpha_{1r} + i\alpha_{1i}\right)\right] \\
&= \frac{1}{\mu_1}\left(-\frac{d\gamma_{1i}}{dt} - \nu_1\gamma_{1r} + \alpha_{1r}\right) + \frac{i}{\mu_1}\left(\frac{d\gamma_{1r}}{dt} - \nu_1\gamma_{1i} + \alpha_{1i}\right). \qquad (5.10)
\end{aligned}$$

This implies

$$\begin{aligned}
\gamma_{2r} &= \frac{1}{\mu_1}\left(-\frac{d\gamma_{1i}}{dt} - \nu_1\gamma_{1r} + \alpha_{1r}\right), \\
\gamma_{2i} &= \frac{1}{\mu_1}\left(\frac{d\gamma_{1r}}{dt} - \nu_1\gamma_{1i} + \alpha_{1i}\right). \qquad (5.11)
\end{aligned}$$

Thus, we can regard γ_2 as known once γ_1 has been determined. Thus, we can further simplify (5.8) by eliminating γ_2 using (5.11). Looking only at the temporal term that includes the real and imaginary components of the γ functions, we see that

$$\begin{aligned}
\gamma_{1r}\gamma_{2i} - \gamma_{1i}\gamma_{2r} &= \frac{1}{\mu_1}\left(\gamma_{1r}\frac{d\gamma_{1r}}{dt} - \nu_1\gamma_{1r}\gamma_{1i} + \alpha_{1i}\gamma_{1r} + \gamma_{1i}\frac{d\gamma_{1i}}{dt} + \nu_1\gamma_{1i}\gamma_{1r} - \alpha_{1r}\gamma_{1i}\right) \\
&= \frac{1}{\mu_1}\left(\frac{1}{2}\frac{d|\gamma_1|^2}{dt} - \left[\alpha_{1r}(t)\gamma_{1i} - \alpha_{1i}(t)\gamma_{1r}\right]\right).
\end{aligned}$$

This then implies that

$$-\overline{u_d'\zeta_d'} = -\frac{n}{2r\mu_1}\left(\hat{\Psi}_2\delta^*(r-r_1) - \hat{\Psi}_1\delta^*(r-r_2)\right)\left[\frac{1}{2}\frac{d|\gamma_1|^2}{dt} - (\alpha_{1r}\gamma_{1i} - \alpha_{1i}\gamma_{1r})\right].$$

This can be further simplified by evaluating the radially-dependent coefficients ($\hat{\Psi}_1$ and $\hat{\Psi}_2$) at the Dirac function's only non-zero points, as well as using the definitions of μ_1 and δ, to get:

$$-\overline{u_d'\zeta_d'} = -\frac{2}{\xi_1}\left(\delta^*(r-r_1) - \delta^2\delta^*(r-r_2)\right)\left[\frac{1}{2}\frac{d|\gamma_1|^2}{dt} - (\alpha_{1r}\gamma_{1i} - \alpha_{1i}\gamma_{1r})\right]. \tag{5.12}$$

Equation (5.12) embodies an interesting feature of the discrete waves' eddy vorticity flux. Strictly neutral discrete waves (i.e. exponentially stable normal modes from Michalke and Timme, 1967, and S99) by themselves do not contribute to mean flow changes. In that particular case, $\psi_s' = 0$ which implies that $\alpha_1 = 0$. This then implies that $|\gamma_1|^2$ is constant, which means that the bracketed term in (5.12) vanishes.

This particular mean flow acceleration solution for the discrete Rossby waves is an example of a non-acceleration theorem (e.g. Lindzen, 1990). The quasi-linear dynamics have shown that, without an exponential instability and sheared disturbances, neutral (steady) waves will not accelerate the mean flow. This result is readily generalizable to basic states with any finite number of constant vorticity regions and their corresponding discrete vortex Rossby waves, assuming that no exponential instabilities exist.

In the presence of sheared disturbances, however, the bracketed term in (5.12) may not vanish exactly. This additional forcing of the discrete mode can, thus, lead to a spin-up or spin-down of the vortex at the interfaces (because of the selective nature of the Dirac delta function). Physically, the idea of a Dirac delta function in velocity change may seem a little strange. But, as will be shown in later sections, when we smooth out the discrete jump slightly, the delta function becomes spread out as a small but peaked function. Thus, we will regard the sign of $\partial\bar{v}/\partial t$ from (5.12) as the physically meaningful quantity.

An interesting feature to note from (5.12) is that the delta functions have opposite magnitude. In fact, the magnitude of the velocity change at r_2 is δ^2 of the velocity change

at r_1. This can be explained by appealing to angular momentum conservation. The discrete waves and their associated mean flow represent a complete solution to the two-dimensional Euler equations. Therefore, any velocity changes they create will have to obey conservation of angular momentum, since that quantity has been shown previously to be integrally conserved in the Euler equations. This conservation law explains why the accelerations at the two interfaces are of opposite sign and have a spacial factor (δ^2) to correct for the radial dependence of angular momentum.

5.2.2 Illustrative Example

As an illustration in the case of discrete vortex Rossby waves, for unstable cases, depending on the sign of ξ_1, the discrete waves extract energy from one interface's mean flow and deposit it at the other interface. One can see that this exchange of angular momentum (and, subsequently, vorticity) is evident in previous studies. As an example, let us examine Figure 5.1 from S99. This figure summarizes the changes in the mean vortex in a simple two-dimensional nonlinear model run with a smoothed-out three-region vortex. In their case, ξ_1 would be negative. This would imply that for these growing discrete waves alone, the inner interface should spin-up, while the outer interface should spin-down. For early times (less than 8 hours) while the dynamics are more linear than nonlinear, we can use the quasi-linear dynamical results to interpret the mean vortex changes. We see that the quasi-linear theory does give the proper signature velocity changes. The magnitudes of this velocity change are significant, on the order of 10 m/s in a 55 m/s mean vortex. This underscores the potential role that these discrete modes may play in the mean flow dynamics of intense, geophysical vortices.

In the previous paragraphs, we have only examined exponential instability cases. Quantitatively, though, how can a smooth perturbation affect the mean vortex in an exponentially stable case? Although we have completed the linear analysis for the general problem in the three-region model, these answers by themselves do not give easily calculated results for mean flow changes caused by the eddy vorticity fluxes. Therefore, to aid in our examination of the wave-mean flow interactions in sharp gradient vortices with sheared disturbances,

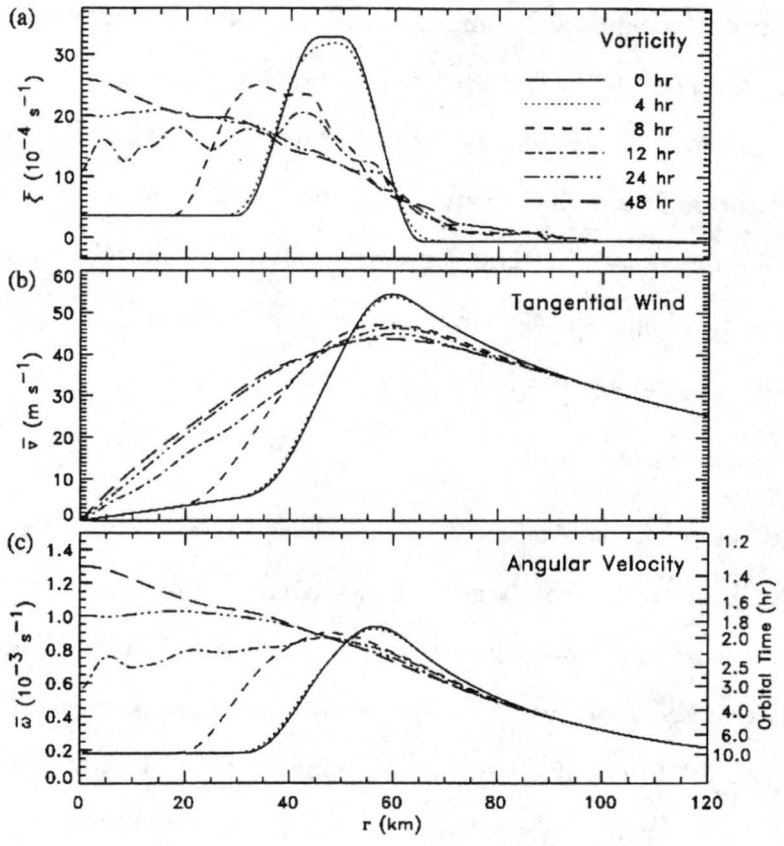

Figure 5.1: Time evolution of the mean fields in a nonlinear numerical model run of a smoothed, discrete-like, mean vorticity vortex. (From Schubert et al. (1999))

we employ a simple numerical model. To aid in the analysis of the results, we reduce the complexity of our problem by using a two-region constant vorticity initial basic state. This mean vortex is frequently referred to as a Rankine vortex and is inspired by observations similar to the tornado and polar stratospheric vortex plots in the introduction of this work, Figures 1.1 and 1.3, respectively.

We also reduce the complexity of our examination by focusing on perturbations that will be sheared apart, i.e. outside the radius of the Rankine vortex's non-zero vorticity. The full examination of the sheared disturbances' effects in the three-region model is an interesting study to be deferred to later work.

5.3 Semispectral Two-Dimensional Fluid Flow Model

The numerical model that we will employ is discussed more fully in Montgomery, Hidalgo, and Reasor (2000). It is a two-dimensional nondivergent flow model written in polar coordinates, employing a Fourier azimuthal representation and a finite-difference radial representation. Since one of the coordinates is spectral, while the other is standardly discretized, we call this model "semispectral".

Recalling that the flow is non-divergent, the only prognostic variable that is needed to be calculated is the total streamfunction ψ. Our prognostic equation is conservation of total vorticity, given by (2.3), which is given in terms of total streamfunction by

$$\left(\frac{\partial}{\partial t} + u\frac{\partial}{\partial r} + \frac{v}{r}\frac{\partial}{\partial \lambda}\right)\nabla^2\psi = 0. \tag{5.13}$$

We split the total streamfunction into azimuthal mean components and wavenumber perturbations, as done previously. Using this separation, we can run the model in a variety of modes, including linear with constant mean flow, linear with updating mean flow, and full nonlinear.

In the first model runs used in this work, the radial grid spacing is set to 250 meters in a circular domain of 300 kilometer radius. Azimuthal modes up to wavenumber-5 are resolved; however, in linear dynamics, only the wavenumbers of the initial perturbation are needed. Diffusion is set to 0, since we are examining inviscid dynamics. The time step used is 20 seconds, with model output every 5 minutes. Later model runs at higher resolutions will be described in more detail later.

For the discrete interfaces, a cubic Hermite polynomial is used to connect the constant vorticity regions (e.g. S99; Kossin, Schubert, and Montgomery, 2000). This Hermite spline occurs over seven grid points (e.g. Figure 5.2). Second-order accurate calculations are made in the discretized radial direction.

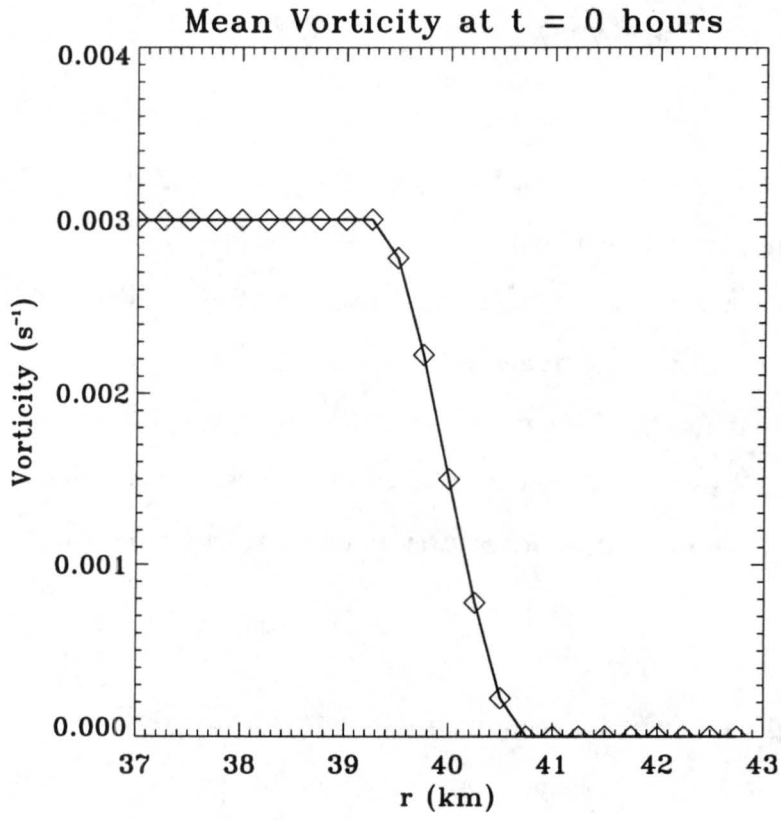

Figure 5.2: An example of the cubic Hermite spline function.

5.4 The Effect of the Discrete Mode

5.4.1 Rankine Vortex and Physical Discussion

We begin by looking at the simplest interaction between the discrete modes excited on the interface and a small, smooth vorticity perturbation, i.e. a sheared disturbance outside a Rankine vortex. In the following simulations, the Rankine vortex is 40 km in radius with a constant vorticity value of 3×10^{-3} s^{-1} (see Figure 5.3). We start with no perturbation on the interface, but a smooth wavenumber-2 perturbation centered at either 60, 70, or 80 km (r_0). The perturbation has an amplitude (ζ_M) of 1×10^{-4} s^{-1} and a radial structure in the form of a half-period of a cos^2 function with a wavelength of 20 km:

$$\hat{\zeta}_s = \begin{cases} \zeta_M \cos^2\left(\frac{\pi(\rho - r_0)}{20 \text{ km}}\right) & r_0 - 10 \text{ km} \leq \rho \leq r_0 + 10 \text{ km} , \\ 0 & \text{elsewhere.} \end{cases} \tag{5.14}$$

The integration is run out to 60 hours.

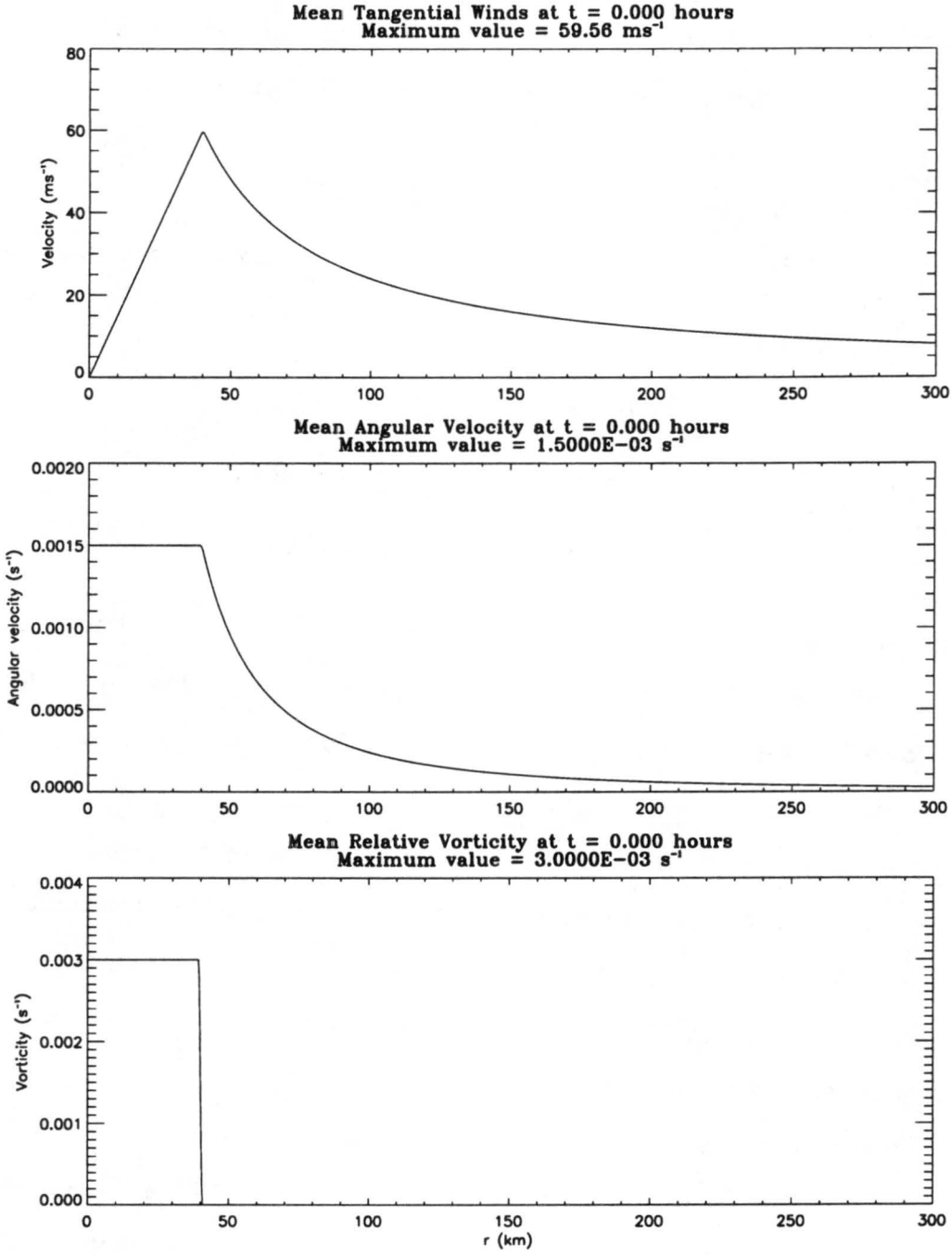

Figure 5.3: The Rankine vortex mean profiles for tangential velocity ($\bar{v}(r)$), angular velocity ($\bar{\Omega}(r)$), and vorticity ($\bar{\zeta}(r)$).

The model is also run with strictly linear dynamics. The results of the 80 kilometer perturbation simulation are shown below in Figures 5.4 and 5.5. Figure 5.4 shows the perturbation (relative) vorticity (ζ') for the first five hours of the simulation, while Figure 5.5 shows the attendant eddy momentum flux ($\overline{u'v'}$) at those same times.

As mentioned above in (5.1), $d\bar{v}/dt = -\overline{u'\zeta'}$. It can be easily shown that in two-dimensional non-divergent dynamics, $\overline{u'\zeta'} = \partial(r^2\overline{u'v'})/(r^2\partial r)$.

We define $\delta\bar{v}(T)$ as the integral change in the mean tangential wind over the time interval $[0, T]$:

$$\begin{aligned}
\delta\bar{v}(T) &= \int_0^T \frac{d\bar{v}}{dt} dt \\
&= -\int_0^T \frac{1}{r^2}\frac{\partial}{\partial r}\left(r^2\overline{u'v'}\right) dt \\
&= -\frac{1}{r^2}\frac{\partial}{\partial r}\left(r^2 \int_0^T \overline{u'v'} dt\right). \qquad (5.15)
\end{aligned}$$

From this, we can integrate the linear perturbation solutions over the 60 hour run of the semispectral model to diagnose the total quasi-linear spin-up/spin-down due to the divergence/convergence of the eddy momentum flux. The results of this are summarized in Figure 5.6.

On Figure 5.6, the solid line is the $\delta\bar{v}$ as computed by the linearized semispectral model during these 60 hours. The dashed line is the mean-flow change if the sheared disturbance acted by itself via the Orr mechanism mentioned in Chapter 2, i.e. using $\overline{u'_s v'_s}$ for $\overline{u'v'}$ (cf. Farrell (1987) and MK97, pg. 450-454, for a description of sheared disturbances' effects on the mean flow in smooth mean profiles).

The first thing to notice is the magnitude which $\delta\bar{v}$ is modified with the inclusion of the discrete mode. By itself, the smooth perturbation would cause a spin-up/spin-down couplet with a magnitude of 0.15 m/s. But when we include the effects of these pseudo-discrete waves in the model, the spin-up increases to approximately 0.75 m/s in the vicinity of the initial sheared disturbance with a spin-down of 0.65 m/s. Also apparent in the full calculation is a spike of spin-down at the steep vorticity interface, on the order of 0.3 m/s

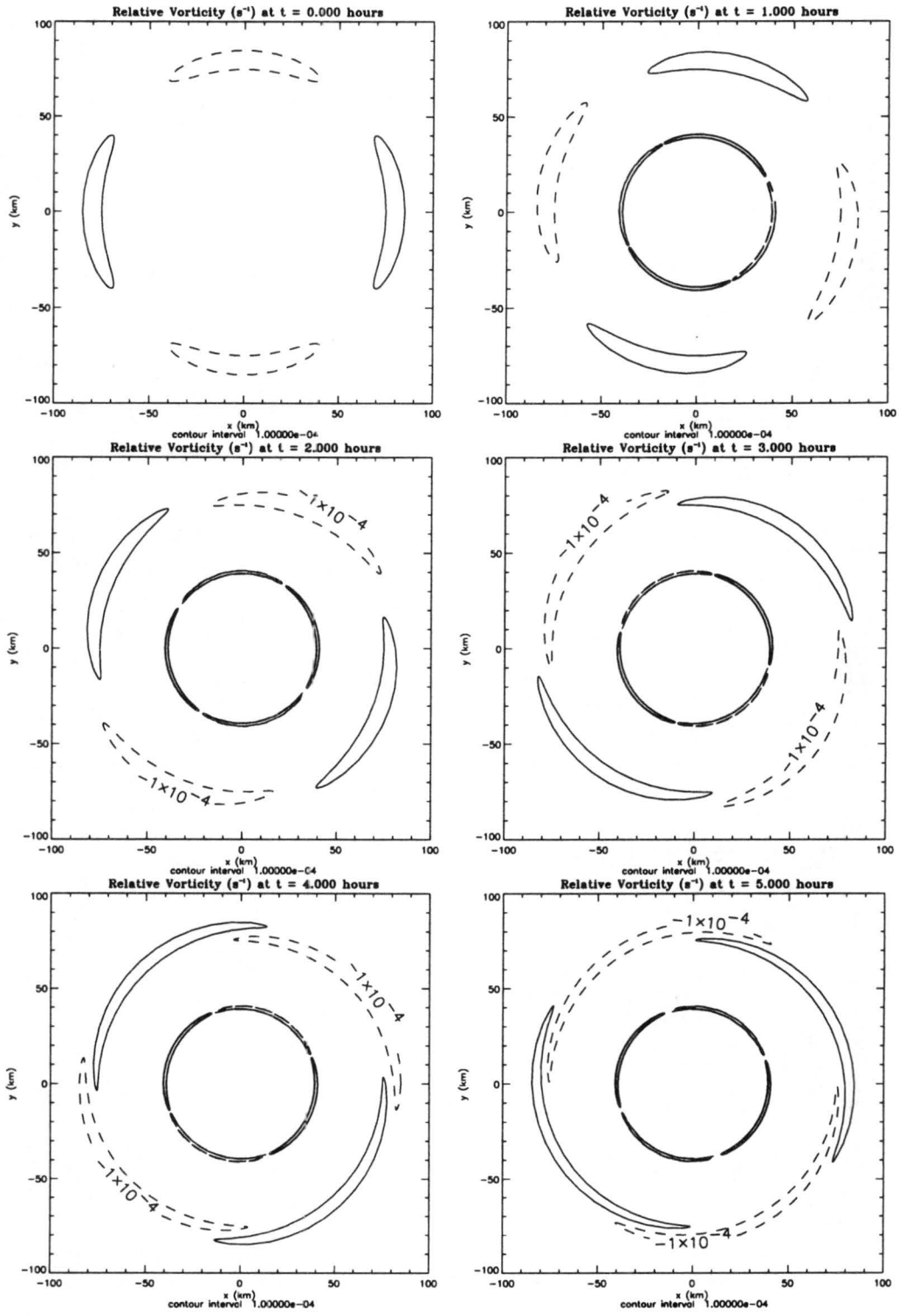

Figure 5.4: Perturbation (relative) vorticity (ζ') for the 80 kilometer perturbation case at each hour for the first five simulation hours showing the spiraling of the initial smooth perturbation.

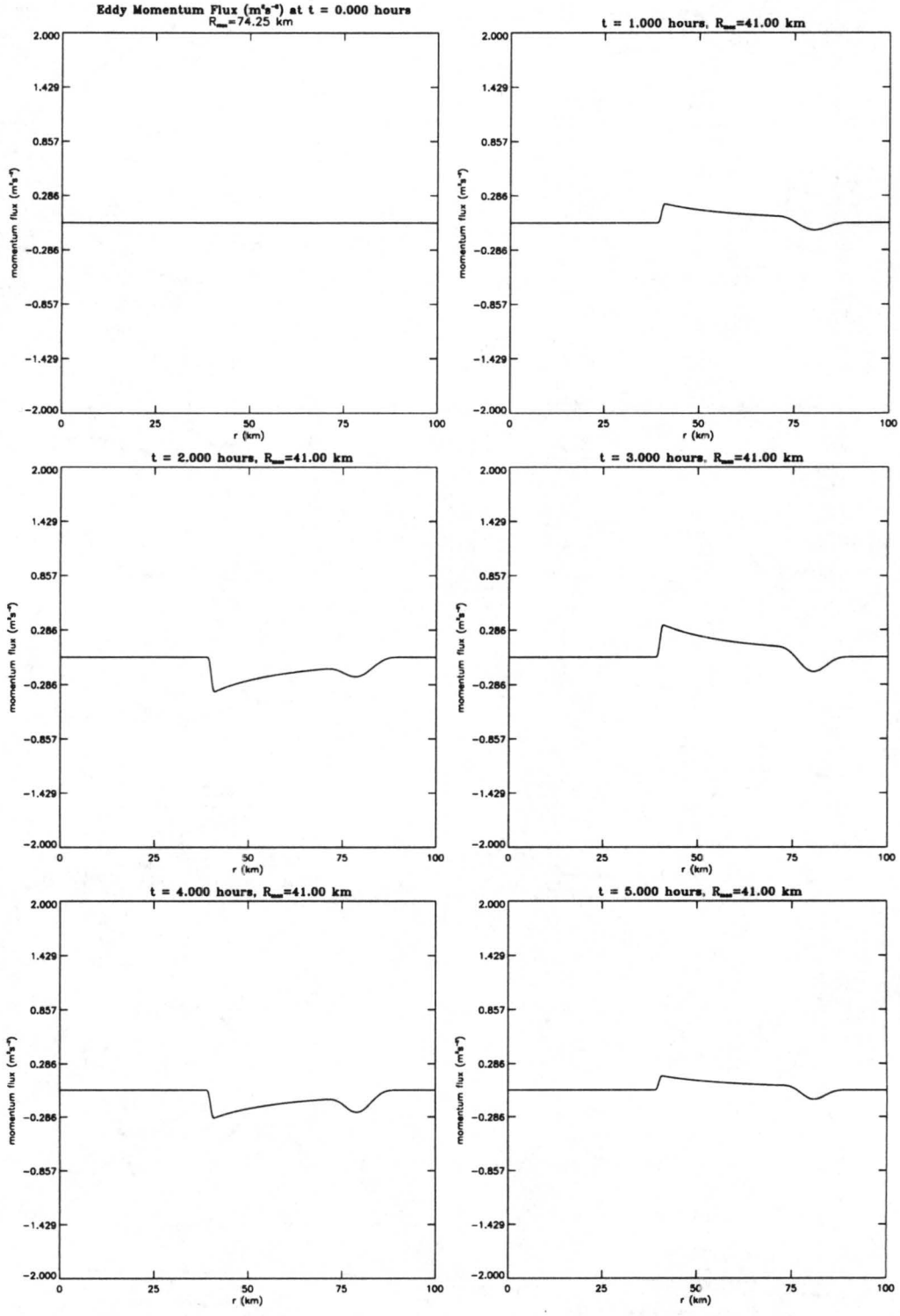

Figure 5.5: The tangential momentum flux ($\overline{u'v'}$) at each hour for the first five hours for the 70 kilometer perturbation case.

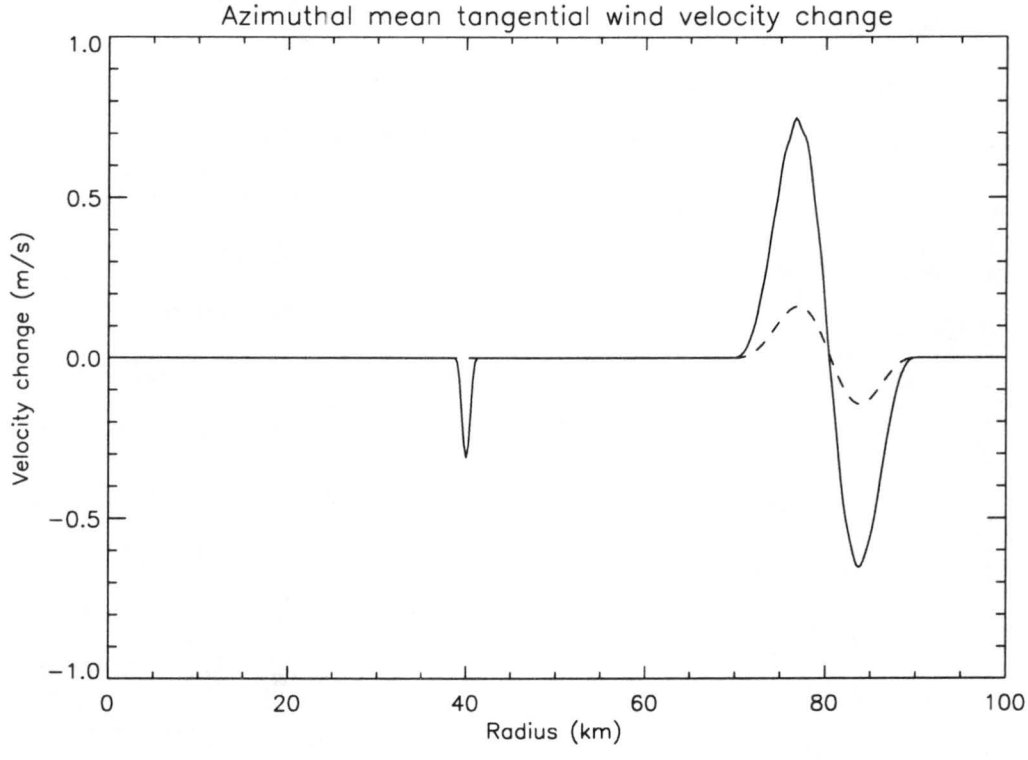

Figure 5.6: Diagnosed quasi-linear $\delta\bar{v}$ for the 80 kilometer perturbation case as calculated by the integrated momentum flux in the semispectral model. The solid line is the total result. The dashed line is the tangential wind change solely due to the sheared disturbance , i.e. $\partial(r^2\overline{u_s'v_s'})/(r^2\partial r)$.

over the 60 hour integration. This is the manifestation of the Dirac delta function that our analytical calculation pointed to. Here, the delta function gets spread out over the radial extent of the interface.

While these numbers may be small compared to the values in the mean flow, recall that the initial disturbance vorticity was 1/30 of the Rankine's vorticity. At small amplitudes, a larger initial perturbation will have mean flow accelerations varying on a quadratic scale, i.e. doubling the strength of the perturbation leads to a quadrupling of the mean flow change (cf. (5.7) and MK97). Quantification of large amplitude disturbances' mean flow changes is beyond the scope of this work, but will be considered in future work.

Focusing on the spin-down at the interface, it is only natural to ask why the discrete modes excited by this sheared disturbance would tend to spin-down the vortex in the vicinity of this interface. The answer comes from total momentum conservation.

As a purely circular flow, the vortex has a certain mean flow angular momentum associated with it. As the sheared disturbance jostles the interface with a radial perturbation wind, the discrete Rossby wave is excited. The angular momentum needed to produce this perturbation cannot be spontaneously created in violation of conservation of total angular momentum, so where does it come from? Since the perturbations are only allowed to interact with the mean flow, the only source of mean angular momentum available for these waves is the mean flow. So, to create the angular momentum needed for these discrete waves, the mean flow must decelerate. In this way, these waves are sometimes called "negative energy waves," (e.g. Briggs, Daugherty, and Levy, 1970) since they strengthen by cannibalizing the mean flow's angular momentum (and, thus, kinetic energy).

One can make an argument that this effect is already encapsulated in the wave-mean flow dynamics of the three-region model, that is, in (5.12). Assuming that the outer interface disappears in a limiting sense ($\xi_2 \to 0$ and $\delta \to 1$), we can use Equation (5.12) as a starting point for the acceleration of the mean azimuthal velocity at the inner interface:

$$\frac{\partial \bar{v}}{\partial t}(r = r_1) = -\frac{2}{\xi_1}\delta^*(r - r_1)\left[\frac{1}{2}\frac{d|\gamma_1|^2}{dt} - (\alpha_{1r}\gamma_{1i} - \alpha_{1i}\gamma_{1r})\right].$$

In the Rankine case, ξ_1 is positive. At the beginning of our simulation, γ_1 is set to zero, but because of the smooth perturbation's radial winds, it will have to increase in magnitude. Thus, $d|\gamma_1|^2/dt > 0$. Therefore, the coefficient on the Dirac delta function at r_1 will be negative, which implies a spin-down at that initial moment. Then, as the smooth perturbation is sheared apart and the discrete wave returns to neutrality, the amplitude becomes constant and α_1 (the forcing on the inner interface by the smooth perturbation) decays to zero, implying that the mean flow change at the inner interface also decays to zero. This does not guarantee, however, that the total integrated change would be negative. Since the strength of the sheared disturbance's winds decrease with time, though, the tendency at very short times should be large compared to later tendencies, and thus, should dominate.

Based on the above results and discussion, it seems fairly obvious that the discrete wave can significantly influence the mean flow accelerations in sharp gradient vortices with sheared disturbances around them. But, to what extent are the wave-induced acceleration changes affected by the spatial position of the smooth perturbation?

5.4.2 Resonance Between the Discrete Mode and the Basic State

Figure 5.7 displays the $\delta\bar{v}$ calculation for the two other cases where this particular model was run, but moving the initial smooth vorticity perturbation to a 60 and 70 kilometer radius, respectively. The $\delta\bar{v}$ calculation for the 70 kilometer case is similar to the 80 kilometer case examined above, but the model produces an interesting and sharp tripole in the 60 kilometer case.

The magnitude of the mean tangential flow change due to the Orr mechanism alone, i.e. $\partial(r^2\overline{u_s'v_s'})/(r^2\partial r)$, in this case is similar to the 70 and 80 kilometer cases, i.e. around 0.1 m/s, but *the mean flow change due to the inclusion of the discrete mode is almost two orders of magnitude greater.* Also, the deceleration in the vicinity of the interface has increased by at least an order of magnitude. What caused this significant change?

First, let us recall Kelvin's theory on the rotation rate of an unforced wavenumber-n discrete perturbation on a Rankine vortex (Lamb, 1932). This states that the azimuthal

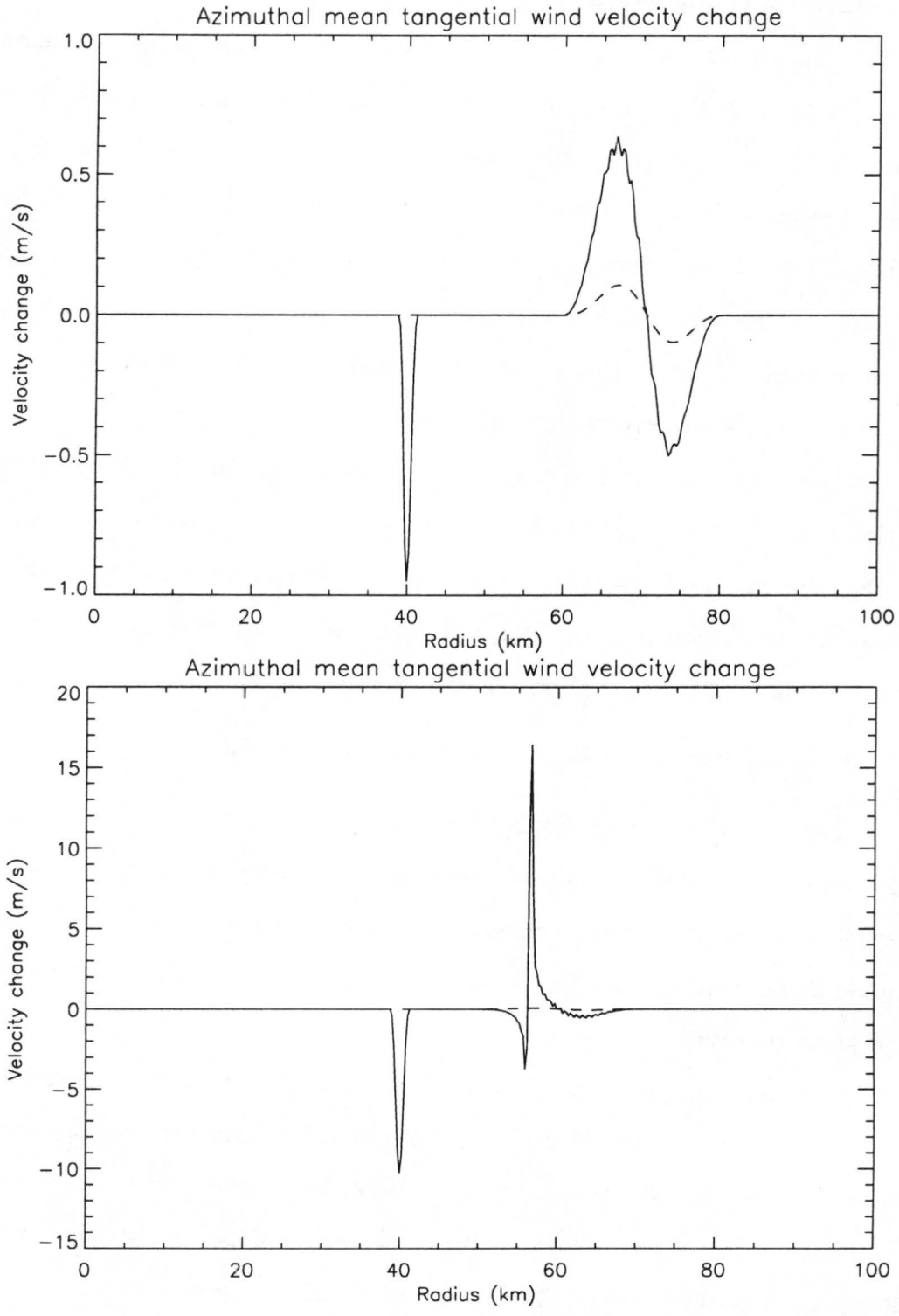

Figure 5.7: Same as Figure 5.6, but with the smooth perturbation centered at 70 km (top) and 60 km (bottom).

rotation rate of the discrete wave is governed by the vorticity of the vortex (ζ_0) and the azimuthal wavenumber n:

$$\omega_{wave} = \frac{\zeta_0}{2}(n-1). \tag{5.16}$$

So, assuming Kelvin's theory gives a guideline for the rotation rate of our discrete mode in the semispectral simulation, we find that our wavenumber-2 wave should rotate at a rate of 1.5×10^{-4} s^{-1}.

Next, the angular velocity profile outside of the interface radius in a Rankine vortex is given by

$$\bar{\Omega}(r) = \frac{\zeta_0}{2}\left(\frac{r_0}{r}\right)^2.$$

Therefore, in our Rankine vortex, the angular velocity profile which governs the shearing of the smooth perturbation is

$$\bar{\Omega}(r) = \frac{1}{2}\left(3.0 \times 10^{-4}\ \text{s}^{-1}\right)\left(\frac{40\ \text{km}}{r}\right)^2.$$

This gives values ranging from 4.9×10^{-5} s^{-1} at 70 km to 9.6×10^{-5} s^{-1} at 50 km. Recall that the actual rotation rate of a wavenumber-n perturbation embedded in this mean flow is n times the mean rotation rate, i.e. (2.14). Using this, we get that the rotation rate of the smooth perturbation would be 9.8×10^{-5} s^{-1} at 70 km to 1.92×10^{-4} s^{-1} at 50 km.

In fact, we can show that the radius where the Kelvin's frequency and the frequency of a wave advected by the basic state of a Rankine vortex with vorticity ζ_0 and radius r_0 are the same occurs at

$$r_C = r_0\sqrt{\frac{n}{(n-1)}} = \frac{r_0}{\sqrt{1-\frac{1}{n}}}. \tag{5.17}$$

This radius is called a "critical radius". It is equivalent to r_A and r_B in our discussion of the initial value problem's complete solution for the three-region model. More specifically, though, in our Rankine vortex case, this radius is at $r_C = 56.57$ km.

We must be careful using this result, however, since Kelvin's result does not include any additional forcings on the vortex's interface which can affect the frequency of rotation

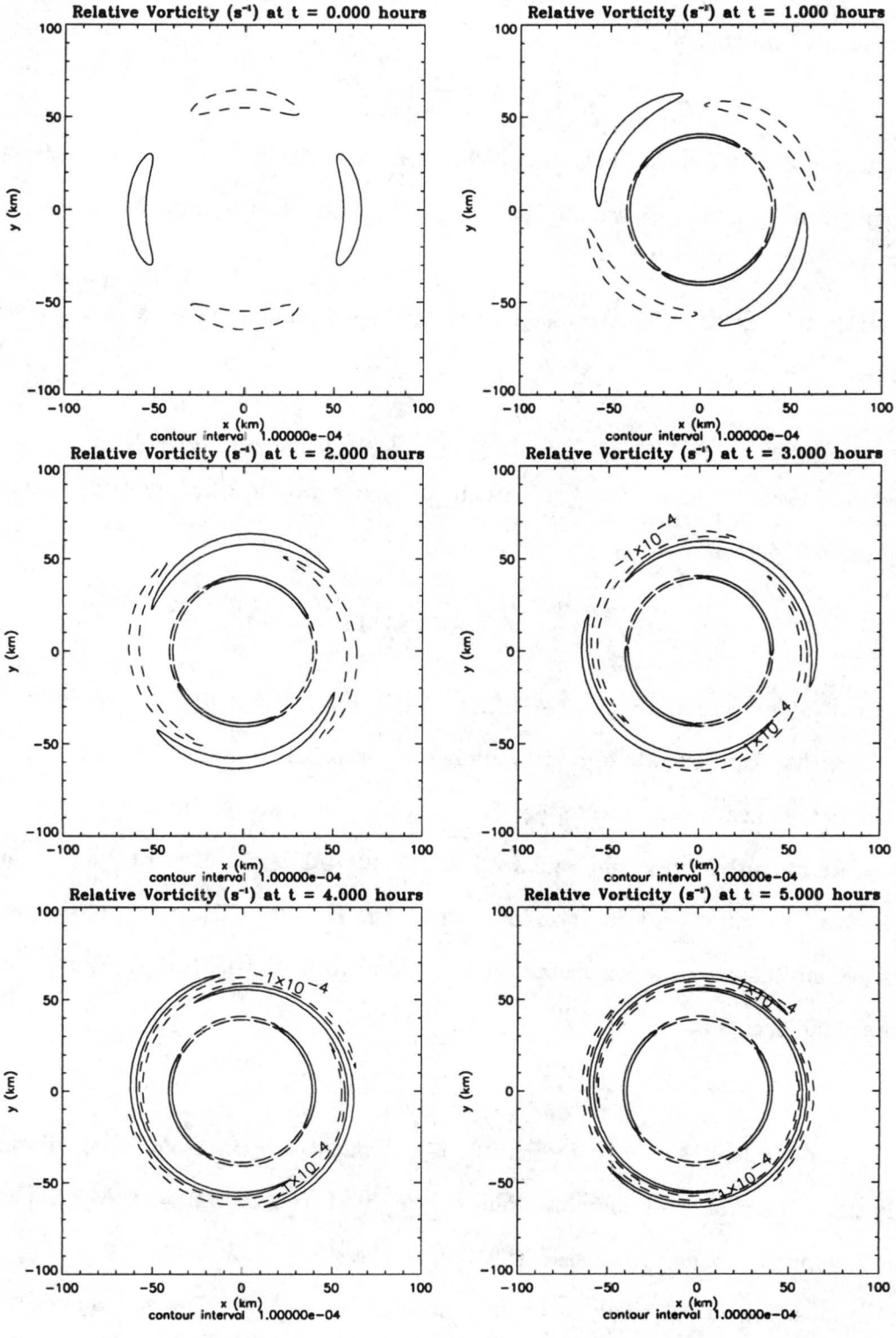

Figure 5.8: Same as Figure 5.4, but with the smooth perturbation centered at 60 km.

of the perturbation. However, if the forcings rotate at the same rate as the perturbation, the discrete mode will rotate at its intrinsic frequency and will be reinforced continuously.

In the 60 km case, the initial smooth perturbation excites the discrete mode at the beginning of the simulation. Until the smooth perturbation is sheared apart more sufficiently, u'_s at the interface tends to rotate at the same rate as the main body of the sheared disturbance, i.e., close to the rotation rate of a wavenumber-2 perturbation being advected by the mean flow at 60 km. We've already shown that the rotation rates of the excited, unforced wave and the rotation rate of the initial smooth perturbation at 60 km are nearly identical. For further visual evidence of this, one can examine the phases of the waves with respect to each other in Figure 5.8.

It is this near-"resonance" between the main body of the sheared disturbance's forcing and the discrete wave that helps produce the impressive radial structure in the $\delta\bar{v}$ calculation. This can be seen in the difference between the evolution of the momentum fluxes in Figures 5.5 and 5.9.

Notice the persistent "bump" in the momentum flux near 55 km in Figure 5.9, especially after two hours. It is this feature that differentiates Figures 5.5 and 5.9 and helps explain the differences in the $\delta\bar{v}$ calculations for the two cases. The resonance between the sheared disturbance being advected around and the intrinsic frequency of the discrete perturbation on the Rankine vortex's edge sets up that persistent momentum flux divergence/convergence couplet that shows up as a concave-down "bump" in Figure 5.9. Since this behavior persists for a significant amount of time, this leads to tremendous tangential velocity changes.

This mechanism could be important in geophysical vortices that are quasi-two-dimensional and have steep vorticity gradients, e.g. hurricanes or the polar stratospheric vortex. The change in the mean flow caused by these linearized perturbation reactions could prove to be comparable with nonlinear dynamics. We now investigate the nonlinear dynamics to complete this comparison.

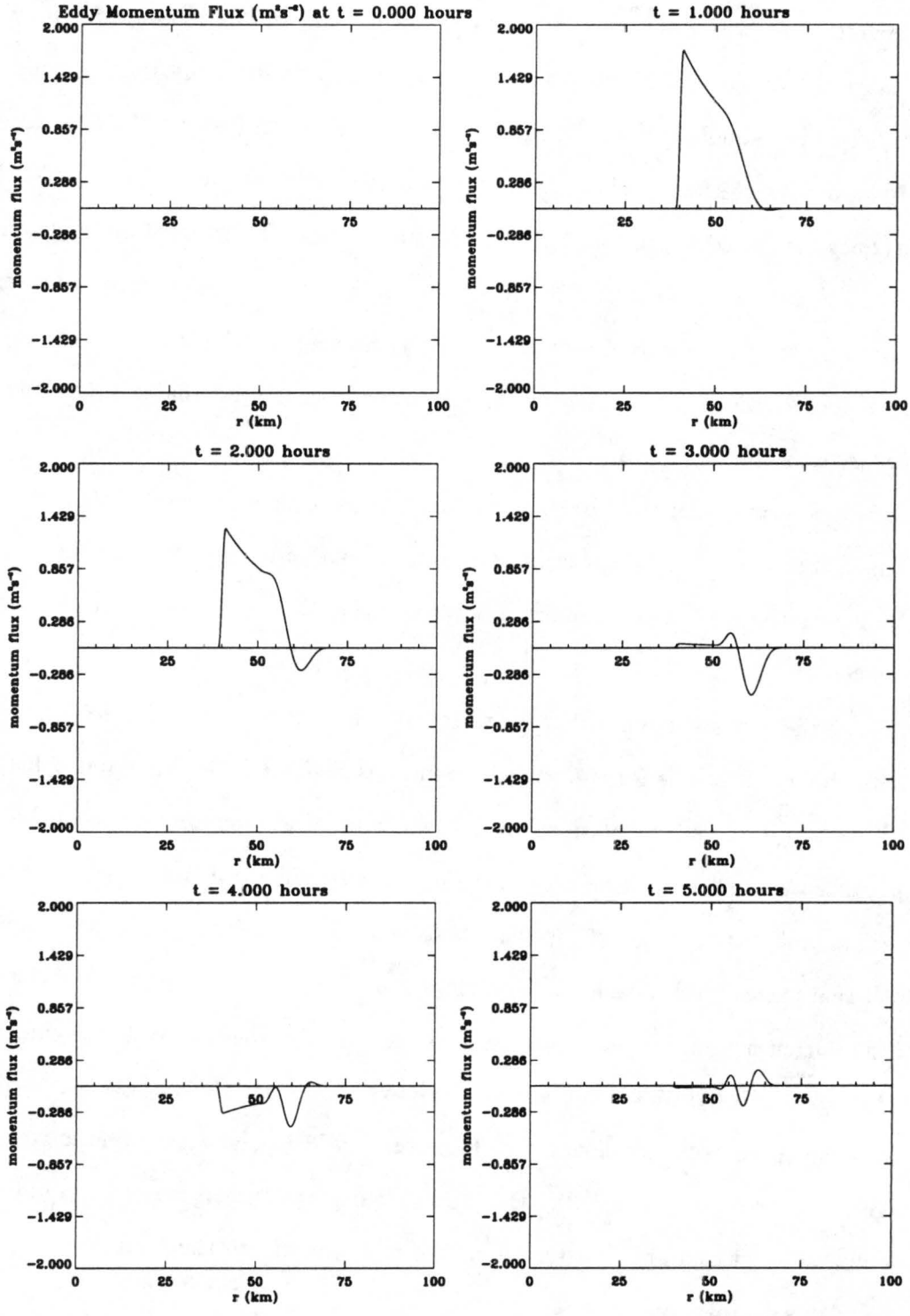

Figure 5.9: Same as Figure 5.5, but with the smooth perturbation centered at 60 km.

5.5 Fully Nonlinear Dynamics

5.5.1 Comparisons with Linear Theory

Whenever significant events and changes happen in linearized dynamics, the natural question is to ask how much of those effects will persist in the more complete nonlinear dynamics. Since these large magnitude effects often require perturbations to either be persistent, large amplitude, or have large gradients, one should check that the assumptions of linear theory, i.e. $\vec{u}' \cdot \nabla\zeta' \ll$ linear terms, are not violated. We will show that such a violation has indeed occurred in our 60 km case.

It is natural to see whether or not the nonlinear results agree with the linear results. To do this, we use the same model setup, except we double the number of computed azimuthal modes to 10 and turn on the nonlinear calculation code in the model. The doubling of the azimuthal modes provides us with improved azimuthal resolution needed to make the nonlinear results more accurate.

We start by looking at the 70 and 80 km perturbation cases (Figure 5.10). We notice, in these two cases, that the agreement between the nonlinear and linear runs becomes much better as the smooth perturbation moves farther and farther away from the critical radius.

In the 80 km case, the nonlinear and linear dynamics agree quite well. The spin-up/spin-down couplet outside the interface spreads out slightly and is not as extreme, but the deceleration near the sharp vorticity interface is well captured. The spin-down near the interface in the 70 km case is significantly amplified in the nonlinear dynamics, while the spin-up/spin-down couplet outside the interface spreads out as more sheared waves are allowed to be excited and radially propagate (mostly due to radial perturbation flow).

This highlights the usefulness of the quasi-linear theory in predicting velocity changes, at least in cases where perturbations are not near a critical radius. The nonlinear dynamics do tend to reduce the overall effect of the spin-up/spin-down, probably since the sheared disturbances will now be sheared not only by the mean flow, but also by themselves and their excited discrete perturbations. The change to nonlinear dynamics mean that the

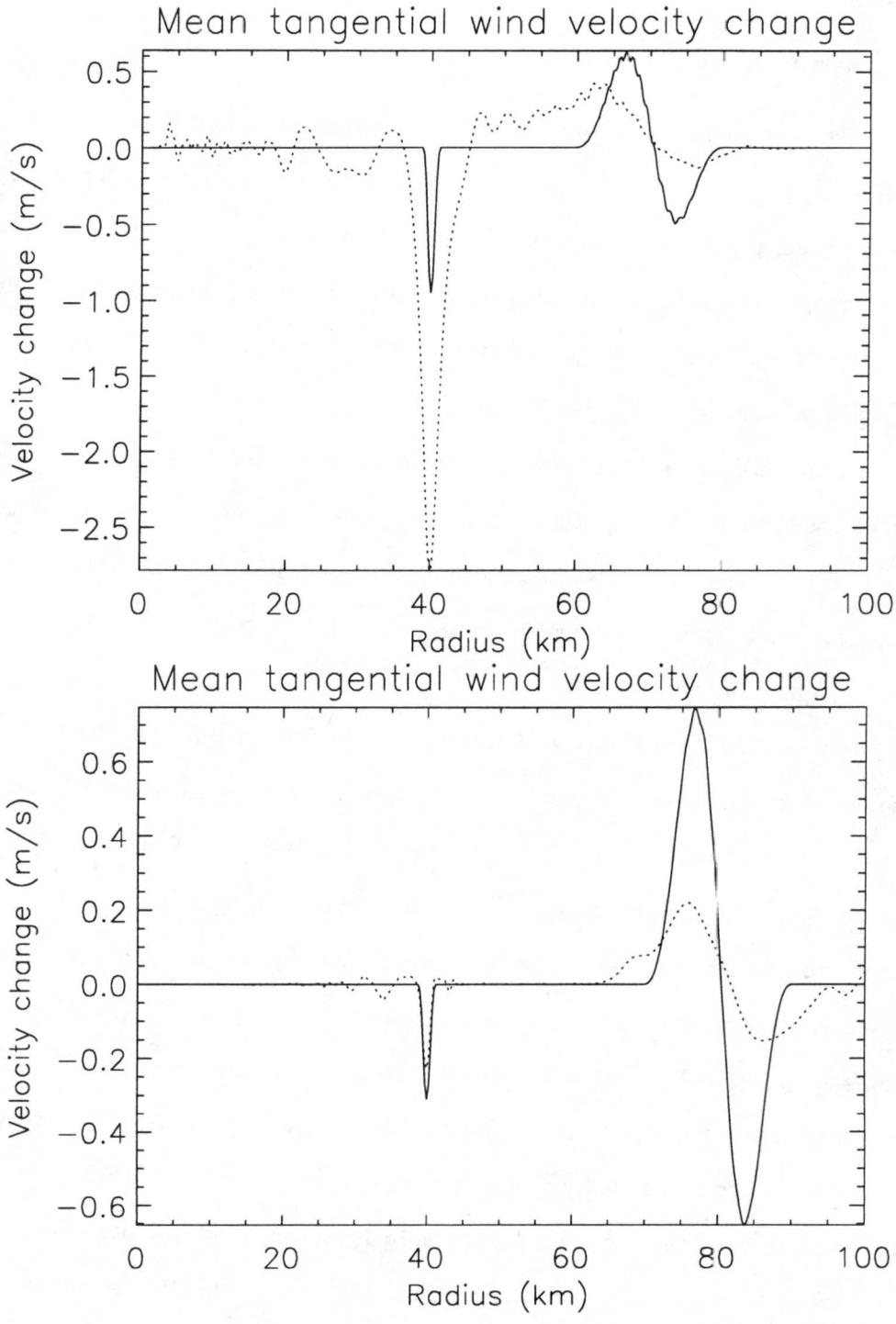

Figure 5.10: $\delta\bar{v}$ comparison between the linear (solid line) and non-linear (dotted line) model runs of the semispectral model in the 70 kilometer (top) and 80 kilometer (bottom) perturbation cases. All integrations are done over the full 60 hour life cycle.

perturbations' fluxes will now move out to different radii, since they can now be moved radially, which means that the maximum spin-up/spin-down magnitudes will be reduced in exchange for allowing velocity changes at radii beyond the initial sheared disturbance's radii.

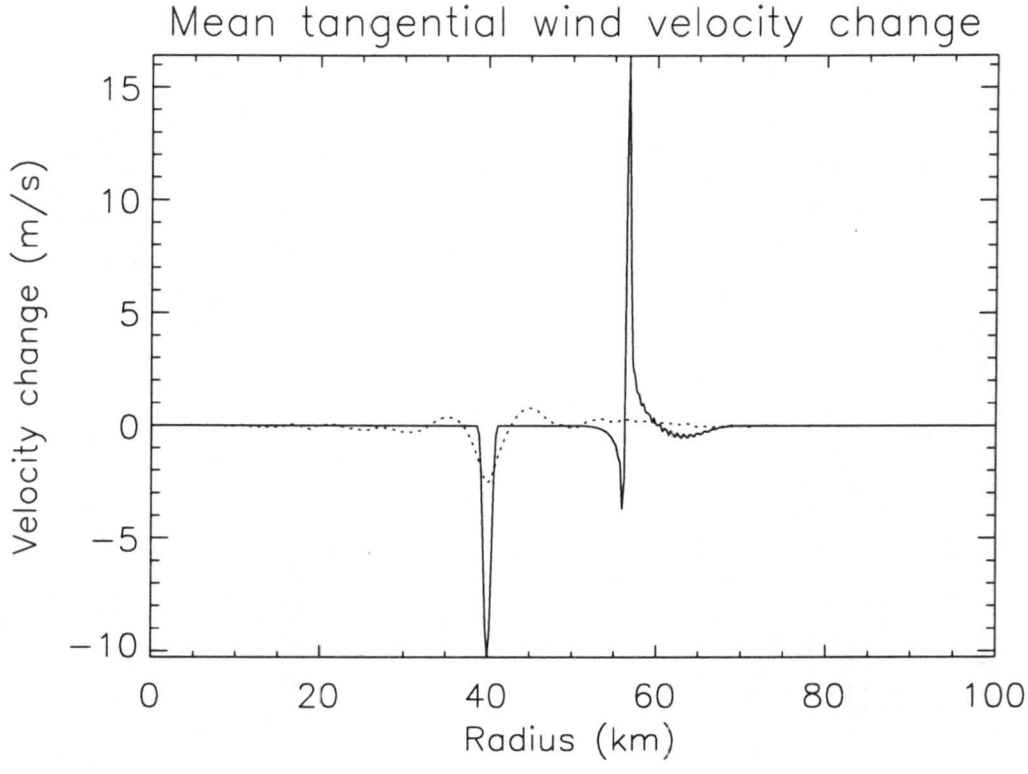

Figure 5.11: Same as Figure 5.10, but for the 60 km case.

As we move our perturbation closer to the critical radius, however, we begin to see strong signs of the breakdown of quasi-linear theory. Figure 5.11 shows that a significant spin-down at the interface still exists in the nonlinear run, but the magnitude is much less than its quasi-linear prediction and its profile has spread out radially. In contrast, the quasi-linear tripole near the critical radius in association with the linear resonance effect has been virtually eliminated in the nonlinear dynamics.

The reason for this change between the linear and nonlinear results becomes more apparent once we examine the time evolution of the mean velocity change. Figure 5.12 shows $\delta\bar{v}(t)$, integrated for the first 6 hours of the nonlinear integration along with the linear model's $\delta\bar{v}$ integrated over the full 60 hours.

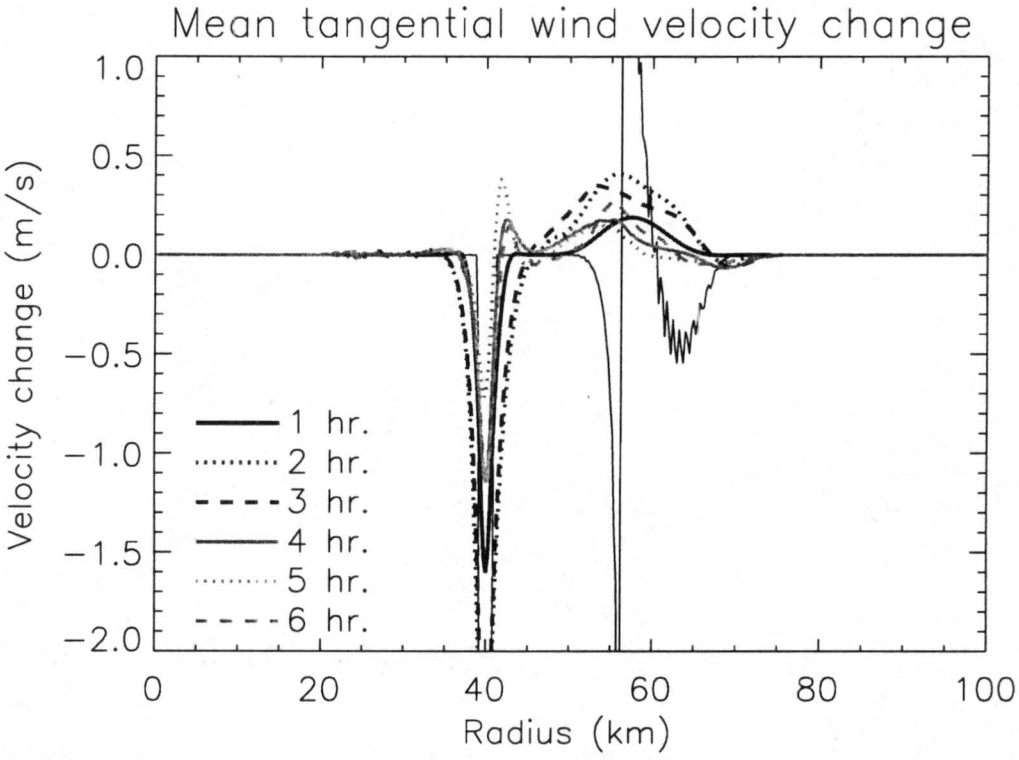

Figure 5.12: $\delta\bar{v}$ comparison between the linear (thin solid line) and nonlinear (other lines) model runs of the semispectral model in the 60 kilometer perturbation case. The linear integration is done over the full 60 hour life cycle, while the nonlinear model integrations are run for the indicated amounts of time.

Notice first that the $\delta\bar{v}$ calculation in the nonlinear model for the first three hours at the 40 km interface shows a strong deceleration. However, that initial deceleration becomes tempered as the discrete waves on the interface begin to weaken (see Figure 5.13). This initial response is forced by the linear dynamics, i.e. smooth perturbation's forcing on the discrete wave moving out of phase with the discrete wave. Shortly afterward, however, we believe that something essentially nonlinear is occurring.

5.5.2 Vorticity Mixing in the Wave-Induced Skirt

To better examine this phenomenon, we run the exact same calculation, except that we decrease the radial grid spacing to 125 meters (doubling the number of points everywhere and, in particular, in the Hermite spline to make it more smooth), double the number of resolved azimuthal modes to 20, and reduce the time step accordingly. Since we suspect that the critical radius is an important feature, we also seed some particles in the fluid at the initial time around the critical radius ($r_C = 56.57$ km), calculating their forward Lagrangian trajectories. We call this integration the "doubled resolution" simulation. This resolution allows us to rid ourselves almost entirely of Gibbs phenomena that is apparent near the interface in the original calculation (not shown).

Looking at the perturbation vorticity (ζ') in Figure 5.13, we note that the magnitude of perturbation vorticity on the interface is above 1×10^{-3} s^{-1} at 2 hours. Recalling that the magnitude of the Rankine vortex jump is 4×10^{-3} s^{-1}, it becomes obvious that this case is violating the linear approximation. Specifically, comparing the linear dynamical structure given in Figure 5.8 to the nonlinear structure in Figure 5.13, we begin to notice important differences. At $t = 1$ hour, the structure of the waves are similar enough to claim that nonlinearities are not significant. At $t = 2$ hours, the perturbations are still in similar places, but the magnitude of the inner interface's wave is already large compared to the Rankine vortex's vorticity. Much of the large magnitude of the discrete wave is attributable to the resonant interaction between the smooth perturbation and the discrete mode, as discussed in section 5.4.2.

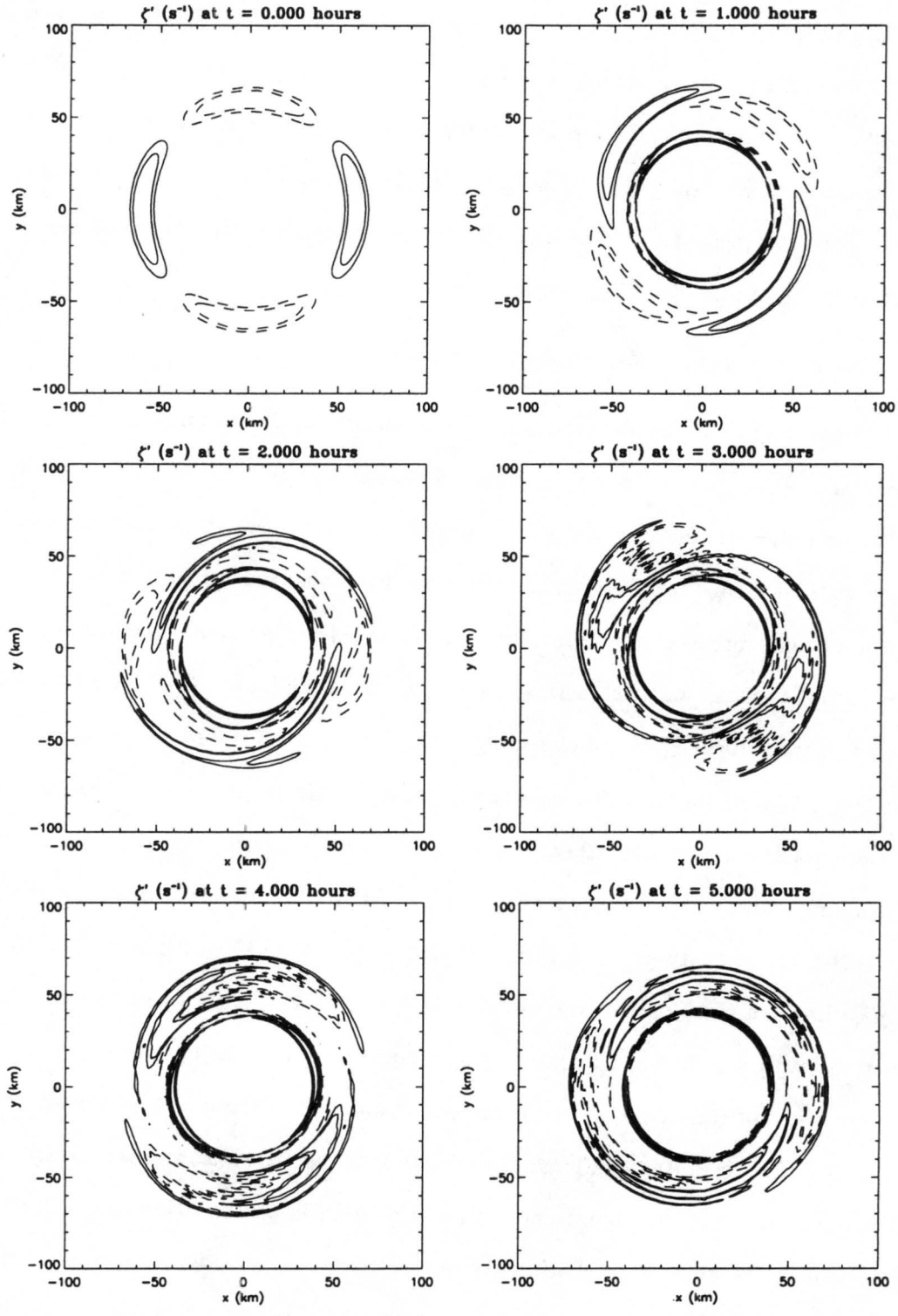

Figure 5.13: Perturbation (relative) vorticity plots (ζ') for the "doubled resolution" integration of the Rankine 60 km case for the first five simulation hours. The contours are $\pm 5.0 \times 10^{-5}$ s^{-1}, $\pm 1.0 \times 10^{-4}$ s^{-1}, $\pm 2.5 \times 10^{-4}$ s^{-1}, $\pm 5.0 \times 10^{-4}$ s^{-1}, $\pm 1.0 \times 10^{-3}$ s^{-1}. Negative contours are dashed.

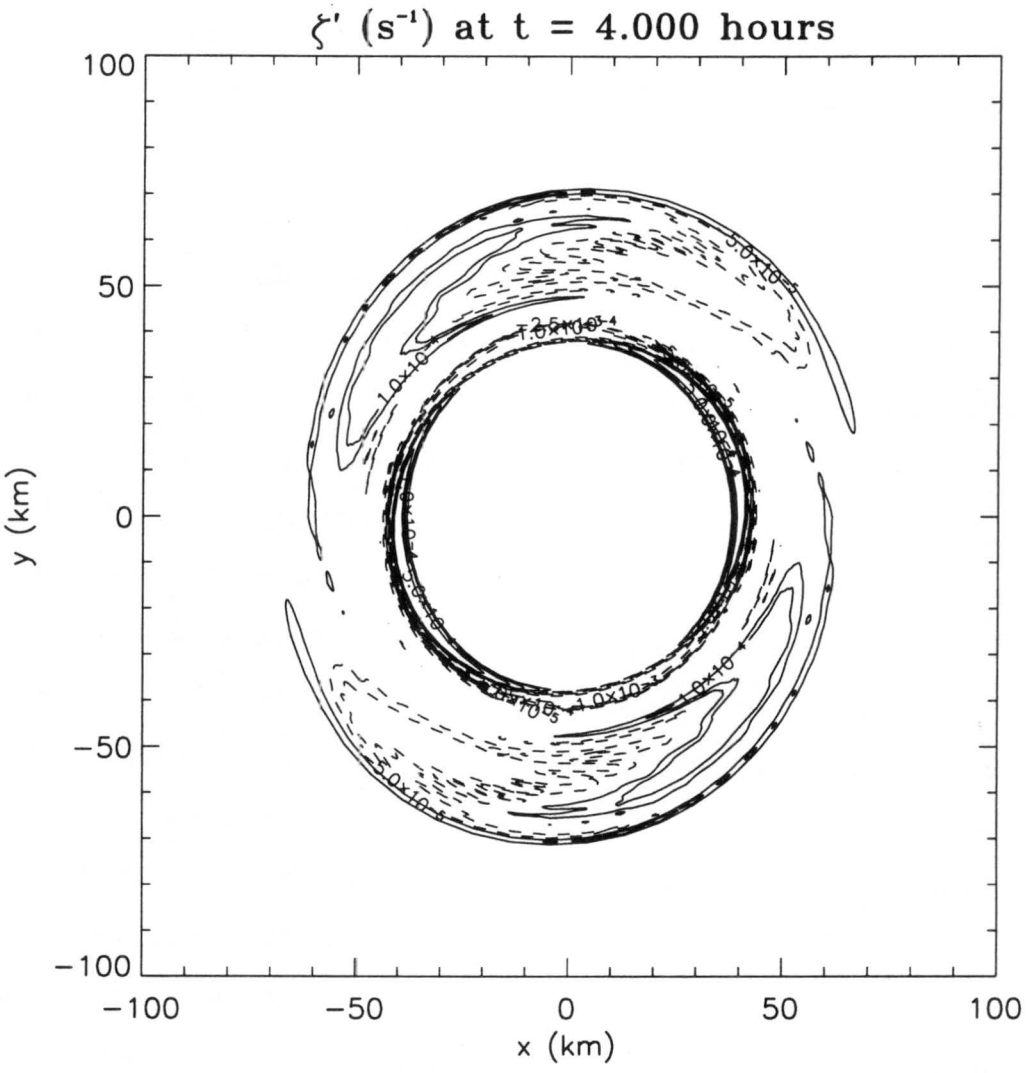

Figure 5.14: Perturbation (relative) vorticity plots (ζ') for the "doubled resolution" integration of the Rankine 60 km case at 4 hours. The contours are $\pm 5.0 \times 10^{-5}$ s^{-1}, $\pm 1.0 \times 10^{-4}$ s^{-1}, $\pm 2.5 \times 10^{-4}$ s^{-1}, $\pm 5.0 \times 10^{-4}$ s^{-1}, $\pm 1.0 \times 10^{-3}$ s^{-1}. Negative contours are dashed.

By the time the vortex has been allowed to evolve for four hours, however, the resulting structures appear to be nonlinear in nature. The main lobes of the initial asymmetries have moved closer to each other. As the main vortex strains the initial asymmetries and the radial wavenumber of these sheared disturbances increases, the distance between the asymmetries decreases, allowing for the waves to interact with each other in a significant manner. One can notice this most readily in Figure 5.13, where the positive vorticity perturbation gets strained by and strains the negative vorticity perturbation, particularly between 2 and 4 hours.

For a closer look at the evolution of those features, we focus on Figure 5.15. It is during this time period that the nonlinearities first appear to be the most pronounced. As the leading edge of the positive perturbation gets squeezed between the trailing edge of the negative perturbation and the negative lobe of the discrete wave, it is being progressively stretched and strained by both waves and by the mean flow. By $t = 2.6$ hours, the leading edge, though, is now being radially advected by both the negative perturbation lobe and the edge of the discrete perturbation. This causes the positive vorticity that is being stretched between the two negative perturbations to be "pooled" into a lobe with sizable radial extent.

By $t = 3.2$ hours, the main features are a pair of perturbation vorticity dipoles, the discrete wave whose rotation is being accelerated by these paired dipoles (since the perturbation winds associated with these across the interface is ahead of the crest of the discrete wave), and a pair of positive vorticity spiral bands which are the trailing edges of our original positive perturbation. But, it is the radially re-expansion of both the original positive and negative perturbations that draws our interest. This points to the potential of vorticity mixing playing an integral role in the evolution of the vortex.

As one way of establishing the importance of vorticity mixing, we examine the calculated azimuthal mean vorticity of the nonlinear calculation. Looking more closely at Figure 5.16, we notice one main interesting feature at $t = 3$ hours.

First, we see that outside the vortex interface, there appears to be a small mean vorticity concentration ($44 < r < 56$ km). This is similar to the "skirt" of vorticity discussed in the

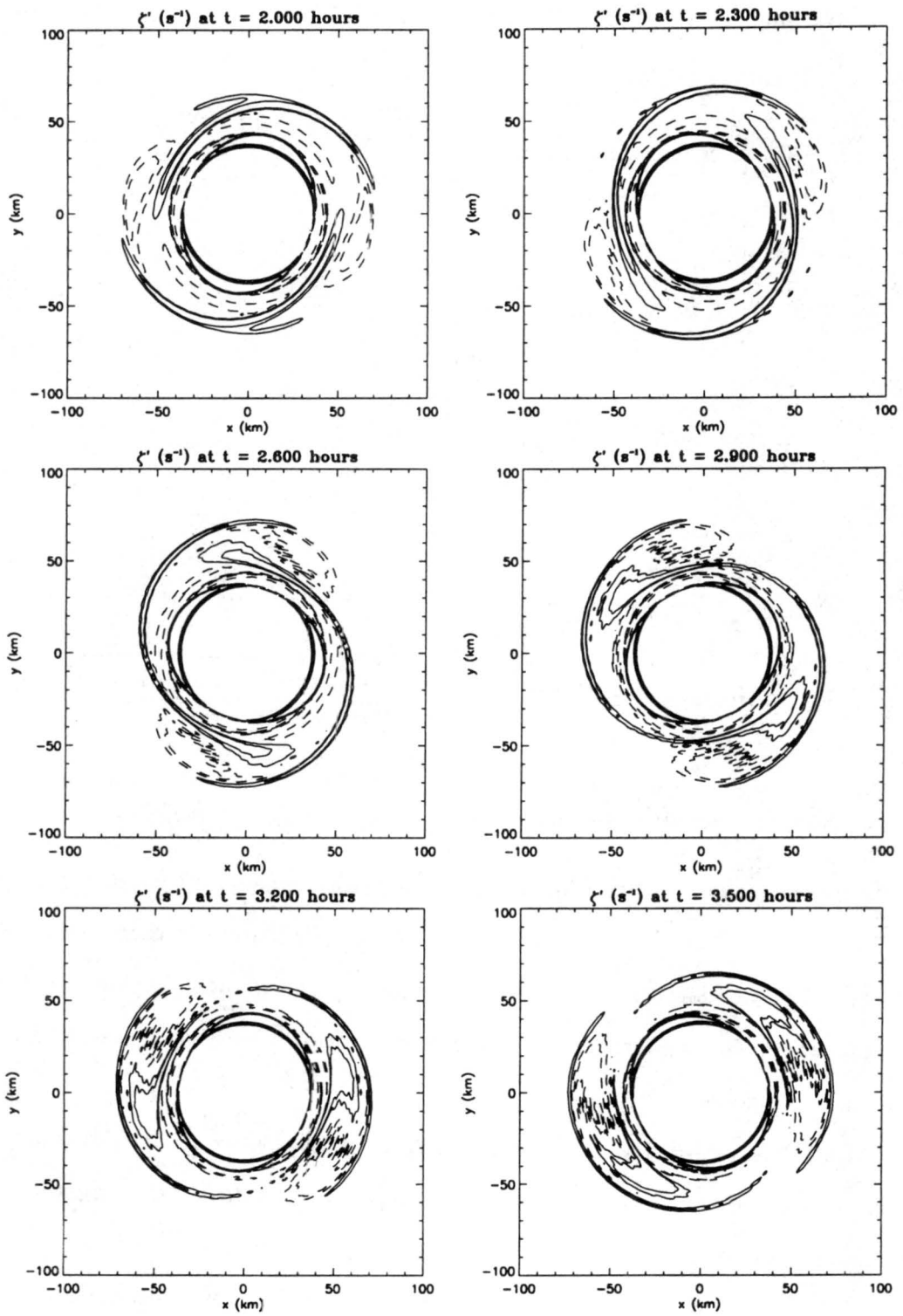

Figure 5.15: Same as 5.13, except in the time between 2 and 4 hours.

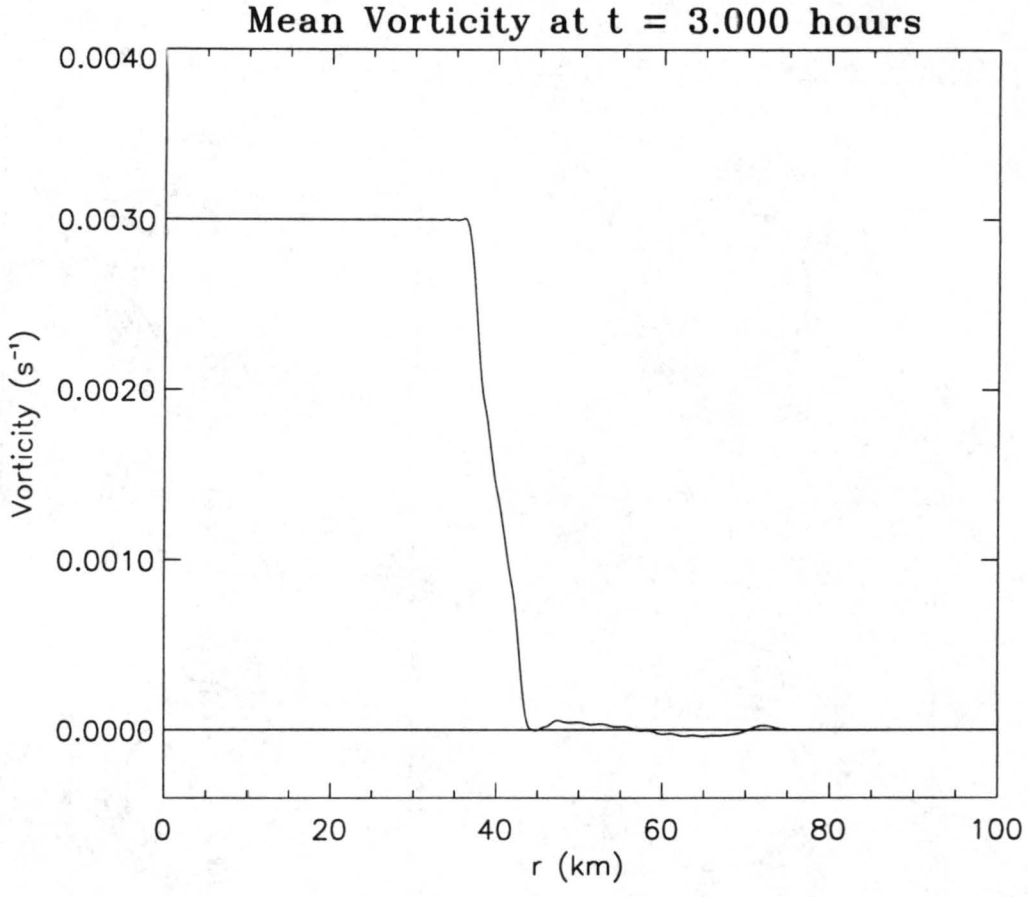

Figure 5.16: The mean vorticity ($\bar{\zeta}$) as calculated by the "doubled resolution" 60 km Rankine semispectral model run after three hours of integration.

three-dimensional vortex alignment and axisymmetrization paper of Schecter, Montgomery, and Reasor (2002), hereafter denoted by SMR02. It thus appears that strictly Rankine vortices, in conjunction with small amplitude sheared disturbances outside the core of the vortex, can, through wave-mean flow interaction, provide a pathway to resonant damping of the discrete modes.

In SMR02, an initial Rankine vortex with a "skirt" of positive vorticity outside the main vortex is shown to potentially damp out initial discrete waves in a three-dimensional quasi-geostrophic regime. In their problem, the discrete mode produces a cat's-eye streamline feature around the critical radius, once the rotation of the discrete mode is subtracted out. Because of this, the mean vorticity will tend to be redistributed and form a plateau in the vicinity of this radius. They then showed that, by angular momentum conservation,

the discrete mode will either decay (grow), given the local radial gradient of vorticity in the vicinity of the critical radius is negative (positive). When the gradient is negative, the discrete mode decays since the mean angular momentum around the critical radius increases as the mean vorticity is redistributed. The opposite is true if the gradient is positive, indicating an amplification of the discrete mode.

Figure 5.17 shows some evidence of this damping. The maximum vorticity perturbation at the interface grows initially, but as the skirt outside the main vortex grows, the perturbation begins to decay, most notably after $t = 4$ and $t = 7$ hours.

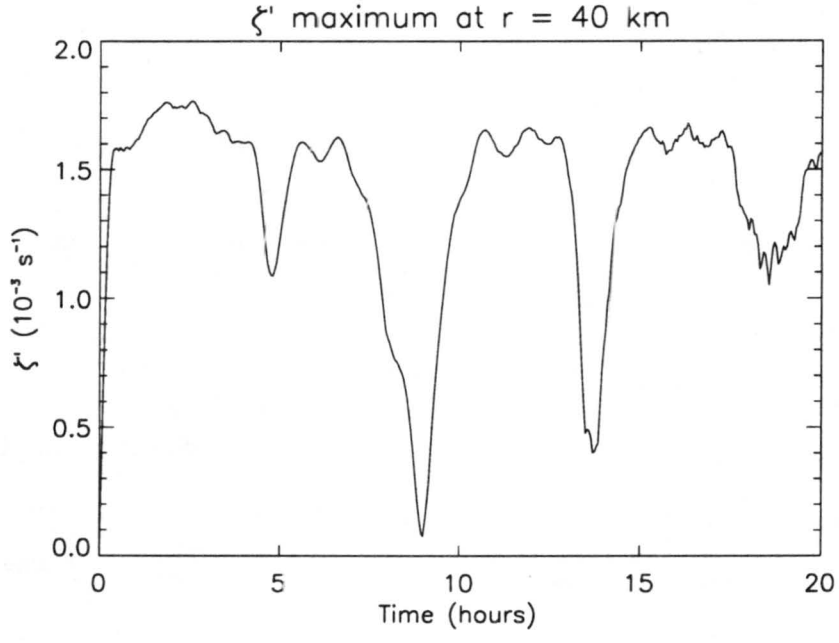

Figure 5.17: The maximum of the perturbation vorticity (ζ') at the interface ($r = 40$ km) in the "doubled resolution" Rankine nonlinear semispectral run.

The event from $t = 4$ to 5 hours appears to be due to the sheared disturbances moving out of phase with the discrete mode and forcing it adversely, as demonstrated previously on page 73. But, the dramatic decrease in the interface's perturbation vorticity starting after 7 hours appears to be consistent with the resonant damping hypothesis. Examining the mean vorticity radial derivative near r_c (Figure 5.18), we note that the first period of significant negative derivative occurs at about 7 hours. At about that time, the discrete mode in Figure 5.17 begins to decay. There is a weakening in the decay around 8 hours, which corresponds

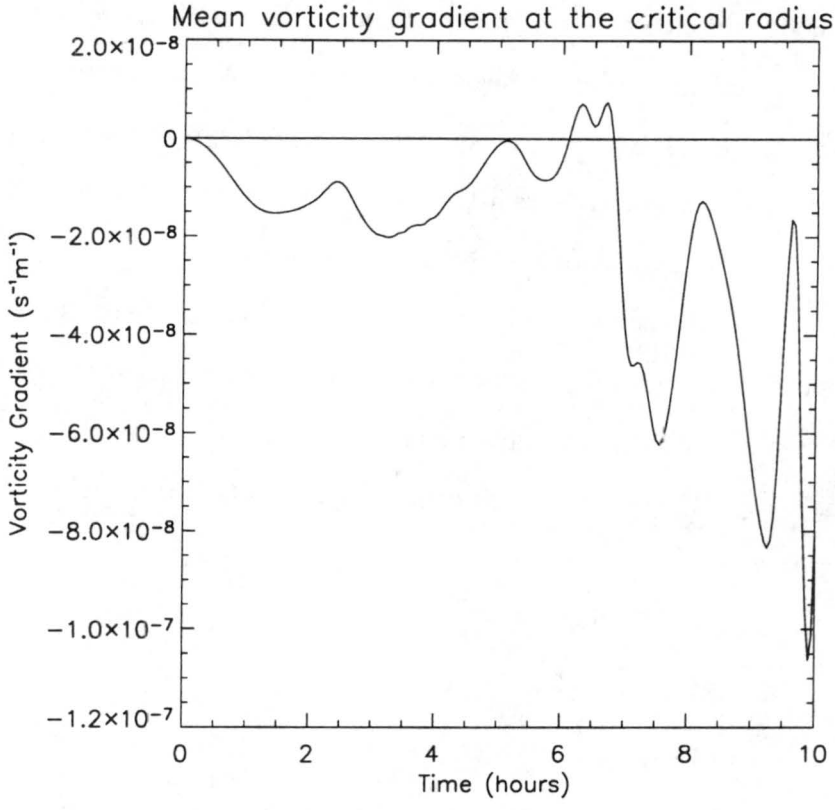

Figure 5.18: The radial derivative of vorticity at the critical radius, $r_c = 56.57$ km.

to a weakening of the negative gradient in mean vorticity, followed by another significant decay period correlated with another strong negative mean vorticity gradient.

To give further credence to our hypothesis that vorticity mixing may play an important role in the overall evolution in the 60 km case, we now examine the Lagrangian trajectories to see if the cat's-eye feature described in SMR02 exists.

Figure 5.19 shows the trajectories in this "doubled resolution" simulation in the frame of reference rotating with the discrete wave given by Kelvin's theory (see Equation (5.16)). The particles' trajectories are calculated as the model is run, using updated data every two model time steps (2 seconds in this case). The particles are seeded in (λ, r) space such that they lie in an approximately 2 km by 2 km grid, centered around $r_c = 56.57$ km on the x-axis. Red lines indicate particles that started inside the critical radius; green, on the critical radius; and blue, outside the critical radius. Lighter colors indicate those that started out azimuthally "ahead", while darker colors indicate those that started azimuthally "behind".

Particle positions at 4 hours are given by the colored asterisks, including a reference inset with the perturbation vorticity contoured. The critical radius is given by the dashed circle.

The interesting features here are the loops the particles all make with respect to the discrete wave. As the perturbation vorticity is stretched and strained in the flow, the particles separate, but all of them orbit around the critical radius. This supports the idea of the cat's-eye nature of the streamlines around the critical radius. Particles that start near it tend to be caught near it, allowing for mixing to occur.

On the basis of the foregoing discussion, we would expect that in fully linearized dynamics, the trajectories would be closer to complete circuits around the critical radius. To test this idea, we ran the "doubled resolution" model twice more, computing the trajectories of particles seeded in exactly the same place. The first extra run was a sort of "weakly nonlinear" run, where waves are not allowed to interact with one another, but the diagnosed mean flow change by the waves was added back into the mean flow. This run is called the "mean flow updating" run. In the other extra run, we reverted to the strictly linearized dynamics we explored earlier. The trajectory results for both of these runs can be seen in Figures 5.20 and 5.21

Comparing these three figures, we note that up to about 3 to 4 hours, the results are very similar between the linear, mean flow updating, and nonlinear trajectories. But after the initial few hours, the trajectories of the same particles diverge between the model runs. The cat's-eye phenomenon, however, seems to be robust, as one would expect it to be. In the linear calculation, the particles do not seem to separate too much, even at the end of 10 hours of integration, while in the mean flow updating run, there is a significant amount of separation of the particles by the end. It is interesting to note that the mean flow updating run tends to get the shorter loop of the outer particles (blue) but tends to overshoot the radial trajectories of the inner group (red) of particles.

It is thus apparent from the trajectories, that with sheared disturbances in the vicinity of critical radii that linearized dynamics may deviate significantly from the more realistic nonlinear dynamics after only a short time (on the order of 5 hours). This emphasizes the

importance of nonlinear dynamics in these cases, particularly when examining the changes in the mean flow by perturbations near the critical radius.

5.6 Discussion

Given the results above, linear theory gives us an accurate first guess to the initial dynamics, and in some cases, the long term dynamics. But, in some cases, particularly with strong initial perturbations or resonant interactions, nonlinear dynamics may end up dominating the evolution at moderate to long times, even in initially exponentially stable cases. For example, in the 80 km, and to a lesser extent, the 70 km cases, the linear model produced similar results to the nonlinear predictions. The 60 km Rankine case, however, showed a distinct disagreement due primarily to significant nonlinearities that were set up by a resonance between the pseudo-discrete wave on the interface and the main body of the sheared disturbance. This resonance led to a violation of the small perturbation assumption inherent in the linear dynamics.

The critical radius in (5.17) is the Rankine equivalent of what we called r_A and r_B from Chapter 4 for our three-region model. These radii, though not important in the strictly linear dynamics of the initial value problem, can prove to be imperative in the wave-mean flow dynamics for sheared perturbations in the vicinity of the critical radii. These radii should affect these quasi-linear dynamical features in the three-region model (and n-region models) in much the same way as it affected the Rankine vortex.

Lastly, we observed that these critical radii may provide a mechanism for the resonant damping of the discrete modes, as demonstrated in SMR02 for an initial Rankine vortex with an outer "skirt" of vorticity. This is interesting because such a skirt was not prescribed in our initial basic-state vortex. But, as the vortex axisymmetrized, the sheared disturbances that we had initially prescribed produced a mean vorticity skirt. The interactions between this newly-formed skirt and the Rankine vortex and its discrete modes then appear to be similar to the situation described in SMR02. The effects of sheared disturbances on sharp gradient vortices are seen to produce a much richer dynamical problem than was initially envisioned.

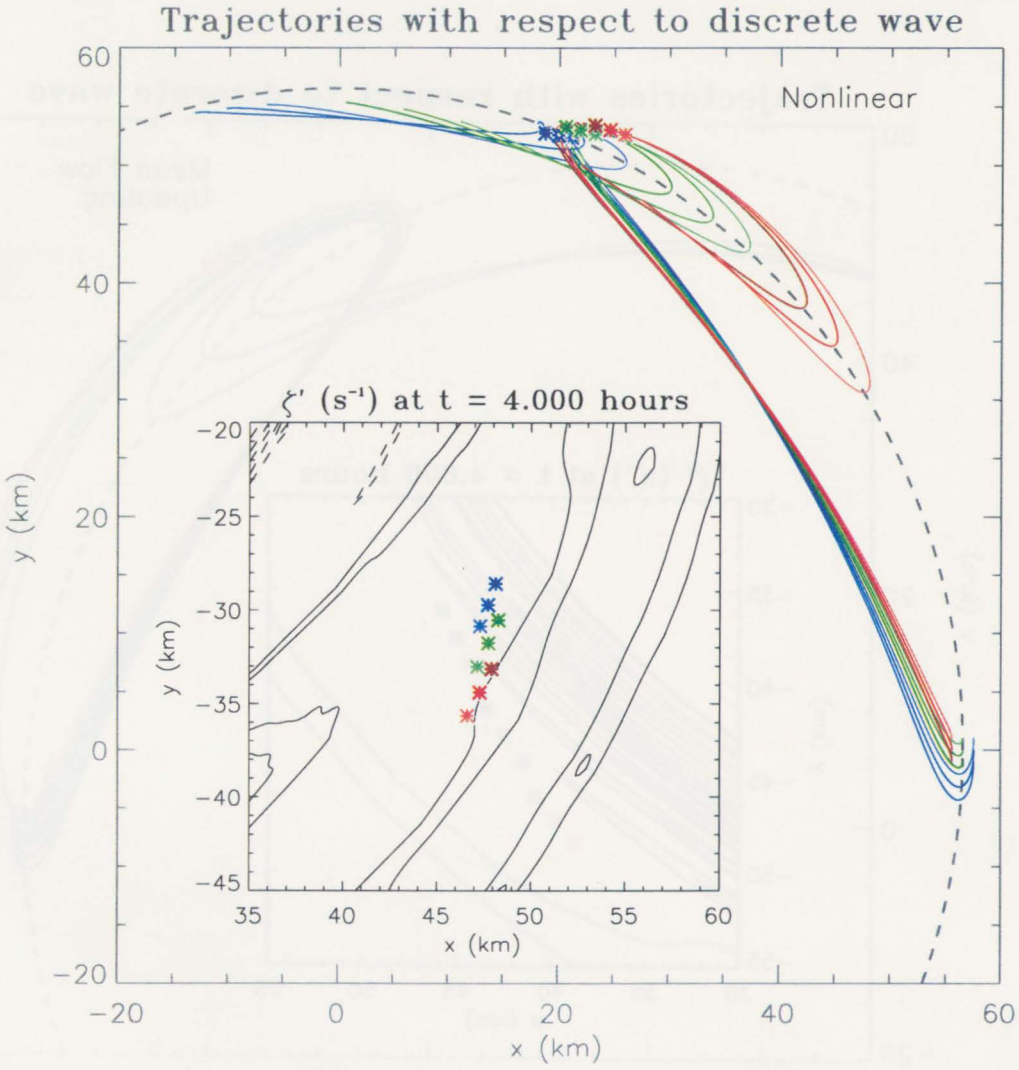

Figure 5.19: Trajectories in the frame of reference rotating with the Kelvin solution for the discrete vortex Rossby wave (see Equation (5.16)) for the "doubled resolution" nonlinear run. The trajectories are run forward for the first 10 hours of the model simulation. The inset shows the physical position of the particles after 4 hours. The particles are initially seeded in an approximately 2 km by 2 km box centered on r_C and near the center of the initial positive perturbation vorticity. See Figure 5.22 for inset reference positions.

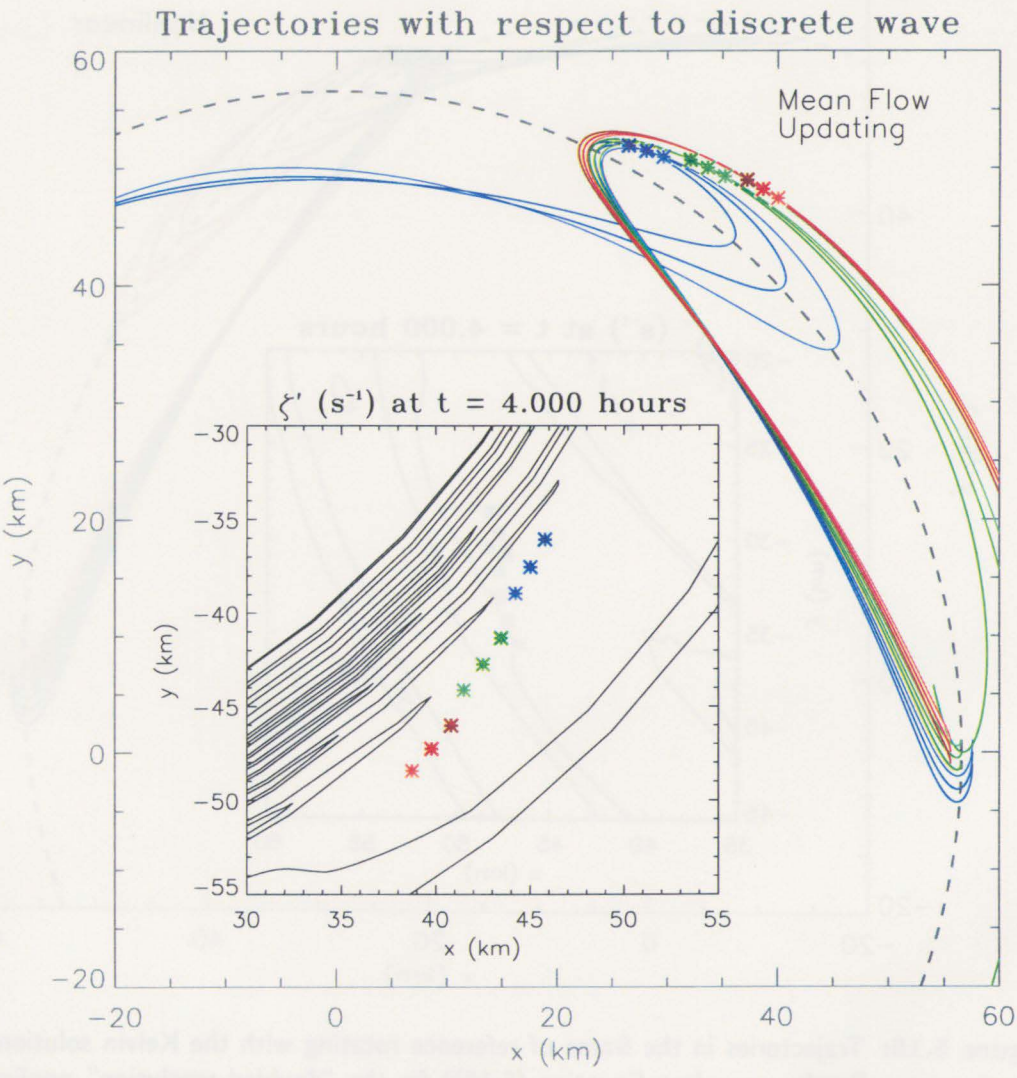

Figure 5.20: Same as Figure 5.19, except for the "doubled resolution" run where wave-wave effects are turned off, but the mean flow is still updated.

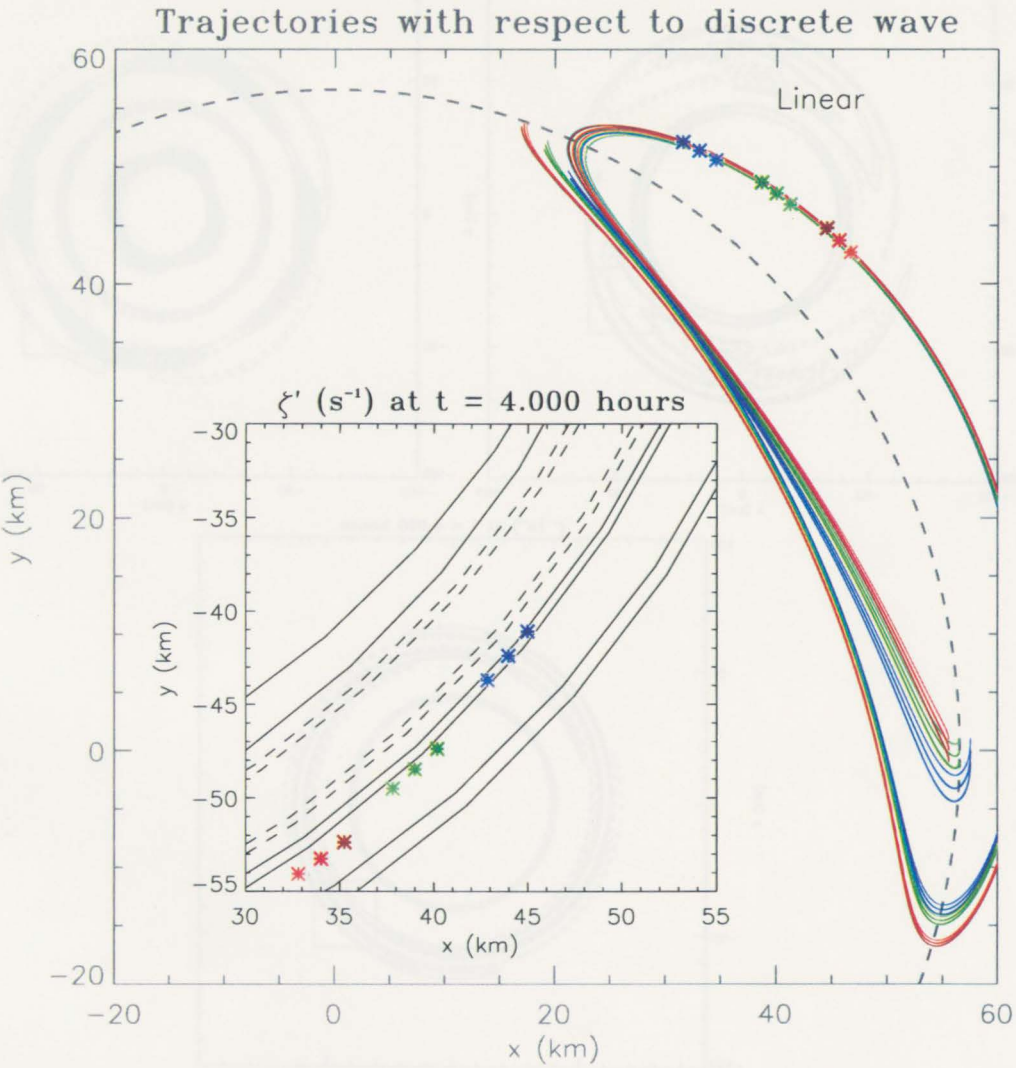

Figure 5.21: Same as Figure 5.19, except for the "doubled resolution" run with totally linearized dynamics.

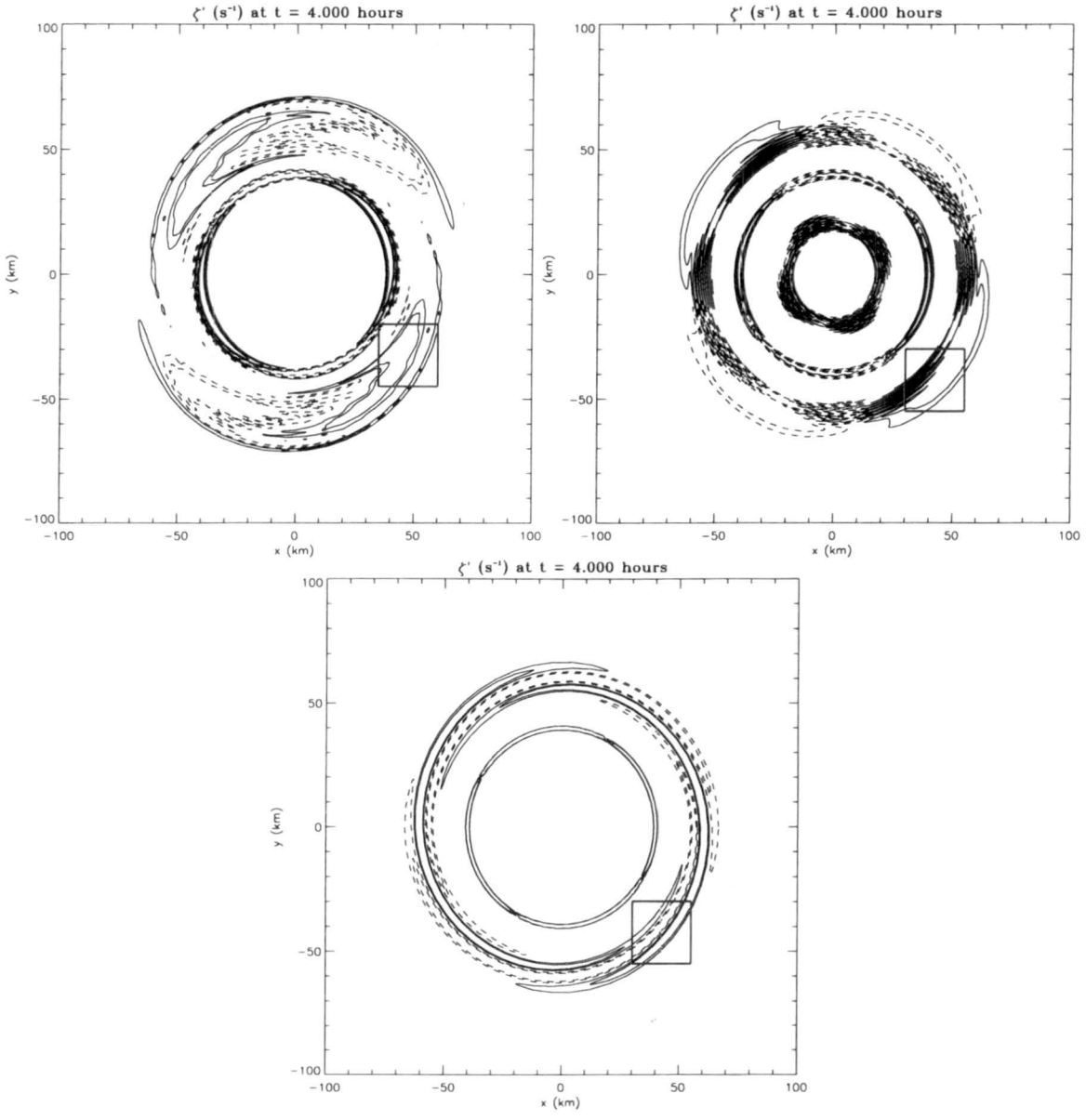

Figure 5.22: Perturbation vorticity in the "doubled resolution" runs after 4 hours in the nonlinear (top left), mean-flow updating (top right), and linear (bottom center). The boxes correspond to the insets in Figures 5.19, 5.20 and 5.21, respectively.

Chapter 6

DISCUSSION AND CONCLUSIONS

By setting up and solving the two-dimensional linear initial value problem for general perturbations on a mean circular vortex with two steep gradients, we find some interesting and enlightening results that can lead to better understanding of real geophysical vortices.

First, we demonstrated that the classic exponential shear instability can exist for wavenumber-2 in the three-region model, as hinted by VT80 and F88. The existence of this particular instability, shown in other works to be relatively prevalent in some geophysical vortices, in this problem allays concerns regarding the usefulness of this particular theoretical framework.

After finding the complete perturbation solutions to this problem, we notice that, outside of the classic exponential instabilities, there are no other non-trivial instabilities in the model. An algebraic instability does exist, but it is a trivial case that represents the coalescence of roots solution, i.e. the transition between exponential instability and stability. Furthermore, we demonstrate that the exponential instability properties of the vortex are unchanged by the inclusion of vorticity perturbations (sheared disturbances) outside the jump radii, implying that small asymmetric perturbations around steep gradient vortices do not change the vortex to make it less or more susceptible to exponential instability processes. They may provide the initial forcing to the main vortex, but will not change the exponential stability properties of it.

Given recent works (SR90, NM00, NMG01) describing an trochoidal instability for wavenumber-1, the lack of any non-trivial trochoidal instability in the complete solution raises a warning flag. We find that the lack of this instability is due to the intimate

differences between the basic state used in those works and the one we utilize, i.e. our mean vortex has cusps and other discontinuities while those works assumed smooth mean vortex profiles. The trochoidal instability found in those recent works requires a smooth local maximum of angular velocity ($\bar{\Omega}$), which our mean vortex cannot possess. This fundamental difference between our "discrete" vortex and the "smooth" vortex in those studies eliminates this mode of instability, even in vortices with more than three discrete regions.

Even though there are few surprises in the linear perturbation solution itself, once we begin to use the linear solution to diagnose the potential eddy momentum fluxes and mean tangential velocity changes, we then note that the interactions between the discrete modes and sheared disturbances may be more important than the perturbation solution might indicate. The mean flow accelerations diagnosed using the linear solutions for the discrete modes and sheared disturbances combined can be amplified significantly over the accelerations produced by just the linear axisymmetrization of the sheared disturbances. This modification of momentum and vorticity fluxes by the combination of these two perturbations is potentially important in the mean flow changes of geophysical vortices. This effect may be particularly effective for the prediction of velocity changes on short timescales where linear theory is most applicable.

The emphasis on short times becomes more apparent when sheared disturbances are placed near critical radii in the mean vortex. Perturbations near these critical radii are resonant with the discrete modes they excite, producing potentially large amplitude discrete modes after a short period of time. The production of these high amplitude discrete modes nullifies the "small amplitude" assumption associated with linear theory, pointing to the importance of nonlinear mixing near these critical radii in the evolution of such vortices. Upon further examination of these resonant cases using a fully nonlinear model, we find that the mean flow accelerations of perturbations near a critical radius in nonlinear theory tends to produce a "skirt" of mean vorticity around that radius. This skirt then plays its role in the resonant damping of the discrete vortex Rossby waves. This is very interesting, since resonant damping is not a process that is encapsulated in our original linear initial value

problem. Therefore, with the inclusion of nonlinear processes, especially in these resonant cases, this simple vortex problem opens itself to a much richer class of phenomena than is contained in the original linear initial value problem.

Appendix A

SIMPLIFICATION OF INHOMOGENEOUS TERM

We start with

$$\left[\left(\frac{d}{dt}+i\nu_2\right)i\alpha_1+\mu_1\alpha_2\right].$$

Recalling the definitions of these terms (2.25), we get that this term equals

$$\begin{aligned}\left[\left(\frac{d}{dt}+i\nu_2\right)i\alpha_1+\mu_1\alpha_2\right] &= \frac{\partial}{\partial t}\left[-\frac{in\xi_1}{r_1}\int_0^\infty G(r_1,\rho)\hat{\zeta}_{s0}(\rho)\rho e^{-int\bar{\Omega}(\rho)}d\rho\right] \\ &+\left(in\bar{\Omega}(r_2)-\frac{i\xi_2}{2}\right)\left[-\frac{in\xi_1}{r_1}\int_0^\infty G(r_1,\rho)\hat{\zeta}_{s0}(\rho)\rho e^{-int\bar{\Omega}(\rho)}d\rho\right] \\ &-\left(-\frac{i\xi_1\delta^{n-1}}{2}\right)\left[\frac{in\xi_2}{r_2}\int_0^\infty G(r_2,\rho)\hat{\zeta}_{s0}(\rho)\rho e^{-int\bar{\Omega}(\rho)}d\rho\right]. \quad \text{(A.1)}\end{aligned}$$

The right hand side is equivalent to

$$\begin{aligned}&\int_0^\infty\left[-\frac{n^2\xi_1\bar{\Omega}(\rho)}{r_1}G(r_1,\rho)\right]\hat{\zeta}_{s0}(\rho)\rho e^{-int\bar{\Omega}(\rho)}d\rho \\ &+\int_0^\infty\left[\left(\frac{n^2\xi_1\bar{\Omega}(r_2)}{r_1}-\frac{n\xi_1\xi_2}{2r_1}\right)G(r_1,\rho)\right]\hat{\zeta}_{s0}(\rho)\rho e^{-int\bar{\Omega}(\rho)}d\rho \\ &+\int_0^\infty\left[-\frac{n\xi_1\xi_2}{2r_2}G(r_2,\rho)\right]\hat{\zeta}_{s0}(\rho)\rho e^{-int\bar{\Omega}(\rho)}d\rho. \quad \text{(A.2)}\end{aligned}$$

Combining these three integrals, we get the assumed form of this term:

$$\int_0^\infty \mathcal{G}(\rho)\hat{\zeta}_{s0}(\rho)\rho e^{-int\bar{\Omega}(\rho)}d\rho \quad \text{(A.3)}$$

where the composite Green function $\mathcal{G}(\rho)$ is defined as

$$\begin{aligned}\mathcal{G}(\rho) &= \left[-\frac{n^2\xi_1\bar{\Omega}(\rho)}{r_1}+\frac{n^2\xi_1\bar{\Omega}(r_2)}{r_1}-\frac{n\xi_1\xi_2}{2r_1}\right]G(r_1,\rho)+\left[-\frac{n\xi_1\xi_2}{2r_2}\delta^{n-1}\right]G(r_2,\rho) \\ &= \left[\frac{n^2\xi_1}{r_1}\left(\bar{\Omega}(r_2)-\bar{\Omega}(\rho)\right)-\frac{n\xi_1\xi_2}{2r_1}\right]G(r_1,\rho)+\left[-\frac{n\xi_1\xi_2}{2r_2}\delta^{n-1}\right]G(r_2,\rho) \quad \text{(A.4)}\end{aligned}$$

REFERENCES

Balmforth, N. J., S. G. Llewellyn, and W. R. Young, 2001: Disturbing vortices. *J. Fluid Mech.*, **426**, 95-133.

Black, P. G., and F. D. Marks, 1991: The structure of an eyewall meso-vortex in Hurricane Hugo (1989). Preprints, *19th Conf. on Hurricanes and Tropical Meteorology*, Miami, FL, Amer. Meteor. Soc., 579-582.

Booker, J. R., and F. P. Bretherton, 1967: The critical layer for internal gravity waves in a shear flow. *J. Fluid Mech.*, **27**, 513-539.

Briggs, R. J., J. D. Daugherty, and R. H. Levy, 1970: Role of Landau damping in crossed-field electron beams and inviscid shear flow. *Phys. Fluids*, **13**, 421-432.

Brown, S. N., and K. Stewartson, 1980: On the algebraic decay of disturbances in a stratified linear shear flow. *J. Fluid Mech.*, **100**, 811-816.

Brunet, G., and M. T. Montgomery, 2002: Vortex Rossby waves on smooth circular vortices. Part I: Theory. *Dyn. of Atmos. and Oceans*, **35**, 153-177.

Brunet, G., and T. Warn, 1990: Rossby wave critical layers on a jet. *J. Atmos. Sci.*, **47**, 1173-1178.

Carr, L. E. III, and R. T. Williams, 1989: Barotropic vortex stability to perturbations from axisymmetry. *J. Atmos. Sci.*, **46**, 3177-3191.

Chen, Y., and M. K. Yau, 2001: Spiral bands in a simulated hurricane. Part I: Vortex Rossby wave verification. *J. Atmos. Sci.*, **58**, 2128-2145.

Davis, C. A., and L. F. Bosart, 2001: Numerical simulations of the genesis of Hurricane Diana (1984). Part I: Control simulation. *Mon. Wea. Rev.*, **129**, 1859-1881.

Dritschel, D. G., 1989: On the stabilization of a two-dimensional vortex strip by adverse shear. *J. Fluid Mech.*, **206**, 193-221.

Dritschel, D. G., 1998: On the persistence of non-axisymmetric vortices in inviscid two-dimensional flows. *J. Fluid Mech.*, **371**, 141-155.

Farrell, B. F., 1984: Modal and non-modal baroclinic waves. *J. Atmos. Sci.*, **41**, 668-673.

Farrell, B. F., 1987: Developing disturbances in shear. *J. Atmos. Sci.*, **44**, 2191-2199.

Flierl, G. R., 1988: On the instability of geostrophic vortices. *J. Fluid Mech.*, **197**, 349-388.

Gent, P. R., and J. C. McWilliams, 1985: The instability of barotropic circular vortices. *Geophys. Astrophys. Fluid Dynamics*, **35**, 209-233.

Hoskins, B. J., M. E. McIntyre, and A. W. Robertson, 1985: On the use and significance of isentropic potential vorticity maps. *Quart. J. R. Met. Soc.*, **111**, 877-946.

Juckes, M. N., and M. E. McIntyre, 1987: A high-resolution one-layer model of breaking planetary waves in the stratosphere. *Nature*, **328**, 590-596.

Kossin, J. P., and W. H. Schubert, 2001: Mesovortices, polygonal flow patterns, and rapid pressure falls in hurricane-like vortices. *J. Atmos. Sci.*, **58**, 2196-2209.

Kossin, J. P., W. H. Schubert, and M. T. Montgomery, 2000: Unstable interactions between a hurricane's primary eyewall and a secondary ring of elevated vorticity. *J. Atmos. Sci.*, **57**, 3893-3917.

Labitzke, K., and Collaborators, 2002: The Berlin Stratospheric Data Series, CD from Meteorological Institute, Free University Berlin.

Lamb, H., 1932: *Hydrodynamics.* 6th ed., Dover, 732 pp.

Lee, W.-C., B. J.-D. Jou, P.-L. Chang, and S.-M. Deng, 1999: Tropical cyclone kinematic structure retrieved from single-Doppler radar observations. Part I: Interpretation of Doppler velocity patterns and the GBVTD technique. *Mon. Wea. Rev.*, **127**, 2419-2439.

Lindzen, R. A, 1990: *Dynamics of Atmospheric Physics*, Cambridge Univ. Press, London, 310 pg.

Lugovtsov, B. A., 1982: Laboratory Models of Tornado-like Vortices. *Topics in Atmospheric and Oceanographic Sciences: Intense Atmospheric Vortices*, ed. Bengtsson/Lighthill, Springer-Verlag, Berlin, 299-312.

McIntyre, M. E., 1993: Isentropic distributions of potential vorticity and their relevance to tropical cyclone dynamics. *ICSU/WMO International Symposium on Tropical Cyclone Disasters*, University Press, 143-156.

Michalke, A., and A. Timme, 1967: On the inviscid instability of certain two-dimensional vortex-type flows. *J. Fluid Mech.*, **29**, 647-666.

Montgomery, M. T., and G. Brunet, 2002: Vortex Rossby waves on smooth circular vortices. Part II: Idealized numerical experiments for tropical cyclone and polar vortex interiors. *Dyn. of Atmos. and Oceans*, **35**, 179-204.

Montgomery, M. T., and J. Enagonio, 1998: Tropical cyclogenesis via convectively forced vortex Rossby waves in a three-dimensional quasi-geostrophic model. *J. Atmos. Sci.*, **55**, 3176-3207.

Montgomery, M. T., J. M. Hidalgo, and P. D. Reasor, 2000: A semi-spectral numerical method of modeling the vorticity dynamics of the near-core region of hurricane-like vortices. Atmospheric Science Paper No. 695, Colorado State University, 56 pp. [Available from Dept. of Atmospheric Science, Colorado State University, Fort Collins, CO, 80523.]

Montgomery, M. T., and R. J. Kallenbach, 1997: A theory for vortex Rossby-waves and its application to spiral bands and intensity changes in hurricanes. *Q. J. R. Meteorol. Soc.*, **123**, 435-465.

Montgomery, M. T., V. A. Vladimirov, and P. V. Denissenko, 2002: An experimental study on hurricane mesovortices. *J. Fluid Mech.*, **471**, 1-32.

Nolan, D. S., and B. F. Farrell, 1999: The intensification of two-dimensional swirling flows by stochastic asymmetric forcing. *J. Atmos. Sci.* **56**, 3937-3962.

Nolan, D. S., and M. T. Montgomery, 2000: The algebraic growth of wavenumber one disturbances in hurricane-like vortices. *J. Atmos. Sci.*, **57**, 3514-3538.

Nolan, D. S., M. T. Montgomery, and L. D. Grasso, 2001: The wavenumber one instability and trochoidal motion of hurricane-like vortices. *J. Atmos. Sci.*, **58**, 3243-3270.

Orr, W. M., 1907: The stability or instability of the steady motions of a perfect liquid. *Proc. Roy. Irish Acad.*, **27**, 9-69.

Polvani, L. M., and R. A. Plumb, 1992: Rossby wave breaking, microbreaking, filamentation, and secondary vortex formation: The dynamics of a perturbed vortex. *J. Atmos. Sci.*, **49**, 462-476.

Reznik, G. M., and W. K. Dewar, 1994: An analytical theory of distributed axisymmetric barotropic vortices on the beta-plane. *J. Fluid Mech.*, **269**, 301-321.

Schecter, D. A., A. C. Cass, C. F. Driscoll, I. M. Lansky, and T. M. O'Neil, 2000: Inviscid damping of asymmetries on a two-dimensional vortex. *Phys. Fluids*, **12**, 2397-2412.

Schecter, D. A., M. T. Montgomery, and P. D. Reasor, 2002: A theory for the vertical alignment of a quasigeostrophic vortex. *J. Atmos. Sci.*, **59**, 150-168.

Schubert, W. H., M. T. Montgomery, R. K. Taft, T. A. Guinn, S. R. Fulton, J. P. Kossin, and J. P. Edwards, 1999: Polygonal eyewalls, asymmetric eye contraction, and potential vorticity mixing in hurricanes. *J. Atmos. Sci.*, **56**, 1197-1223.

Smith, G. B., and M. T. Montgomery, 1995: Vortex axisymmetrization: Dependence on azimuthal wave-number on asymmetric radial structure changes. *Q. J. R. Meteorol. Soc.* **121**, 1615-1650.

Smith, R. A., and M. N. Rosenbluth, 1990: Algebraic instability of hollow electron columns and cylindrical vortices. *Physical Review Letters,* **64**, 649-652.

Staley, D. O., and R. L. Gall, 1979: Barotropic instability in a tornado vortex. *J. Atmos. Sci.,* **36**, 973-981.

Vladimirov, V. A., and V. F. Tarasov, 1980: Formation of a system of vortex filaments in a rotating liquid. *Izv. Akad. Nauk SSSR, Mekhanika Zhidkosti i Gaza*, **1**, 44-51.

Wurman, J., 2002: The multiple-vortex structure of a tornado. *Weather and Forecasting*, **17**, 473-505.

Zwillinger, D., 1998: *Handbook of Differential Equations*, 3rd ed., Academic Press, 801 pp.